CHEMICAL REVIEWS

Review

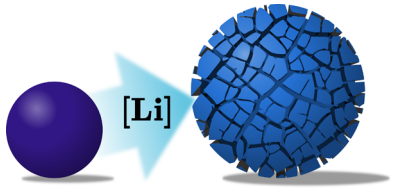
pubs.acs.org/CR

Alloy Negative Electrodes for Li-Ion Batteries

M. N. Obrovac*[,†] and V. L. Chevrier[‡]

[†]Department of Chemistry, Dalhousie University, Halifax, Nova Scotia B3H 4R2, Canada

[‡]Corporate Research Materials Laboratory, 3M Center, St. Paul, Minnesota 55144-1000, United States



CONTENTS

1. Introduction 11444
2. Key Parameters of Alloy Anode Performance 11446
  2.1. A Cell-Based Model for Comparing Anode Performance 11446
  2.2. Full Cell Volumetric Energy Comparison of the Active Elements 11449
  2.3. Electrode Porosity, Irreversible Capacity, and Coulombic Efficiency 11450
3. Fundamentals of Li Insertion in Metals and Alloys 11450
  3.1. The Active Elements 11450
    3.1.1. Hydrogen and the Alkali Metals 11451
    3.1.2. The Alkaline Earth Metals 11451
    3.1.3. The Transition Metals 11452
    3.1.4. The p-Block Elements 11453
  3.2. Selective Formation of Li−M Equilibrium Phases 11457
  3.3. Volume Expansion during Lithiation 11457
  3.4. Effect of Two-Phase Regions on Cycle Life 11458
  3.5. Ability of DFT To Predict Alloy Voltages 11458
  3.6. The Electrochemistry of Silicon 11460
    3.6.1. The Electrochemistry of Bulk Silicon 11460
    3.6.2. The Electrochemistry of Nanosized Silicon 11463
    3.6.3. The Electrochemistry of Thin Film Silicon 11463
  3.7. Alloys of the Active Elements 11464
    3.7.1. Active/Active Alloys 11465
    3.7.2. Active/Inactive Alloys 11472
4. Binders, Surface Coatings, and Electrolytes 11477
  4.1. Binders 11477
  4.2. Surface Coatings 11479
  4.3. Electrolytes and Additives 11480
    4.3.1. Electrolytes for Silicon Alloys 11480
    4.3.2. Electrolytes for Tin Alloys 11481
5. Evaluation of Alloy Cycling Performance in Cells and Coatings 11481
  5.1. Half-Cells 11482
    5.1.1. Half-Cell Cycling Using Constant Voltage Limits 11482
    5.1.2. Half-Cell Cycling Using Constant Capacity Limits 11482
    5.1.3. Differential Capacity Analysis 11483
  5.2. Symmetric Cells 11483
  5.3. Full Cells 11483
  5.4. Impedance Analysis 11484
  5.5. Acoustic Emission Analysis 11485
  5.6. Dilatometry 11485
  5.7. Isothermal Calorimetry 11486
6. Thermal Stability of Alloy Negative Electrodes 11486
  6.1. Reactivity of Alloy Anodes As Compared To Graphite 11487
  6.2. Impact of Solvent and Salt on Alloy Thermal Stability 11487
  6.3. Impact of Surface Area on Alloy Thermal Stability 11487
7. Implementation in Commercial Cells 11488
  7.1. Irreversible Capacity Management 11488
  7.2. Coating Design for Commercial Cells 11488
  7.3. Some Industrially Developed Alloy Materials 11489
    7.3.1. Sn−Co−C Alloys 11489
    7.3.2. SiO-Based Electrodes 11491
    7.3.3. Si−Metal Alloys 11493
8. Concluding Remarks 11493
Author Information 11494
  Corresponding Author 11494
  Notes 11494
  Biographies 11494
Acknowledgments 11494
References 11494

1. INTRODUCTION

Graphite is an excellent negative electrode (anode) material for Li-ion batteries. It has high specific capacity (e.g., ~2.5× higher than $LiCoO_2$), high volumetric capacity (~the same as $LiCoO_2$), low average voltage (but not too low, so that Li plating can be avoided), low voltage hysteresis, good rate capability, low irreversible capacity, good thermal stability when low surface area is maintained, low volume expansion during lithiation, good cycle life, high Coulombic efficiency (CE), good electronic conductivity, excellent densification properties in electrode coatings, and is based on an inexpensive and plentiful raw material. The combination of all of these properties in one material is quite miraculous, in fact. Improving on this miracle material is the task of researchers involved in the development of alloy anode materials. It should not be underestimated what a difficult task this presents.

In writing this Review, we have noticed that this task has been made much more difficult, because most alloy anode research has

Special Issue: 2014 Batteries

Received: April 14, 2014
Published: November 17, 2014

 © 2014 American Chemical Society dx.doi.org/10.1021/cr500207g | Chem. Rev. 2014, 114, 11444−11502

Zhuhai CosMX Battery Co. EX1015
Zhuhai CosMX Battery Co. v. Ningde Amperex Tech. Ltd.

Table 1. Estimations of the Volumetric Capacity, Volume Expansion, Average Voltage, and Stack Energy (According to the Full Cell Model Described in Section 2) for Alloys Discussed in the Text[a]

alloy	ref	capacity (Ah/L)	expansion (%)	average voltage (V)	stack energy (Wh/L)	improvement (%)
graphite		719	10	0.125	726	0
Mg_2Si	3	1248	73	0.26	838	15
$Si_{66}Sn_{34}$	4	2160	264	0.5	946	30
$Si_{75}Al_{25}$	5	1964	194	0.4	900	24
Sn−C	6	2876	0	1.5	661	−9
Sn−C	7	1489	0	1.5	580	−20
$LaSn_3$	8	1114	0	0.6	747	1
SnO		1670	238	0.5	843	16
TCO-1	9	1230	70	0.5	778	7
$Sn_{30}Co_{30}C_{40}$	10	1260	150	0.45	796	10
SiO		1547	117	0.4	853	17
Si−C	11	1814	0	0.47	869	20
3M L-20772	12	1550	105	0.4	854	18

[a]Descriptions of how these estimates were made can be found in sections where these materials are discussed. All stack energy calculations were made assuming the anode was 70% by volume alloy, except for $Si_{66}Sn_{34}$, which was assumed to be a nonporous sputtered film. In these calculations, the irreversible capacity of the anode was assumed to match that of the cathode. The percent energy improvement over a conventional graphite coating is also listed. TCO-1 refers to $Sn_{1.0}B_{0.56}P_{0.40}Al_{0.42}O_{3.6}$.

been based on a set of metrics that does not directly relate to their implementation in practical cells. Most studies set out to make materials that improve on the specific capacity of graphite, usually without regard to average voltage, volumetric capacity, or the many other properties listed above that are more applicable to implementation in practical cells. One difficulty in choosing proper metrics for anodes stems from basic electrochemistry: it is not possible to calculate the energy of a single electrode. Cathode researchers typically estimate the volumetric "energy density" of their materials as the product of the cathode bulk density (which typically does not change in volume much during cycling) and the cathode voltage vs Li (which is close to that of graphite). Here, energy density is in quotes, because, again, the energy density of a single electrode is not defined. By using this "energy density" metric, researchers can get a rough estimate of how cathode materials can impact cell energy. However, we will show that even this estimate is a rather poor one, because it does not properly weigh the contributions of the voltage and density to the full cell energy.

It is not so simple to obtain even this rough "energy density" estimate for anode materials, because this would require defining a cathode voltage, which is hardly ever done. Therefore, usually only the gravimetric capacity (and less commonly the volumetric capacity) is given as a figure of merit for an anode material. However, improving on the specific capacity is not meaningful with respect to increasing the energy of most commercial cells. This is because cell volumetric energy is much more important than gravimetric considerations for almost all applications, including electric vehicles.[1,2] Therefore, using full cell volumetric energy as a figure of merit makes the most sense for most applications, and will be the figure of merit used here. Because many anode materials now comprise porous composites with unreported/unknown densities, we have found that there is no way to calculate how they will improve cell volumetric energy (or decrease the cell energy, in some cases!), as compared to a conventional graphite anode. This is a rather poor state of affairs, considering that alloy anode research has now been an intensely active field for almost three decades. The progress in alloy anode development has undoubtedly been severely hampered by a lack of meaningful performance metrics.

In this Review, we will attempt to compare anode materials in a meaningful way by introducing a standard model of a full cell stack, based on a cell design that we think best fits initial applications of alloy materials. Table 1 shows the results of full cell energy calculations for a number of alloys discussed throughout this Review. Using a full cell model, we have found that the energy increase one should expect from using alloys is probably much less than generally believed. Furthermore, some materials that have been reported as being promising because of their high capacity have only marginal increases (or even a decreased energy) in our cell model, as compared to graphite. Such calculations are not possible for most materials reported in the literature because of lack of information, as mentioned above. In those cases, there is no way to know how a material impacts cell energy. To ensure progress in this field, we strongly urge researchers to adopt a volumetric full cell model to estimate volumetric energy densities or at least report the volumetric capacities and average delithiation voltages of their materials. We also urge journal editors and referees to insist that this information is provided.

There have been many excellent reviews recently and over the past decades regarding the electrochemistry of alloys.[13−22] Usually reviews this late in a scientific field's evolution can simply refer to past reviews regarding the basics, as we do here, when possible. However, because this is the first time alloy materials have been reviewed on the basis of full cell energy, we have found it necessary to start from scratch. Nevertheless, there are extremely good recent reviews on alloy anode chemistry that we could not hope to improve upon. Whenever possible, we simply have cited such reviews and directed the reader there. We have also taken a decidedly pragmatic approach and concentrate on materials that have the best likelihood of being implemented in commercial cells, because of their potential to increase cell energy in a way that makes economic sense.

This Review begins by first discussing key parameters for anode performance measurement. This allows performance metrics for alloy materials to be set. Using these metrics, a standard full cell model is introduced. This model is used throughout this Review to gauge the impact of alloy anodes on cell energy. This is followed by an overview of some fundamentals of alloy anode research, including the latest

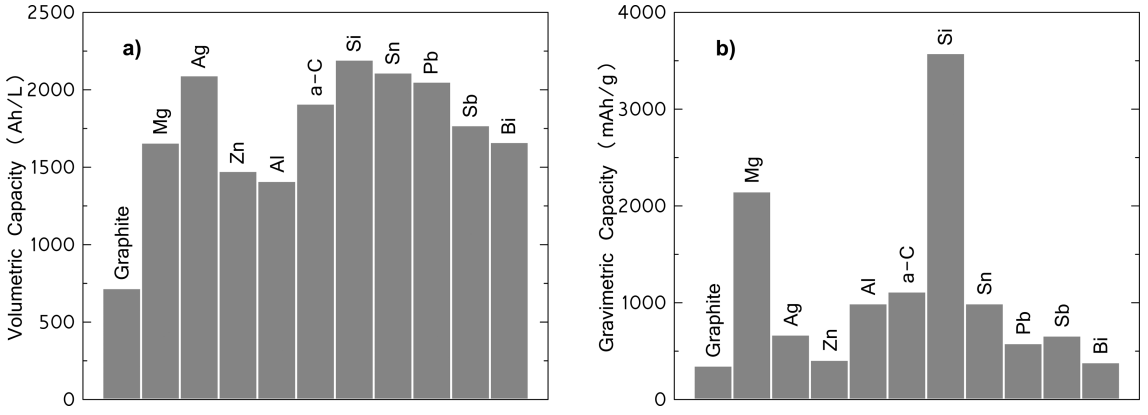


Figure 1. (a) Volumetric capacities calculated at the state of full lithiation and (b) gravimetric capacities of selected elements.

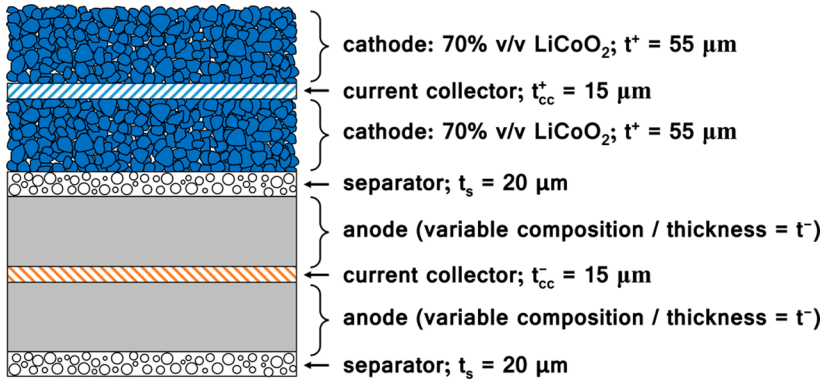


Figure 2. Cell stack used in this Review to model the impact of different anodes on cell energy density.

knowledge of the active elements and their alloys, the chemistry of effective binders and electrolyte additives, the thermal stability of alloys, and the experimental methods used for evaluating the performance of alloy electrodes. After these fundamentals, the implementation of alloys in commercial cells is discussed, including coating design and some examples of advanced alloys that have been suggested for commercialization.

What was once a small field of research a decade ago is now vast. In this Review, we have attempted to review the fundamentals of alloy chemistry with practical applications in mind, to provide a framework for applied alloy anode research. We then concentrate on the key advancements in the field and try to bring up key issues to the research community's attention. We sincerely hope that this Review will be helpful for researchers and in the progression of this field.

2. KEY PARAMETERS OF ALLOY ANODE PERFORMANCE

To provide motivation for using alloy anode materials and a framework for comparison, key performance metrics need to be defined. It is well-known that the volumetric and specific capacities of the active elements are far greater than that of graphite. Because all alloys expand considerably during lithiation, this volume must be accommodated somewhere within a battery. Therefore, for volumetric capacity values to be related to performance in practical cells, they must be calculated with respect to alloy volume at full lithiation.[23] Unfortunately, the volumetric capacity has often been calculated with respect to the volume of the active phase prior to lithiation.[17] When calculated this way, the volumetric capacity has little practical value. Figure 1a shows the volumetric capacities of various elements calculated at their state of full lithiation. The gravimetric capacity is shown in Figure 1b.

Considering that all of the elements shown in Figure 1a have more than double the volumetric capacity of graphite, it seems reasonable that using any of these elements would result in a significant increase in the energy density of Li-ion cells. This has been the viewpoint of many past reviews on this topic. However, this is not necessarily true. Better comparisons between the active elements have been made by estimating their "energy density" versus a standard cathode voltage.[23] However, this figure of merit can still be misleading, as will be discussed below. In addition, electrodes comprising alloy materials can have high irreversible capacities and high porosity. In combination, these effects can easily cause the energy of a cell with an alloy anode to be worse than a conventional graphite cell. More information is required to determine how using alloys will impact cell energy. To do this, a simple cell model is developed in the following sections, so that meaningful comparisons can be made.

2.1. A Cell-Based Model for Comparing Anode Performance

To make more informative performance comparisons, it is necessary to use a cell model, preferably one that is most representative of alloy materials application. Considering that the cycle life, Coulombic efficiency (CE), and rate capability of most alloy anodes are currently inferior to those of graphite, it is probably safe to assume that the initial applications of alloy anodes will be in energy cells for small consumer devices, where device size is paramount and weight is of secondary importance. Therefore, we have chosen a Li-ion energy cell to estimate the impact of alloy anodes on the basis of volumetric energy. Because, as mentioned above, volumetric energy is much more

dx.doi.org/10.1021/cr500207g | Chem. Rev. 2014, 114, 11444−11502

Table 2. Parameters Describing the Baseline Cell Stack Used To Compare Anode Materials[a]

electrode properties							
electrode	density (g/mL)	$V_{average}$	RC (mAh/g)	IC	AV	expansion	coating thickness (μm)
cathode	5.05	3.9 V	150	6%	70%	~0%	55
anode	2.26	125 mV	350	6%	70%	10%	
separator/current collector/cell balance							
current collector thickness (μm)						15	
separator thickness (μm)						20	
N/P						1.1	

[a]Here, the density is the active material density, RC is active material reversible capacity, IC is active material irreversible capacity, AV is active volume in coating, and N/P is the ratio of the negative and positive electrode capacities.

important than gravimetric energy in most battery applications, including electric vehicles,[1,2] using volumetric full cell energy should apply as a figure of merit for most other applications as well.

Commercial Li-ion energy cells come in a large variety of formats. Therefore, we have simply modeled a cell stack, shown in Figure 2, so that the volumetric energy density can readily be scaled to cells of different size. As a baseline, a $LiCoO_2$ cathode and a graphite anode, both being 70% by volume active material, were used. The parameters of the baseline cell stack are listed in Table 2. If the cell component thicknesses are defined as in Figure 2, then the total cell thickness is given by

$$t = t_{cc}^{+} + t_{cc}^{-} + 2(t^{+} + t^{-} + t_{s}) \tag{1}$$

Figure 3 shows the voltage curve of a full cell that is balanced with a negative to positive capacity ratio of N/P. Typically, the

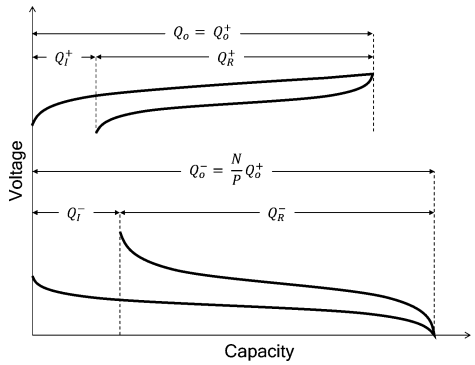


Figure 3. Voltage curve of an anode and cathode in a full cell, illustrating the various capacity definitions described in the text.

value of N/P is about 1.1−1.2 in commercial cells. The excess negative capacity is required so that lithium plating can be avoided. The values of the initial charge capacity, initial cathode charge capacity, reversible cathode capacity, and irreversible cathode capacity of the cell stack are indicated in the figure as Q_o, Q_o^+, Q_R^+, and Q_I^+, respectively. Using this formalism:

$$Q_o^{+} = Q_R^{+} + Q_I^{+} \tag{2}$$

and

$$Q_R^{+} = Q_o^{+}\varphi_o^{+} \tag{3}$$

where φ_o^+ is the cathode initial Coulombic efficiency (ICE). Similar definitions are made for the analogous negative electrode quantities.

It is important to realize some key design restrictions that are inherent to conventional Li-ion cells. Given that the overall cell volume for a given format is fixed, the volumetric capacity of the electrodes is calculated at their full volume expansion. In addition, the cathode thickness in commercial cells is limited by kinetic factors.[24] Therefore, increasing the cathode thickness to match the increased capacity of an alloy anode is not usually possible. Accordingly, in our cell energy calculations, the cathode coating thickness remains fixed at 55 μm. This sets the area specific initial cell capacity, $\bar{Q}_o$, and area specific initial cathode capacity, $\bar{Q}_o^+$, as

$$\bar{Q}_o = \bar{Q}_o^{+} = 2\tilde{q}_o^{+}t^{+} \tag{4}$$

where $\tilde{q}_o^+$ is the cathode coating volumetric capacity and the factor of 2 is present because the cathode is double-sided. Here, a bar ($^-$) indicates capacity per electrode unit area, and a tilde ($\tilde{}$) represents capacity per unit coating volume. Similarly, the cathode reversible area specific capacity is given by

$$\bar{Q}_R^{+} = 2\tilde{q}_R^{+}t^{+} \tag{5}$$

Using this formulism, the anode initial area specific capacity may be written as

$$\bar{Q}_o^{-} = \bar{Q}_o^{+}\left(\frac{N}{P}\right) = \frac{\bar{Q}_R^{+}}{\varphi_o^{+}}\left(\frac{N}{P}\right) = \frac{2\tilde{q}_R^{+}t^{+}}{\varphi_o^{+}}\left(\frac{N}{P}\right) \tag{6}$$

and the anode area specific reversible capacity is

$$\bar{Q}_R^{-} = \bar{Q}_o^{-}\varphi_o^{-} = 2\tilde{q}_R^{+}t^{+}\frac{\varphi_o^{-}}{\varphi_o^{+}}\left(\frac{N}{P}\right) \tag{7}$$

The anode area specific reversible capacity is also given by

$$\bar{Q}_R^{-} = 2\tilde{q}_R^{-}t^{-} \tag{8}$$

This defines the anode coating thickness as

$$t^{-} = t^{+}\frac{\tilde{q}_R^{+}\varphi_o^{-}}{\tilde{q}_R^{-}\varphi_o^{+}}\left(\frac{N}{P}\right) \tag{9}$$

Putting eq 9 into eq 1 allows the cell stack thickness to be calculated in terms of the cathode coating thickness, the anode and cathode reversible capacities, and the ICE of the anode and cathode.

Referring to Figure 3, the value of the cell irreversible capacity, Q_I, is equal to whichever of Q_I^+ or Q_I^- is biggest (Figure 3 shows the case when Q_I^- is bigger than Q_I^+, which is typical for alloy anode materials), therefore

$$\bar{Q}_I = \max\{\tilde{Q}_I^{+}, \tilde{Q}_I^{-}\} = \max\{2\tilde{q}_R^{+}(1-\varphi_o^{+})t^{+}, 2\tilde{q}_R^{-}(1-\varphi_o^{-})t^{-}\} \tag{10}$$

dx.doi.org/10.1021/cr500207g | Chem. Rev. 2014, 114, 11444−11502

Table 3. Characteristics of Alloys of Lithium with Various Elements[a]

element	lithiated phases	x in Li_xM	expansion (%)	voltage (V)		capacity mAh/g	capacity Ah/L	in full cell: average voltage[b] (V)	in full cell: stack energy (Wh/L)	in full cell: energy increase (%)	comments
baseline (graphite)		0.17	10	0.2−0.1		350	719	0.125	726	0	
Mg	Li_xMg	0−1.95	0−125	0.0325	AVG[25]	0−2150	0−1658	0.0325	1032	42	
Ag	α-$Li_{0.9}Ag$	0−0.87	0−76	0.26−0.19	GITT[26]	0−216	0−1288				γ_2-Li_5Ag not considered; x in Li_xAg estimated from ref 26
	β-$Li_{1.3}Ag$	1.04−1.27	91−111	0.186	GITT[26]	258−315	1419−1568				
	γ_3-$Li_{2.7}Ag$	1.74−2.7	152−236	0.18−0.067	GITT[26]	432−670	1798−2093	0.175	1031	42	
Zn	Li_2Zn_5	0.40	39	0.490	AVG[27]	164	840				
	$LiZn_2$	0.50	49	0.256	GITT[28]	205	981				
	Li_2Zn_3	0.67	65	0.219	GITT[28]	273	1179				
	LiZn	1.00	98	0.157	GITT[28]	410	1476	0.310	937	29	
Al	LiAl	1.00	90	0.380	GITT[29]	993	1411	0.38	911	25	
C	a-Li_xC	0−0.5	0−31	1.75−0	AVG[30]	0−1115	0−1910	0.875	826	14	volume expansion estimated from ref 31
Si	$Li_{15}Si_4$	3.75	280	0.400	GITT[32]	3579	2194	0.400	976	34	
Sn	Li_ySn	0.40	22	0.760	GITT[33‡]	90	540				‡estimated from value shown in ref 33; results from ref 33 and suggested lithiation mechanism do not precisely match
	Li_ySn	0.70	39	0.660	GITT[33]	158	832				
	Li_ySn	2.33	129	0.530	GITT[33]	527	1678				
	Li_ySn	2.63	146	0.485	GITT[33]	594	1765				
	Li_ySn	3.50	194	0.420	GITT[33]	790	1964				
	Li_ySn	4.40	244	0.380	GITT[33]	993	2111	0.504	941	30	
Pb	LiPb	1.00	49	0.601	GITT[28]	129	983				
	$Li_{1.5}Pb$	1.50	74	0.449	GITT[28]	194	1265				
	$Li_{2.5}Pb$	2.50	123	0.449	GITT[28]	323	1643				
	Li_3Pb	3.00	148	0.374	GITT[28]	388	1776				
	$Li_{3.5}Pb$	3.50	172	0.292	GITT[28]	453	1885				
	$Li_{4.5}Pb$	4.50	222	0.294	GITT[28]	582	2052	0.423	960	32	
Sb	Li_3Sb	3.00	147	0.948	GITT[33]	660	1771	0.948	796	10	
Bi	LiBi	1.00	42	0.810	GITT[33]	128	883				
	Li_3Bi	3.00	126	0.828	GITT[33]	385	1662	0.822	821	13	

[a]Where possible, equilibrium voltages as measured by the galvanostatic intermittent titration technique (GITT) were used. When hysteresis occurred, GITT values as measured during the delithiation half-cycle were used. Where GITT values did not exist, the voltage was estimated as the average voltage between the lithiation and delithiation half-cycle voltage curves (denoted as AVG in the table above). Cell stack energies were calculated according to the model described in the text. The % increase in energy is given with respect to the baseline cell described in Table 2. [b]Average voltages were estimated by averaging alloy equilibrium voltages over the entire voltage curve.

dx.doi.org/10.1021/cr500207g | Chem. Rev. 2014, 114, 11444−11502

and the reversible area specific cell capacity is given by

$$\bar{Q}_R = \bar{Q} - \bar{Q}_I \quad (11)$$

Using the value of $\bar{Q}_R$ and the stack thickness, the volumetric cell capacity may be calculated in terms of the cathode coating thickness, the anode and cathode reversible capacities, and the ICE of the anode and cathode as

$$\check{Q}_R = \bar{Q}_R/t \quad (12)$$

The stack energy density, $\check{U}_R$, is then given by

$$\check{U}_R = \check{Q}_R V_{avg} \quad (13)$$

where V_{avg} is the average cell discharge voltage and where ˇ indicates per unit stack volume. If it can be approximated that the cathode voltage is constant, and that the small excess capacity of the anode can be neglected in voltage calculations, then V_{avg} will be the difference between the cathode voltage and the average anode delithiation voltage or:

$$V_{avg} \approx V^+_{avg} - V^-_{avg} \quad (14)$$

From this exercise, it can be seen that the anode coating reversible volumetric capacity at full lithiation, the anode initial Coulombic efficiency (or percent irreversible capacity), and the anode average voltage are absolutely necessary to gauge the impact an anode material will have on the energy stored in a full cell. The energy stored by different cell formats can be easily computed by multiplying the cell stack energy density by the total stack volume in a cell. For instance, the baseline $LiCoO_2$/graphite cell described in Table 2 has a stack energy density of 726 Wh/L. Therefore, this cell stack in an 18650 cell having 17 mL total volume and 15.3 mL stack volume will have a cell energy of 11.1 Wh, which is comparable to that of commercial high energy density 18650 cells.

2.2. Full Cell Volumetric Energy Comparison of the Active Elements

The cell model developed in section 2.1 is useful to compare the performance of anode materials by observing how the cell energy changes when different anode materials are substituted for graphite. Here, this model is used to evaluate the impact of using anodes that comprise elements that alloy with lithium on the cell energy. In this calculation, the volumetric capacity, volume expansion, and average voltage of the active elements were derived from the values listed in Table 3, which are discussed in detail in section 3.1. The cathode thickness was fixed at 55 μm for all cells. The anode was assumed to be comprised entirely of the active element (e.g., a thin film) with zero porosity. The impact of porosity and electrode inactive volume is discussed in section 2.3. Because the irreversible capacity is highly dependent on surface area, binders, electrolytes, rate, etc., and because there may be methods to deal with anode irreversible capacity (as discussed in section 7.1), for the purposes of this calculation the anode irreversible capacity was chosen to match exactly that of the cathode (this gives the same energy as if the cell has zero irreversible capacity, assuming the irreversible capacity does not occupy volume in the cell). Using these assumptions in eqs 1−14, the stack energy density simplifies to

$$\check{U}_R = \frac{2\tilde{q}^+_R t^+}{t^+_{cc} + t^-_{cc} + 2t_s + 2t^+\left[1 + \frac{\tilde{q}^+_R}{\tilde{q}^-_R}\left(\frac{N}{P}\right)\right]}(V^+_{avg} - V^-_{avg}) \quad (15)$$

In the case of our cell model, inserting the values from Table 2 into eq 15 results in a simple equation that can be used to estimate the cell stack energy density of an anode (in Wh/L) with a reversible coating volumetric capacity $\tilde{q}^-_R$ (in Ah/L) and average voltage V^-_{avg} (in volts):

$$\check{U}_R = \frac{(58\,327.5\ \text{Ah/L})}{70 + (110)\left[1 + \frac{(58\,327.5\ \text{Ah/L})}{\tilde{q}^-_R}\right]}[(3.9\ \text{V}) - V^-_{avg}] \quad (16)$$

For instance, a Si thin film electrode with no porosity has a reversible volumetric capacity of 2194 Ah/L and an average voltage of 0.4 V, as discussed in section 3.6. Substituting these values into eq 16 as $\tilde{q}^-_R$ and V^-_{avg}, respectively, results in a stack energy density of $\check{U}_R$ = 976 Wh/L. This represents a 34% increase in volumetric energy as compared to the baseline $LiCoO_2$/graphite cell of 726 Wh/L, described above.

The results of similar calculations for various active elements are listed in Table 3 and are shown graphically in Figure 4, in which the stack energy is plotted for different negative electrode active materials. To provide a popular frame of reference, a scale is also provided that indicates the cell energy that results when the stack is used in an 18650 cell format. This calculation assumed zero anode porosity. The impact of porosity and irreversible capacity on cell energy will be discussed in section 2.3.

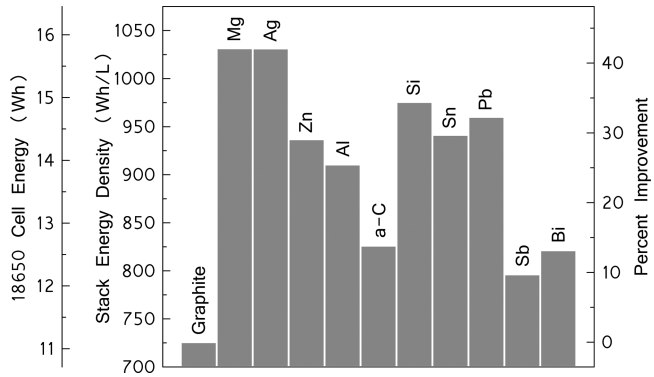


Figure 4. Calculated stack energies for different negative electrode active materials. The right-hand side axis indicates the percent improvement in energy over a graphite electrode. A scale was also provided with 18650 cell energies based on the model.

Figure 4 is quite instructive. First, the maximum increase in energy one can expect by replacing graphite with an alloy (i.e., zero porosity Ag with no irreversible capacity) in a conventional Li-ion cell is quite modest: only about 42%, corresponding to a 15.8 Wh 18650 cell. This result is highly dependent on the cathode thickness and capacity. If either of these parameters is increased even by small amounts, the cell energy can be significantly increased. Nevertheless, the energy gains shown in Figure 4 are difficult to achieve in practice. If composite coatings are used that include active particles, porosity, and other inactive phases or if their irreversible capacity is considered (as is discussed below), the stack energy densities can be significantly less than shown in Figure 4. Therefore, only the elements that result in the highest cell energies remain attractive for alloy anode material design.

Another result from Figure 4 is that the order of the active elements that result in the highest energy densities is completely different than what is predicted from only considering volumetric

or specific capacities.[16,17,20,34] This can be readily seen by comparing Figure 4 with Figure 1a. The reason for this, of course, is because the anode voltage is now being considered. The negative electrode "energy density", which has been calculated as the product of a standard cathode voltage versus the anode average voltage and the anode expanded volumetric capacity,[23] is also not consistent with the relative cell energies in Figure 4. This is because the real energy density of a cell stack is proportional to the cell voltage divided by the cell stack volume. Because the active anode material is a rather small portion of the total stack volume, the anode volume has less effect on the cell energy than the anode voltage. This can be appreciated upon inspection of eq 16.

The result of the above discussion is that the energy of a full cell will be heavily weighted on the anode cell voltage and less so on the anode volumetric capacity. This is why Ag and Mg, which have the lowest average voltage of the active elements considered here, have the highest predicted stack energy density. Conversely, elements with high average voltage fare poorly in a realistic cell energy calculation. This is especially true for Sb. Although Sb has a midrange volumetric capacity in Figure 1a, it has the highest average voltage, and, accordingly, the lowest theoretical stack energy density of all of the active elements considered here. The present model predicts only a 10% gain in cell energy if Sb is used as an anode with zero inactive volume and irreversible capacity. If other factors that lower the energy further from this ideal model are considered, the use of Sb-based alloys has little impact on increasing cell energy over a conventional graphite electrode, according to our model. In addition, equilibrium voltages were used in our cell energy calculations. In practice, alloys cycling at constant current can have significantly higher delithiation voltages, reducing cell energy further. Therefore, the use of Sb-based alloy anodes might not result in any significant full cell energy improvement over graphite, as has been pointed out in the past.[33]

The active elements that result in the highest stack energy density according to Figure 4 are Ag ≈ Mg > Si > Pb > Sn. Of these, Ag is likely too expensive for use as the primary element in an alloy for mass market commercial cells. Mg has low rate capability, and this combined with its ultralow voltage may make it susceptible to Li-plating during charge (see section 3.1.2.1). Pb is less attractive because of its toxicity. This leaves Si and Sn as likely for use as the primary active element in alloy anodes, and by far most of the research on alloy anodes has focused on Si- and Sn-based materials. Accordingly, Si- and Sn-based alloys will form the basis of this Review. However, the other active elements may be highly valuable as components of Si- or Sn-based alloys and will be discussed in this context.

2.3. Electrode Porosity, Irreversible Capacity, and Coulombic Efficiency

Alloy electrodes can have significantly higher electrode porosity, higher irreversible capacity, and lower CE than conventional graphite coatings.[35] These factors can result in lowered energy density or poor cycling performance. Figure 5 shows the separate impacts of anode irreversible capacity and inactive volume (which can include porosity, binders, and conductive diluents) on the stack energy, when a silicon anode is used. The cell energy decreases monotonically with increasing inactive volume. The cell energy initially increases with increasing anode irreversible capacity. A maximum value of cell energy is reached when the irreversible capacities of the cathode and anode are equal.

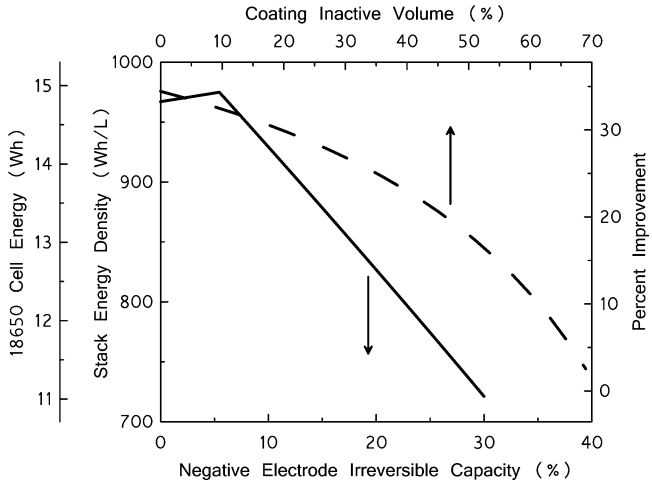


Figure 5. Stack energy density and the percent energy improvement (over a conventional graphite cell) as a function of anode inactive volume and irreversible capacity for the cell stack described in the text, using a silicon anode. A scale is also provided with 18650 cell energies based on the model.

Increasing the anode irreversible capacity further results in a reduction of cell energy.

Both the porosity and the irreversible capacity can combine to drastically reduce cell energy and should be taken into consideration when calculating energy density. For instance, according to our model, a full cell having a Si anode with 30% inactive volume (4% binder volume, 1% conductive diluent, 25% porosity, for example) and 25% irreversible capacity results in no energy gain over a conventional graphite cell. These values of inactive volume and irreversible capacity are small in comparison to much of the published work in this field. Serious attention to electrode inactive volume and irreversible capacity is needed to develop practical electrodes. Methods of reducing the irreversible capacity and the inactive volume are discussed in sections 7.1 and 7.2.

The CE also should be taken into consideration in anode development. Its impact is often ignored or underestimated. It can also be difficult to measure, especially in half-cells. Alloy materials can often have low CEs due to reactivity with electrolyte, particle fracture, or particle disconnection (see sections 4 and 5). As an illustration of the impact of the CE on cycle life in a full cell, Figure 6 shows the capacity retention versus cycle number of a full cell calculated using different values of the anode CE, as indicated in the figure. The cathode CE was assumed to be 100%. Figure 6 demonstrates how capacity fade in a full cell can quickly become unacceptable as a result of only small changes in the CE. Coulombic efficiencies of 99.99% and 99.95% resulted in 5% and 22% capacity loss after 500 cycles, respectively. The huge impact of even small reductions in the CE on full cell cycling does not seem to be widely appreciated.

3. FUNDAMENTALS OF Li INSERTION IN METALS AND ALLOYS

3.1. The Active Elements

Figure 7 highlights the elements that are known to form compounds with lithium. The elements that we considered for this Review are highlighted in blue. The elements that were not considered are highlighted in red. Essentially we have tried to concentrate on those elements that are most likely to be used in

dx.doi.org/10.1021/cr500207g | Chem. Rev. 2014, 114, 11444−11502

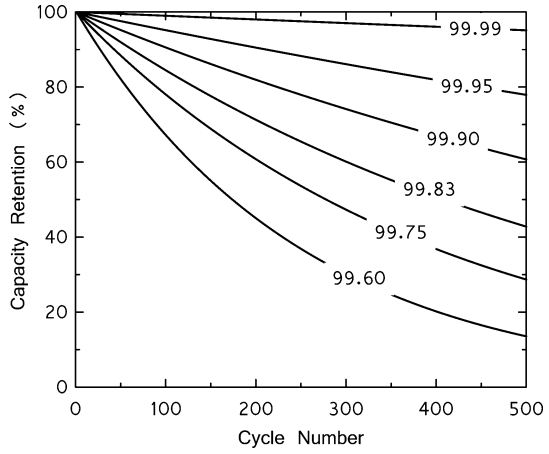


Figure 6. Effect of the anode CE on the capacity retention of a full cell. The cathode CE was assumed to be 100%.

practical consumer cells and have avoided elements that are highly toxic, expensive, or have high voltages. Nevertheless, many of the elements in Figure 7 that we include in this Review likely have too high voltage or low capacity to be considered as a primary anode material. However, they are of interest because they can form an effective matrix phase during lithiation or interact with high capacity, low voltage elements, such as Si or Sn, to significantly alter their electrochemistry, and, in some cases, enhance performance. Therefore, such elements are important to discuss from the perspective of their use as potential "additive elements" in practical alloy materials.

3.1.1. Hydrogen and the Alkali Metals. Of the group 1 elements only hydrogen is known to form compounds with lithium. Li is known to react with hydrogen reversibly via conversion reactions with metal hydrides, such as MgH_2 and TiH_2, according to

$$AH_2 \overset{Li}{\rightarrow} A + 2LiH \quad (17)$$

where A is Mg or Ti.[36−38] An ∼89% volume expansion is associated with this conversion reaction, which is believed to be the cause of limited cycling performance. Using the bulk densities of Mg (1.74 g/mL) and LiH (0.78 g/mL), we calculate the theoretical volumetric capacity of MgH_2 to be about 1561 Ah/L. With an average voltage of 0.5 V during delithiation,[36] this corresponds to a 831 Wh/L stack energy density according to our standard cell model or a 14% improvement over graphite. This is quite good; however, to our knowledge, the thermal stability of hydrides in Li-ion cells is unknown and still needs investigation.

3.1.2. The Alkaline Earth Metals. The lithiation of alkaline earth metals has received little study. Poor kinetics and air reactivity may prohibit the use of these metals as principal components of negative electrodes. However, Mg has been studied extensively as a component in alloys, especially with silicon, significantly altering its voltage curve (see section 3.7.1.1.2). To develop such alloys, a better understanding of the alkaline earth metals is warranted.

3.1.2.1. Magnesium.

$$Mg \overset{Li}{\leftrightarrow} (Mg) \overset{Li}{\leftrightarrow} (Li) \quad \textit{Reference 39}$$

Li and Mg have large solid solution regions at room temperature, according to their equilibrium binary phase diagram, shown in Figure 8.[40] A Mg-rich phase exists with up to 15 atomic % Li, and a Li-rich alloy exists with a minimum of 30 atomic % Li. These phases are separated by a two-phase coexistence region. Because the lithium-rich solid solution phase extends to lithium metal, the theoretical capacity of Mg is infinite. Mg is the only element that has this property.[40] Magnesium's ability to form extended solid solutions with lithium presents a different lithiation mechanism as compared to most active elements, which mainly form binary lithium compounds. Few studies of this interesting system have been reported. High impedance surface films on the Mg surface make electrochemistry at this electrode difficult to achieve.[39,41] Kim et al.[25] and Park et al.[39] reported low rate capability for the lithiation of Mg, with a maximum lithiation current of only 10 mA/g. The voltage curve of Li in Mg is shown in Figure 9. The maximum achievable reversible capacity was 2150 mAh/g, corresponding to a composition of about $Li_{1.95}Mg$.[25] The average voltage is quite low, being about 18 mV for lithiation and 50 mV for delithiation, respectively. Although normally attractive in anode materials, the exceedingly low average voltage of Mg, coupled with its low rate capability, may create a high chance for lithium plating during charge in full cells.

Park et al. demonstrated significantly increased rate capability in Mg−C ball milled composites with good capacity retention in half cells for the 20 cycles reported.[39] They also confirmed that the lithiation reaction follows the equilibrium phase diagram, with the reversible formation of Mg, and the Mg-rich and Li-rich phases being observed during cycling by ex situ X-ray diffraction (XRD).

3.1.2.2. Calcium and Strontium Lithiation Mechanism Unknown. $CaLi_2$ is the only binary compound that exists below 141 °C in the Ca−Li system.[40] This compound has a theoretical capacity of 1337 mAh/g or 1030 Ah/L. Only one study could be found that investigated the lithiation of pure calcium.[42] A first cycle capacity of only 400 mAh/g was achieved for a composite coating cycled between 5 mV and 1.5 V, with subsequent cycles having rapid capacity fade. No voltage curve was shown. It was only mentioned that "pure Ca powder showed several distinct regions with insertion beginning at about 0.3 V." This does not correlate with the single plateau that would be expected from the

H																	He
Li	Be												B	C	N	O	F	Ne
Na	Mg												Al	Si	P	S	Cl	Ar
K	Ca		Sc	Ti	V	Cr	Mn	Fe	Co	Ni	Cu	Zn	Ga	Ge	As	Se	Br	Kr
Rb	Sr		Y	Zr	Nb	Mo	Tc	Ru	Rh	Pd	Ag	Cd	In	Sn	Sb	Te	I	Xe
Cs	Ba	La +	Lu	Hf	Ta	W	Re	Os	Ir	Pt	Au	Hg	Tl	Pb	Bi	Po	At	Rn
Fr	Ra	Ac +	Lr	Rf	Db	Sg	Bh	Hs	Mt	Ds	Rg	Cn	Uut	Fl	Uup	Lv	Uus	Uuo

Figure 7. Periodic table with the known active elements highlighted in red and blue. The elements in blue are included in this Review. The elements in red are not included.

dx.doi.org/10.1021/cr500207g | *Chem. Rev.* 2014, 114, 11444−11502

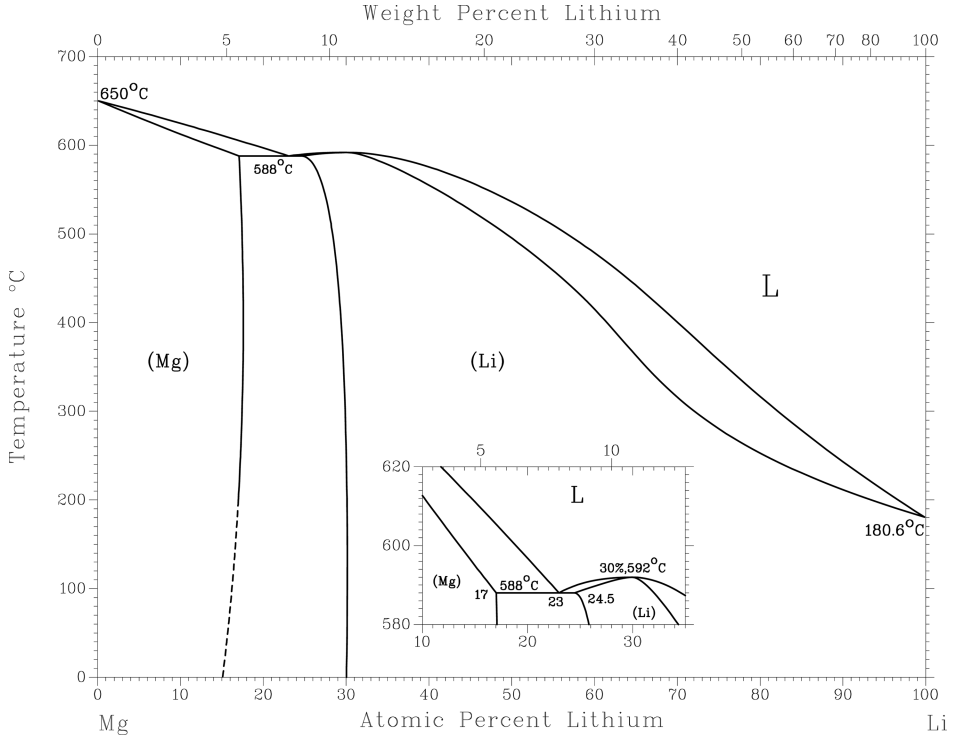


Figure 8. Li−Mg system. Reprinted with permission from ref 40. All rights reserved, www.asminternational.org. Copyright 1996 ASM International.

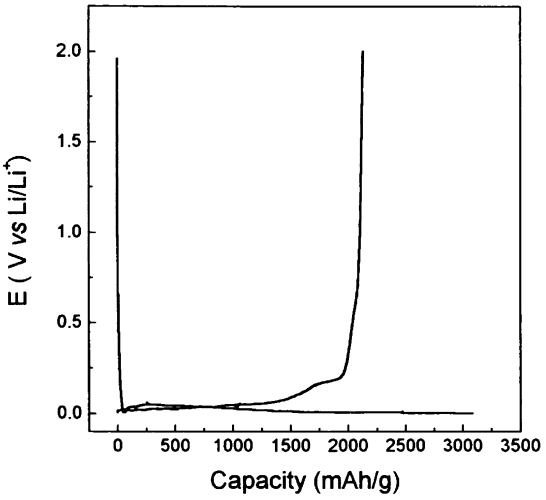


Figure 9. Voltage curve of a Mg electrode at a constant current of 5 mA/g. Reprinted with permission from ref 25. Copyright 2000 Elsevier.

known Ca−Li phase system. More studies are required to understand this system.

Theoretically, strontium can store much more lithium than any other alkali metal. Two binary compounds, Li_2Sr_3, $Li_{23}Sr_6$, have been confirmed to form in the Li−Sr system below 134 °C, although more intermetallic phases may exist.[40] $Li_{23}Sr_6$ has a theoretical capacity of 900 mAh/g or 1223 Ah/L. To our knowledge, no room temperature electrochemical lithiation studies of strontium have been reported.

3.1.3. The Transition Metals. Excepting Zn and Ag, only very precious or toxic transition metals form alloys with lithium: Ru, Rh, Pd, Cd, Ir, Pt, Au, and Hg.[40] These are not included in this Review, because the likelihood of their incorporation in practical negative electrode materials, even in small amounts, is probably low. Readers interested in the lithiation of these materials are referred to the following studies: Pd,[43] Cd,[28,44,45] Pt,[46−48] Au,[49−52] Hg.[47,53] To our knowledge, the lithiation of Ru, Rh, and Ir has not been reported.

3.1.3.1. Silver.

$$Ag \overset{Li}{\leftrightarrow} (Ag)\sim(Ag{-}Li_{0.9}Ag) \overset{Li}{\leftrightarrow} \beta\sim(LiAg{-}Li_{1.3}Ag)$$
$$\overset{Li}{\leftrightarrow} \gamma_3\sim(Li_{1.7}Ag{-}Li_{2.7}Ag) \overset{Li}{\leftrightarrow} \gamma_2{*}\sim(Li_{3.5}Ag{-}Li_5Ag)$$

**Only formed in trace amounts, from ref 26.*

Despite being a precious metal, Ag has been suggested as a candidate active material for alloy negative electrodes because of its high conductivity, high theoretical capacity, and low average voltage.[26,54] Figure 10 shows the binary Ag−Li phase diagram. Ag is unique in that it forms a number of intermetallic phases with lithium with extended solid solution regions. The γ_1 phase, with nominal composition $Li_{12}Ag$, has the highest lithium content of all of the binary lithium intermetallic phases.[40]

Taillades and Sarradin predicted that the lithiation of Ag proceeds as described by the Ag−Li binary phase diagram by comparing the phase diagram with the galvanostatic intermittent titration (GITT) curve of the lithiation of a silver thin film (shown in Figure 11), excepting that only the γ_2 phase could be achieved at maximum lithiation.[26] The minimum Li composition in the γ_2 phase was also found to be richer than predicted by the equilibrium phase diagram ($Li_{3.5}Ag$ as opposed to $Li_{3.2}Ag$). Later, a detailed ex situ XRD study by Park et al. confirmed that the lithiation of nano-Ag particles proceeds as described by the equilibrium binary phase diagram, but terminates at the γ_2 composition.[54] Taillades and Sarradin also showed that thin film silver could be reversibly cycled 150 times without capacity loss, when limiting cycling voltages of 0.150−0.015 V were used.[26] However, this was achieved at a cycling rate at which only a fraction of the capacity of the Ag film was accessed during each cycle.

3.1.3.2. Zinc.

dx.doi.org/10.1021/cr500207g | *Chem. Rev.* 2014, 114, 11444−11502

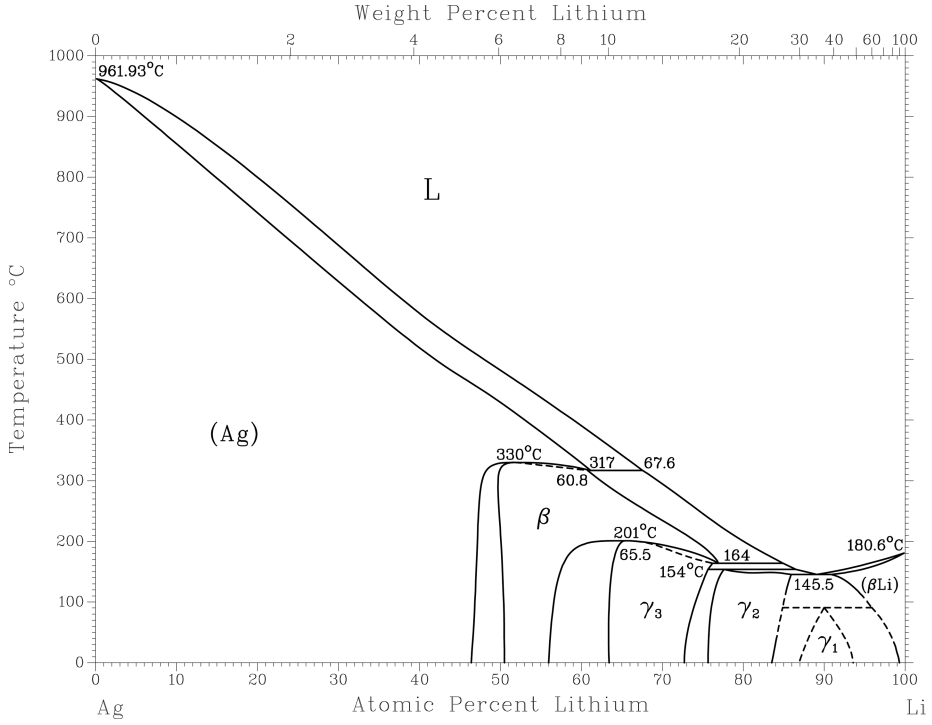


Figure 10. Ag–Li system. Reprinted with permission from ref 40. All rights reserved, www.asminternational.org. Copyright 1996 ASM International.

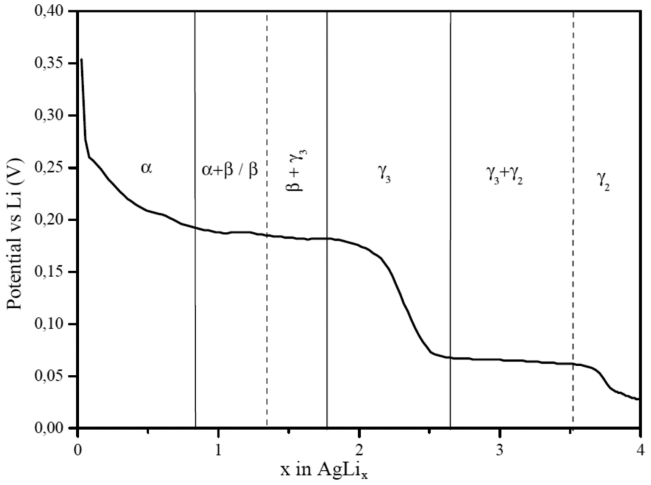


Figure 11. GITT curve of a silver thin film electrode during the alloying process. Pulse duration, 0.1 h; pulse intensity, 15 μA; open circuit potential time derivative, 5 mV/h. Reprinted with permission from ref 26. Copyright 2004 Elsevier.

$$\textit{lithiation:}\quad Zn \xrightarrow{Li} \alpha\text{-}LiZn_4 \xrightarrow{Li} \alpha\text{-}Li_2Zn_3 \xrightarrow{Li} LiZn$$

$$\textit{delithiation:}\quad LiZn \xrightarrow{-Li} \alpha\text{-}Li_2Zn_3 \xrightarrow{-Li} LiZn_2 \xrightarrow{-Li} \alpha\text{-}Li_2Zn_5 \xrightarrow{-Li} \alpha\text{-}LiZn_4 \xrightarrow{-Li} Zn$$

Reference 27.

Relatively few studies of zinc lithiation have been reported. Hwa et al. have recently shown by in situ X-ray diffraction measurements that room temperature zinc lithiation follows the mechanism shown above.[27] According to this mechanism, the Li–Zn binary phase diagram is followed during delithiation, but the $LiZn_2$ and α-Li_2Zn_5 phases were not formed during lithiation. At full lithiation, Hwa et al. suggest that the LiZn phase can accommodate a significant amount of nonstoichiometry, up to a lithium content of $Li_{1.27}Zn$.[27] Very poor kinetics were noted in the Li–Zn system when $x < 0.4$ in Li_xZn.[28] Thin films of crystalline zinc were found to have poor cycle life in lithium batteries, even if the lithiation level was severely restricted.[55] During cycling of sputtered Zn electrodes, poor Coulombic efficiency and "electrode slippage" have been observed that are suggestive of lithium consuming reactions occurring on the Zn surface.[30] From the studies reported so far, the incorporation of Zn in practical alloy negative electrodes does not seem promising.

3.1.4. The p-Block Elements. All of the p-block elements form compounds with lithium, excepting the noble gases. This Review will be restricted to the metals and metalloids in the p-block, including carbon. Oxygen is discussed with respect to its matrix forming ability in SiO and Sn–oxide materials, which are discussed in sections 7.3.2 and 3.7.2.7, respectively. Ga, Ge, In, Tl, As, and Te were considered either too toxic or expensive to be included within the scope of this Review. Readers interested in the lithiation of these elements and their compounds are encouraged to look in the following sources: Ga,[56–58] Ge,[16] In,[20,59,60] As,[61] Te.[62] We are not aware of any studies of the lithiation of Tl or its alloys.

3.1.4.1. Boron. almost inactive at room temperature[63]

Five equilibrium phases are reported to exist in the B–Li system: $B_{0.8-1.0}Li$, B_3Li, $B_{14}Li_3$, $B_{6-7}Li$, and $B_{10-13}Li$.[64] These compounds are generally composed of connected boron polyhedra with the Li residing in the resulting cavities.[65] These systems are attractive for Li storage because of their high theoretical volumetric and gravimetric capacities and because their open structures that support nonstoichiometries are suggestive of being amenable toward intercalation.[64]

Boron lithium alloys having about 70 atomic % Li have long been known to operate as reversible negative electrodes at intermediate temperatures (400–600 °C).[66–71] At these temperatures, such alloys consist of molten lithium held within

dx.doi.org/10.1021/cr500207g | Chem. Rev. 2014, 114, 11444–11502

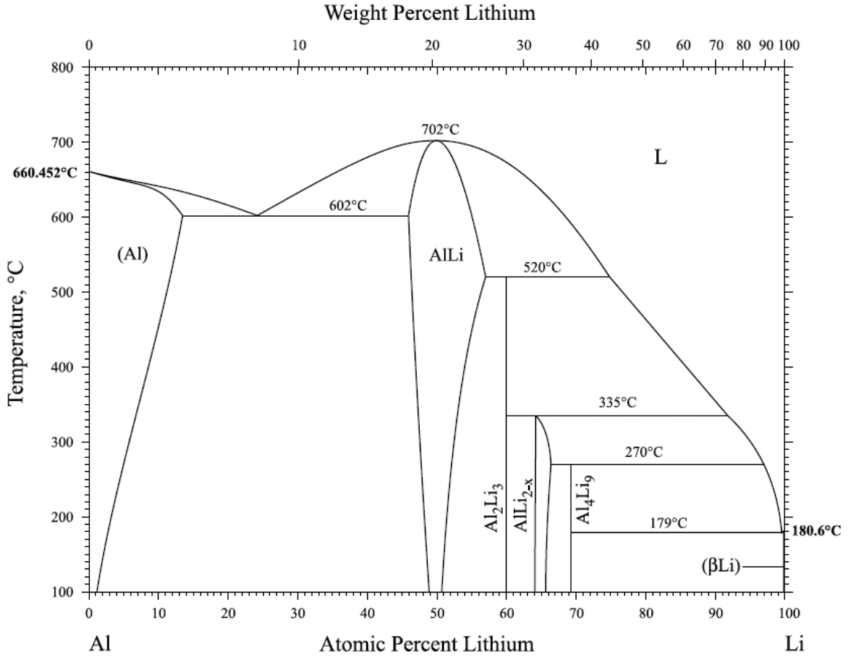


Figure 12. Al−Li phase diagram. Reproduced with permission from ref 76. Copyright 2012 ASM International from Springer Science and Business Media.

a solid porous matrix of Li_7B_6 by surface tension, resulting in a ductile material.[69,71] However, low capacities have been reported for the lithiation of boron at ambient temperatures. Huggins et al. reported the insertion of 0.01 mol of Li into boron at room temperature with little reversibility.[63] Reversible insertion of Li into thin films of B_{50} was demonstrated by Ding et al. between 0.01 and 3.0 V, resulting in a high average voltage.[72] The gravimetric capacity of the boron films was low, being only 44 mAh/g at 25 °C and increasing to 268 mAh/g at 85 °C.[72]

3.1.4.2. Aluminum.

$$Al \overset{Li}{\leftrightarrow} (Al) \overset{Li}{\leftrightarrow} \beta\text{-}AlLi \overset{Li}{\leftrightarrow} Li_3Al_2/Li_9Al_4?$$

References 29, 73−75.

The Al−Li binary system is shown in Figure 12. Five equilibrium binary phases are reported to exist in this system: α-(Al), β-AlLi, Al_2Li_3, $AlLi_2$, and Al_4Li_9.[76] At temperatures between 415 and 505 °C, lithiation of Al results in the formation of α-(Al), β-AlLi, and Al_2Li_3 phases, in agreement with the equilibrium phase diagram.[77] The room temperature voltage curve of aluminum is shown in Figure 13. The voltage curve is mainly comprised of a single plateau corresponding to the formation of β-AlLi. This has been confirmed by X-ray diffraction measurements.[73,74] Extra capacity beyond this plateau has been attributed to the formation of higher lithiated phases of Al that form on the surface of β-AlLi.[29,74,75] It is thought that such phases are impeded from growing into the bulk because of poor diffusion.

3.1.4.3. Amorphous Carbon.

$$a\text{-}C \overset{Li}{\leftrightarrow} a\text{-}Li_{0.5}C$$

References 30, 78, 79 ("a" indicates an amorphous phase).

In keeping with the alloying theme of this Review, the intercalation of lithium into common carbonaceous hosts (e.g., graphite, hard/soft carbons, etc.) will not be discussed. The intercalation mechanism of lithium into these materials is well-known. However, the lithiation of amorphous carbon (denoted here as a-C), which is a component in important alloy systems, has only recently been studied. Dahn et al. found that Sn−Co−C alloys made by ball milling and combinatorial sputtering comprise a Sn−Co alloy phase and an amorphous carbon phase (see also section 7.3.1).[78] By measuring the capacity at different alloy compositions, Dahn et al. estimated that 0.5 Li were reacting per carbon in the alloy. This corresponds to a capacity of 1116 mAh/g or about 1360 Ah/L. This is about twice the volumetric capacity of graphite. Studies of the volume expansion during the lithiation of Sn−Co−C alloys suggest to us that the lithiation of the amorphous carbon phase proceeds via an intercalation mechanism (see discussion in section 3.3).

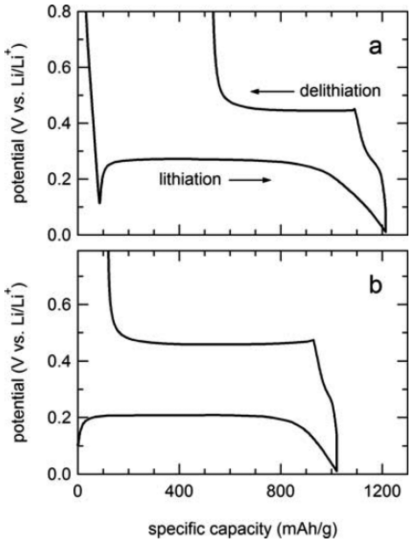


Figure 13. Potential versus specific capacity for the first galvanostatic cycle (1C rate) of electrodeposited aluminum films in a lithium half-cell. Average thickness of aluminum films was (a) 1.2 μm and (b) 6.2 μm. Reproduced with permission from ref 74. Copyright 2014 The Electrochemical Society.

Subramanian et al. and Purcell et al. studied the electrochemistry of pure and nearly pure amorphous carbon films prepared directly by sputter deposition.[30,79] The films were found to have a reversible capacity of about 800 mAh/g, in agreement with Dahn et al. The voltage curve of an amorphous $C_{0.86}Zn_{0.14}$ film is shown in Figure 14. It has an average voltage of about 0.75 V and is almost featureless and sloping, resembling a single-phase alloying reaction. Good cycling characteristics were demonstrated over 50 cycles.[30]

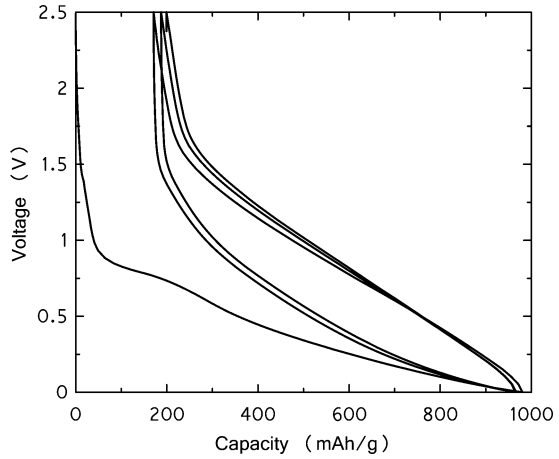


Figure 14. Voltage curve of an amorphous $C_{0.86}Zn_{0.14}$ thin film. Reproduced with permission from ref 30. Copyright 2014 The Electrochemical Society.

The lithiation of diamond films has also been investigated. Pure diamond, an electrical insulator, has been found to have almost no reversible capacity.[80] Doping diamond with boron to impart electrical conductivity results in only a slight improvement with reversible capacities reported in the range of 2−88 mAh/g.[81,82]

3.1.4.4. Silicon.

$$\textit{lithiation:}\quad x\text{-}Si \xrightarrow{Li} a\text{-}Li_ySi \xrightarrow{Li} a\text{-}Li_xSi \xrightarrow{Li} x\text{-}Li_{15}Si_4$$

$$\textit{delithiation:}\quad x\text{-}Li_{15}Si_4 \xrightarrow{-Li} a\text{-}Li_zSi \xrightarrow{-Li} a\text{-}Si$$

$$\textit{subsequent cycling:}\quad a\text{-}Si \xrightarrow{Li} a\text{-}Li_zSi \xrightarrow{Li} x\text{-}Li_{15}Si_4$$

Simplified from refs 83 and 84. "x" refers to a crystalline phase and "a" indicates an amorphous phase.

Silicon is one of the most important of the alloying elements because of its low cost and high energy density. Its lithiation mechanism is complex and depends on voltage limits and the initial Si structure and morphology. The electrochemistry and phase behavior during the cycling of bulk, nano, and thin film Si are discussed in detail in section 3.6.

3.1.4.5. Tin.

$$Sn \overset{Li}{\leftrightarrow} Li_2Sn_5 \overset{Li}{\leftrightarrow} LiSn \overset{Li}{\leftrightarrow} Li_7Sn_3 \overset{Li}{\leftrightarrow} Li_5Sn_2{}^* \overset{Li}{\leftrightarrow} Li_{13}Sn_5{}^* \overset{Li}{\leftrightarrow} Li_7Sn_2{}^* \overset{Li}{\leftrightarrow} Li_{17}Sn_4{}^*$$

"" represents disordered structures, refs 85, 86.*

The Li−Sn system, shown in Figure 15, comprises the Li_2Sn_5, LiSn, Li_7Sn_3, Li_5Sn_2, $Li_{13}Sn_5$, Li_7Sn_2, and $Li_{22}Sn_5$ binary phases.[40] It has recently been shown that the $Li_{22}Sn_5$ phase is more precisely represented by $Li_{17}Sn_4$.[86,87] Wang et al. showed that the lithiation of Sn at 400 °C proceeded according to the reported binary phase diagram.[33] However, at room temperature they found that Li_5Sn_2 was no longer formed. Figure 16 shows the Li−Sn voltage curve. In the region where $x > 2.5$ (>564 mAh/g), the voltage curve becomes sloped, indicative of the formation of

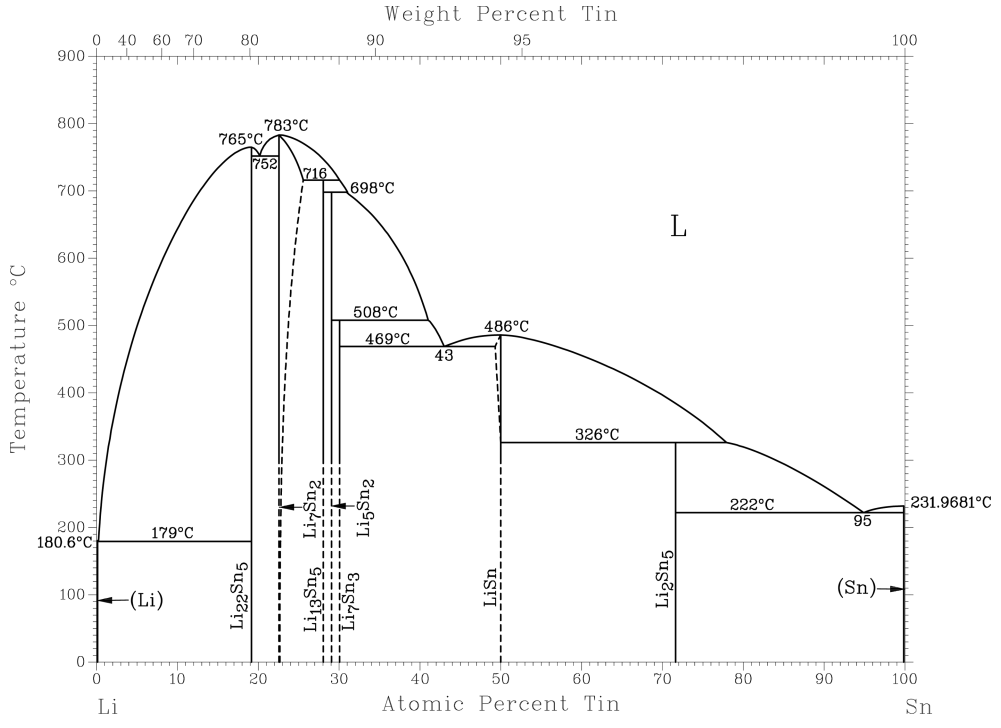


Figure 15. Li−Sn binary system. Reprinted with permission from ref 40. All rights reserved, www.asminternational.org. Copyright 1996 ASM International.

dx.doi.org/10.1021/cr500207g | *Chem. Rev.* 2014, 114, 11444−11502

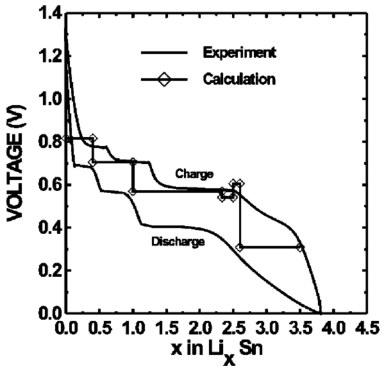


Figure 16. An experimentally measured Li−Sn voltage curve and voltage curve from ab initio calculations. Reprinted with permission from ref 85. Copyright 1998 American Physical Society.

single-phase regions and the inability of the system to nucleate crystalline phases at room temperature.[19]

Courtney et al. suggested that when the lithium content is above $x > 2.5$ in Li_xSn, none of the structures formed in the binary phase diagram are formed during the room temperature lithiation of Sn.[85] Instead, phases resembling the bulk phases, but including some disorder, were observed by XRD.[88] This is consistent with earlier in situ XRD studies during the lithiation of SnO by Courney et al., in which the phases Sn, Li_2Sn_5, and LiSn were identified as being sequentially formed, while at higher levels of lithiation only broad XRD peaks were present and the more lithium-rich phases could not be distinguished.[89] In further contrast to the equilibrium Li−Sn system, the highest lithiation level achievable at room temperature has been reported to be 3.4−3.8 in Li_xSn.[85,90] However, XRD measurements show that the short-range ordering of the highest lithiated phase is consistent with that of "$Li_{22}Sn_5$".[88] Because the Li_xSn phases with $x > 2.5$ are the highest melting phases in the Li−Sn system, low atom mobility in these high melting phases might explain why these are not formed, while faster atom mobility allows the low melting phases to be formed during room temperature lithiation (see section 3.2).

Mössbauer spectroscopy is a useful probe in the study of Sn containing anodes, and the Mössbauer parameters of the Li−Sn phases have been reported in a number of studies.[90−92] An in situ Mössbauer study by Courtney et al. found that Sn, Li_2Sn_5, and LiSn were unambiguously formed during the lithiation of tin containing glasses. The Mössbauer spectra of higher lithiated Sn-phases did not correspond as well with the known spectra of bulk Li−Sn phases, excepting that at full lithiation the spectrum of "$Li_{22}Sn_5$" was clearly identified. These results are consistent with their earlier in situ XRD studies.[88,93]

3.1.4.6. Lead.

$$Pb \overset{Li}{\leftrightarrow} Li_{1.0}Pb^* \overset{Li}{\leftrightarrow} Li_{1.5}Pb^* \overset{Li}{\leftrightarrow} Li_{2.5}Pb^* \overset{Li}{\leftrightarrow} Li_{3.0}Pb^* \overset{Li}{\leftrightarrow} Li_{3.5}Pb^* \overset{Li}{\leftrightarrow} Li_{4.5}Pb^*$$

**Determined by coulometric titration.*[28]

Because lead is toxic, one might argue that it should not be included in a discussion of electrode materials for commercial Li-ion batteries. However, lead acid batteries are currently used in the majority of the >1 billion automobiles on the planet. This is made possible by the implementation of efficient recovery/recycling programs.[94] Although the movement toward nontoxic systems is desirable, given the massive precedent for the use of Pb in batteries, we have included it in this discussion.

The binary Li−Pb phases present in the Li−Pb system[40] are LiPb, Li_5Pb_2, Li_3Pb, $Li_{10}Pb_3$, and Li_4Pb (which is more accurately described as $Li_{17}Pb_4$).[86] Few studies of the lithiation of Pb have been reported.[28,46,95] This may be due to the relatively low specific capacity of Pb as compared to other active elements (550 mAh/g for $Li_{17}Pb_4$). Nevertheless, Pb's low average voltage (~380 mV)[28] and high volumetric capacity (1937 Ah/L for $Li_{17}Pb_4$) are attractive. As a result, Pb has an even greater impact on raising cell energy than Sn, as shown in Table 3.

No published Pb voltage curve could be found, apart from the first lithiation half-cycle.[28,46] The voltage plateaus from coulometric titration are roughly consistent with the compositions of the equilibrium Li−Pb phases.[28] Figure 17 shows the

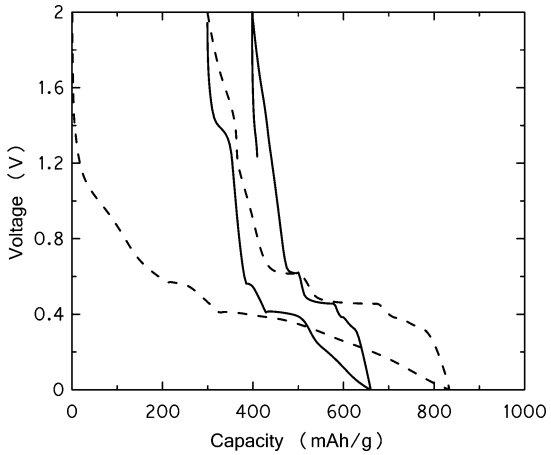


Figure 17. Pb versus Li voltage curve. The first and second cycles are shown with dashes and lines, respectively. Data for this curve are from ref 23.

voltage curve of Pb, which was generated from the data collected for ref 23. The voltage curve is similar to that of Sn, with plateaus occurring at low levels of lithiation and a sloping region present at high lithiation levels, where more complex and high melting phases occur. This is suggestive that the high lithium content phases are not formed at room temperature, in a fashion similar to that of the Li−Sn system (see also section 3.2). A detailed XRD study of the lithiation of Pb is needed to more fully understand this system.

3.1.4.7. Antimony.

$$\textit{lithiation:}\quad Sb \overset{Li}{\rightarrow} Li_2Sb \overset{Li}{\rightarrow} Li_3Sb$$

$$\textit{delithiation:}\quad Li_3Sb \overset{-Li}{\longrightarrow} Sb$$

From refs 96, 97.

The voltage curve during the lithiation of Sb at room temperature has two plateaus at 0.956 and 0.948 V corresponding to the formation of Li_2Sb and the high pressure cubic ($Fm\bar{3}m$) polymorph of Li_3Sb, respectively.[33,96,97] During delithiation, Li_3Sb converts directly to Sb, without the formation of the Li_2Sb intermediate phase.[96,97] This may be attributed to the high melting point and complexity of the Li_2Sb phase (18 atoms per unit cell), as compared to the relatively simple crystal structure of the Li_3Sb phase (8 atoms per unit cell), as discussed in section 3.2. Ex situ XRD measurements of fully lithiated sputter deposited 4 μm Sb films by Baggetto et al. contained diffraction peaks from the ambient pressure hexagonal phase ($P6_3/mmc$) of Li_3Sb in addition to the high pressure cubic

dx.doi.org/10.1021/cr500207g | Chem. Rev. 2014, 114, 11444−11502

($Fm\bar{3}m$) polymorph.[97] It was suggested that the cubic phase may convert spontaneously to the hexagonal phase at room temperature.

Huggins et al. suggested that the potentials of the Sb voltage plateaus "are too high (over 0.8 V vs pure lithium at room temperature) to be useful as negative electrode materials in most lithium-based cells."[33] Nevertheless, a large amount of research has been done, and continues, on Sb-based alloys.

3.1.4.8. Bismuth.

$$Bi \overset{Li}{\leftrightarrow} LiBi \overset{Li}{\leftrightarrow} Li_3Bi$$

References 33, 98.

The Bi–Li system contains two binary phases: LiBi and Li_3Bi.[40] Lithiation of Bi at room temperature has been shown to follow the equilibrium phase diagram by coulometric titration and in situ XRD.[33,98] Few studies have been reported for bismuth-based alloys, perhaps due to its high voltage vs Li and relatively high cost. However, even though Bi has a lower average voltage than Sb, and results in a higher cell energy according to Table 3, there are many more publications on Sb-based alloys than Bi-based alloys.

3.2. Selective Formation of Li–M Equilibrium Phases

The different lithiation mechanisms described in the previous sections are suggestive of a basic trend regarding when phases present in the equilibrium diagram are not formed during room temperature lithiation. That is, when a complex Li–M phase is present in the equilibrium phase diagram and has a high melting point, it is not formed during lithiation at room temperature. Indeed for systems with adequate crystallographic information (M = Bi, Sn, Al, Sb, Si, Cd, Ga, Ge), when the total number of atoms in the Li–M unit cell is greater than 17 and the melting point of the Li–M phase exceeds 550 °C, the Li–M equilibrium phase is not formed during room temperature lithiation. Li_2Sb is an intermediate example, because while it meets the above criteria (Li_2Sb has 18 atoms in its unit cell and melts at 825 °C),[40] it does form during lithiation, but not during delithiation, as discussed in section 3.1.4.7.

Phases with high melting points generally have low atom mobility. This presumably does not allow the rearrangements of atoms to form complex structures at room temperature. It should be noted that the inverse of this rule is not necessarily true: that is, some phases with low melting points or low complexity still may not form during lithiation.

3.3. Volume Expansion during Lithiation

The lithiation of the active elements generally results in a large volume expansion of the host, which can reach up to 280% in the case of Si.[83] Only a simple overview of volume expansion and its effects is presented here to motivate the discussion of practical electrode design. The effects of alloy volume expansion and theoretical modeling of stress and strain during lithiation have recently been reviewed in detail.[13] The consequences of volume expansion are detrimental on all levels. At the cell level, volume expansion can cause current collector distortion, crushing of the separator, and cell bulging. At the electrode level, repeated volume expansions and contractions during the cycling of composite electrode coatings containing active alloy powders can cause the active materials to lose electrical contact, resulting in cell fade.[46,99,100] At the particle level, the volume expansion of alloys is thought to cause disruption in the SEI layer, resulting in cell fade.[101−103] At the subparticle level, the internal stresses that result from alloy expansion can cause alloy particles to fracture, leading to loss of electrical contact and cell fade.[46,100,101,104]

By plotting the volume per host atom versus the number of Li inserted per host atom, Obrovac et al. showed that the lithiation of the active elements generally follows Vegard's law.[23] Such a plot is shown in Figure 18. This trend is also true of alloys of alkali

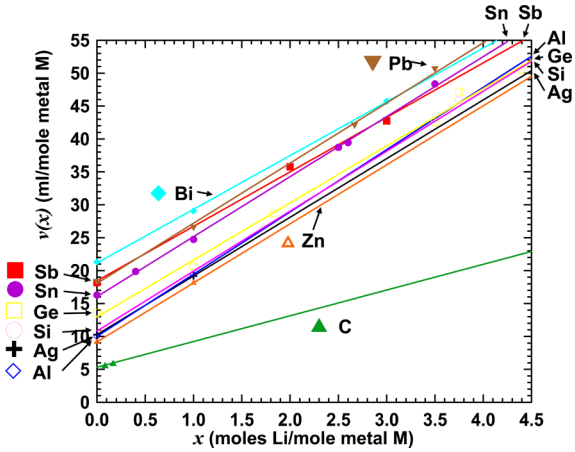


Figure 18. Volume of lithiated alloy per mole of host metal M, $v(x)$, plotted as a function of the lithium content, x. Reproduced with permission from ref 23. Copyright 2007 The Electrochemical Society.

and alkaline earth metals.[105] The slope of the lines plotted in Figure 18 corresponds to the molar volume that lithium occupies in the alloy.[23] Obrovac et al. found that this quantity is nearly the same for all Li–M binary alloys (except a-C, as discussed below) and is about 8.9 mL/mol inserted Li (or 14.8 Å^3/Li). We refer to this as the "standard lithiation model" when calculating volume expansion of alloys in this Review. As a consequence of this observation, Obrovac et al. argued that if volume expansion limits cycling performance, then the energy density depends little on the active element used.[23] This is illustrated in Figure 19, which

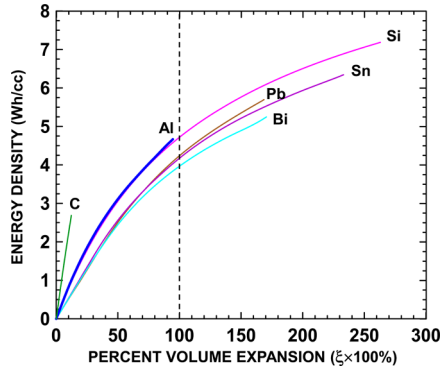


Figure 19. Energy expansion curves (vs a 3.75 V cathode) for various active metal elements calculated from their voltage curves. Reproduced with permission from ref 23. Copyright 2007 The Electrochemical Society.

plots the "energy density" of the active elements (versus a 3.75 V cathode) as a function of the volume expansion of different anode materials. At 100% volume expansion, for instance, the "energy densities" of all of the active elements are similar. As mentioned in section 2, such single electrode "energy densities" are not equivalent to those calculated for a full cell, in which the anode voltage is strongly weighted over its volumetric capacity.

dx.doi.org/10.1021/cr500207g | Chem. Rev. 2014, 114, 11444−11502

However, this figure still represents a valid comparison, because the average voltages of Si, Sn, Al, and Pb are all similar. Therefore, full cells with these elements as anodes with capacities limited to 100% volume expansion will have similar energies. A more accurate treatment of the relation between energy density and volume expansion is discussed in section 3.7.2.1 with respect to active/inactive alloys.

The volume expansion of alloys by 8.9 mL/mol inserted Li proposed by Obrovac et al. has been confirmed for Si and Sn by in situ AFM and optical measurements of alloy expansion during lithiation.[31,100,106] However, Tian et al. found that lithium only occupies 3.4 mL/mol (5.7 Å/Li) in the amorphous carbon phase in sputtered Sn−Co−C alloys.[31] This is slightly less than the volume Li occupies in fully lithiated graphite (4.2 mL/mol, 7.0 Å/Li) and is suggestive to the present authors that Li inserts into a-C with an intercalation mechanism (such as Li insertion in hard carbon) as opposed to an alloying mechanism. In the case of Si, volume expansion has been shown to be nonisotropic. Figure 20

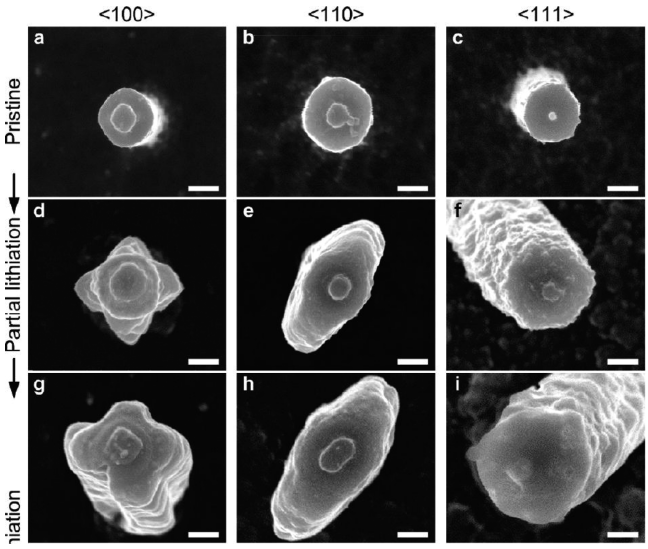


Figure 20. Anisotropic lateral expansion of crystalline Si nanopillars with three different axial orientations (⟨100⟩, ⟨110⟩, and ⟨111⟩) upon lithiation. The top row shows pristine pillars, the second row shows partially lithiated pillars held at 120 mV vs Li/Li^+, and the third row shows fully lithiated pillars held at 10 mV vs Li/Li^+. Scale bars are 200 nm. Reprinted with permission from ref 107. Copyright 2011 American Chemical Society.

shows SEM images of lithiated Si nanopillars with different crystal orientations. Preferential volume expansion occurs along the ⟨110⟩ direction, due to enhanced Li diffusion in this direction.[107]

The effect of volume changes on particle morphology has been illustrated in the case of the lithiation/delithiation of Sn particles.[108,109] Figure 21 shows the morphologies of Sn particles that have been delithiated from different initial lithium concentrations. Delithiation results in void formation, forming bicontinuous porous structures. The morphology of these structures is dependent on temperature, rate, and particle size. For instance, particles remain intact with no bicontinuous structure formation when the particle size is 2−3× the ligament size, with the ligament diameter being of the order of 100 nm at 10C to C-rate and about 200 nm at C/2 rate.[109] In thin films of active materials, initial lithiation causes the film to expand under compression. During delithiation, tensile stress causes the film to crack, as shown in Figure 22, forming islands of active material that are bonded to the substrate at a single point.[110−113] During the subsequent cycling reversible behavior is observed, with no additional crack formation. For further discussion of the effects of volume expansion and the theoretical modeling of volume expansion processes, readers are directed to the excellent recent review by McDowell et al.[13]

3.4. Effect of Two-Phase Regions on Cycle Life

During alloy lithiation or delithiation, two-phase regions may be encountered. This will result in a voltage plateau and a reaction front being created in the alloy along which two phases coexist with significantly different molar volumes. In the case of Si, this reaction front has been directly observed by TEM.[114,115] The phase boundary was found to be very sharp and on the order of about 1 nm.[115] Stresses along the reaction of Si and the resulting plastic deformation and fracturing have also been described by theoretical models.[13,116] Both experiment and theory are indicative that two-phase boundaries cause additional particle damage due to inhomogeneous volume change, as compared to homogeneous volume change during lithiation in a single-phase region.[13,84,89,117−121] For example, this effect has been convincingly observed in Sn-oxide glasses in which single-phase and two-phase behavior can be observed in the same material.[89,119] Initially such materials cycle with a single-phase lithiation insertion into n-Sn regions. After many cycles, the Sn phase aggregates, leading to a two-phase lithiation mechanism, which inevitably leads to capacity fade.

Because fade and two-phase regions are often coincident, it is generally thought that two-phase regions should be avoided during cycling. However, there are many examples in which excellent cycling has been obtained in materials that cycle over two-phase regions. Li−Pb alloys have been reported to cycle hundreds and even thousands of times over multiple phase transitions using conductive binders.[122] Sn has been shown to reaggregate in such binders.[123] Perhaps this reaggregation mechanism may explain the ability of soft metals to cycle well in conductive binders over two-phase regions. However, brittle materials have been shown to cycle well over two-phase regions as well. For instance, Bryngelsson et al. have shown that Sb/Sb_2O_3 can be cycled over a flat 1 V plateau with no capacity fade for 50 cycles.[124] We suggest that cycling such at high voltages may avoid SEI growth that is associated with insulating particles from each other, causing fade.[102,125] Unfortunately, cycling at such high voltages also drastically reduces energy density, as discussed in section 2.

3.5. Ability of DFT To Predict Alloy Voltages

The voltage versus Li metal at which an electrochemically active element alloys with Li can be calculated from the definition of the chemical potential:

$$V = \frac{\mu_{Li}}{q} = -\frac{\Delta G}{e\Delta N} = -\frac{\Delta E + P\Delta V - T\Delta S}{e\Delta N} \approx -\frac{\Delta E}{e\Delta N} \quad (18)$$

where V, μ, q, e, G, N, and E are the voltage, chemical potential, charge, absolute electron charge, Gibbs free energy, Li number, and internal energy, respectively. The approximation where the entropic ($T\Delta S$) and enthalpic ($P\Delta V$) contributions are neglected is justified on the basis of the fact that they are typically 2 and 5 orders of magnitude smaller than the change in internal energy, respectively.[126] Computational schemes that calculate the internal energy (or total energy) of structures can

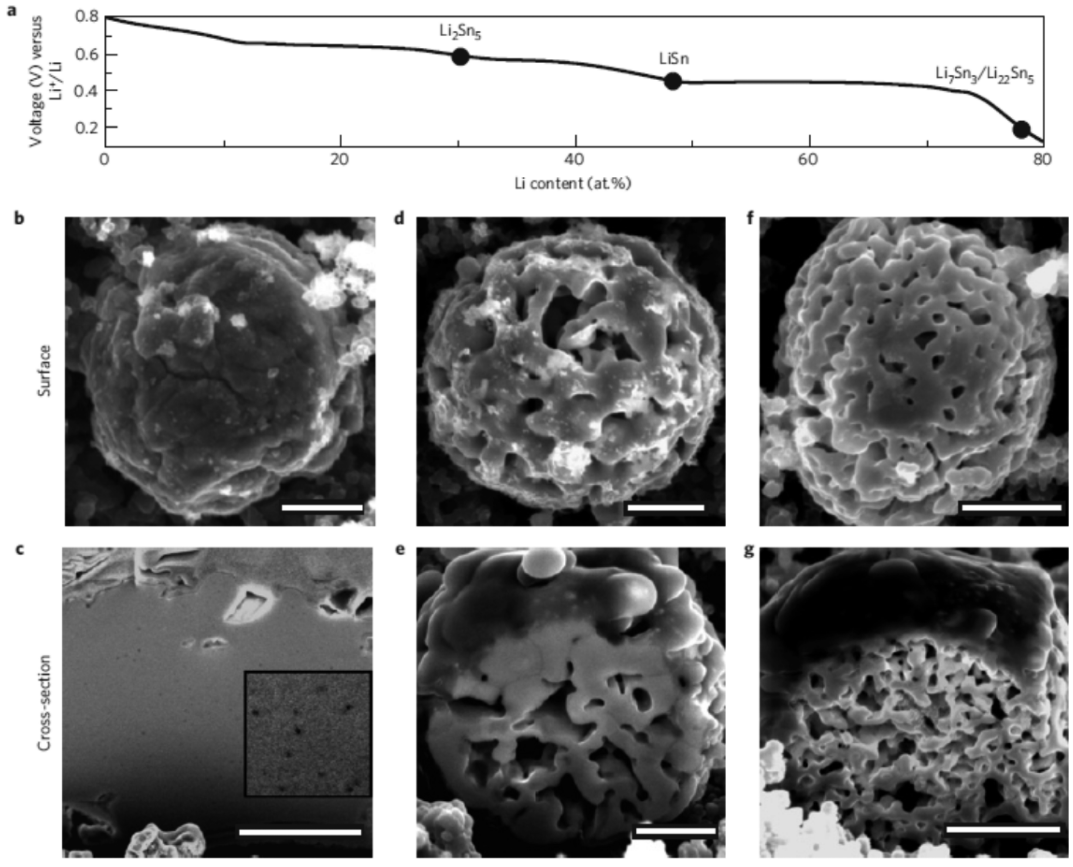


Figure 21. Potentiostatic dealloying (1 V versus LiC═Li) results of Sn particle morphologies as a function of Li composition obtained by a single alloying/dealloying cycle in 1 M $LiPF_6$ in ethylene carbonate/diethylcarbonate, 1:1 v/v at room temperature. (a) Voltage versus Li content for alloying Li into ∼2 μm diameter Sn particles at a fixed current of −49.7 mA/g_{Sn}. The voltages define the composition of the particles. (b−g) The first row of SEM images corresponds to particle surfaces and the second row to focused ion-beam milled cross sections of the particles. (b,c) $Li_{0.30}Sn_{0.70}$; the surface is roughened with void nodules, and the particle interior contains ∼10 nm-diameter voids (c, inset, size of image, 200 nm) that may have formed through a Kirkendall process. These voids are absent in virgin Sn particles. (d,e) $Li_{0.48}Sn_{0.52}$; collapsed bicontinuous morphology yielding a hollow core−shell-like structure. (f,g) $Li_{0.77}Sn_{0.23}$; bicontinuous morphology with a ligament size of 50−100 nm. Scale bars, 500 nm. Reprinted with permission from ref 109. Copyright 2013 Macmillan Publishers Ltd.: Nature Materials.

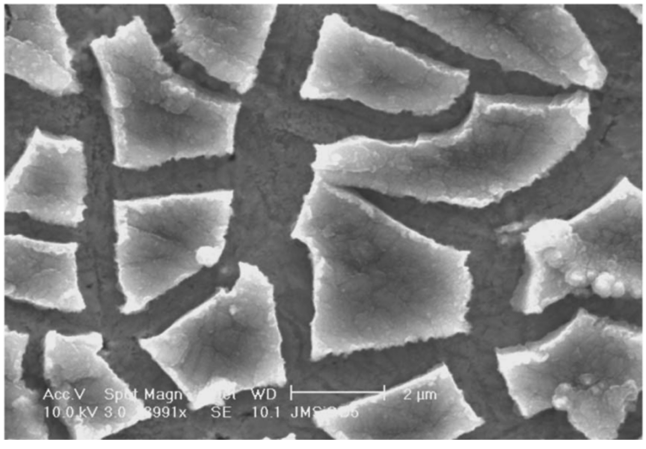


Figure 22. SEM image of a delithiated 250 nm Si thin film cycled after 30 cycles at C/2.5. Reproduced with permission from ref 112. Copyright 2006 The Electrochemical Society.

therefore be used for the calculation of voltages. Specifically, the potential versus Li metal of the reaction:

$$Li_xX + yLi \rightarrow Li_{x+y}X \quad (19)$$

is obtained using eq 18 as

$$V = -\frac{E(Li_{x+y}X) - E(Li_xX) - yE(Li)}{y} \quad (20)$$

The elements that alloy with Li at anode-relevant potentials are typically crystalline and have phase diagrams that include crystalline binary phases containing Li, as discussed in section 3.1. Li metal is also crystalline at room temperature with a body-centered cubic structure. The most widespread approach for reliably calculating the total energy of crystal structures is density functional theory (DFT), which is based on self-consistently solving the one-electron Kohn−Sham equations[127] using plane wave basis sets to represent the electron wave functions. The details of DFT are beyond the scope of this Review, and, furthermore, DFT calculations can be performed using reliable commercial (VASP,[128] CASTEP[129]) as well as open source (ABINIT,[130] QUANTUM ESPRESSO[131]) packages, which enjoy widespread use.

Li-based intermetallics are Zintl phases and have electronic structures that can be described as a mix of metallic and covalent bonds where the Li atoms are not completely ionized.[132,133] During lithiation, the yLi in eq 19 leaves metallic Li (completely delocalized electrons) and enters an intermetallic alloy (somewhat delocalized electrons). The DFT calculation errors stemming from approximations to electron self-interaction will

dx.doi.org/10.1021/cr500207g | Chem. Rev. 2014, 114, 11444−11502

be similar and mainly cancel. This is an important detail, as this is not the case when considering typical cathode materials where the Li atoms become completely ionized and the electron goes from a delocalized to a highly localized state, requiring further corrections for accurate voltage predictions.[126,134] Basic DFT is therefore particularly well suited for the calculation of alloy anode lithiation voltages. The results are not extremely dependent on the treatment of the exchange-correlation energy (local density approximation (LDA)[135] or the general gradient approximation (GGA)[136]) or on the choice of pseudopotential (norm conserving,[137] ultrasoft,[138] or projector-augmented wave[139]).[140]

The first report of DFT calculations for an alloy anode was for the Li−Sn system.[85] Using the crystalline structures of the Li−Sn phase diagram in a series of stepwise two phase reactions, predicted voltage curves were found to be in good agreement with experiment, as shown in Figure 16.[85] In contrast, Si presents a more interesting case as it forms the binary crystalline phases of the Li−Si phase diagram when lithiated at high temperature (415 °C),[141] but is electrochemically amorphized during lithiation at room temperature.[142] The first DFT studies of Si as an anode material showed agreement of two-phase reaction voltages with high temperature experimental results[140] as well agreement with room temperature lithiation when using disordered Li−Si structures as shown in Figure 23.[143,144] Because of the feature-rich behavior of Si during electrochemical lithiation and delithiation, as well as the high level of interest from the experimental community, numerous DFT-based studies followed, investigating both ordered and disordered structures, diffusion paths, and surface kinetics. Reference 145 presents a review of first principles studies of Si in the context of Li-ion batteries.

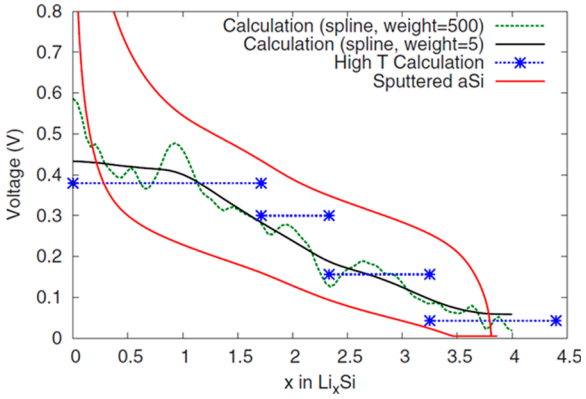


Figure 23. Voltage profiles obtained with DFT calculations as compared to experiment for crystalline Li−Si phases (blue *),[140] and disordered Si (green and black curves),[143] showing the ability of DFT to accurately predict equilibrium voltages. Reproduced with permission from ref 143. Copyright 2009 The Electrochemical Society.

The voltage obtained from DFT calculations can be considered an equilibrium voltage and should lie between the lithiation and delithiation voltages obtained experimentally. All known alloy voltage profiles display significant hysteresis and are distinct from voltage curves obtained from intercalation materials such as graphite. While the hysteresis is partially ohmic in nature, it remains to a large degree even at rates as low as C/1000.[144] A number of explanations have been proposed to account for the voltage hysteresis based on thermodynamic considerations,[146] bond breaking,[144] nucleation energy,[147] kinetic resistance,[148] and stress-potential coupling.[149] However, a definitive answer to the origin of voltage hysteresis remains to be stated. The voltages obtained by DFT can therefore be considered an average voltage for a given state of charge, devoid of any kinetic information.

The voltages listed in Table 4 were obtained from the Materials Project, which is based on DFT calculations employing GGA and the VASP library of PAW pseudopotentials.[150] The agreement between experiment and DFT is good, although DFT voltages are found to be slightly lower on average (~0.1 V). Figure 23 shows results consistent with Table 4 indicating that the gap between DFT and experimental values stems from experimental hysteresis. The emergence of large scale open databases based on DFT calculations such as the Materials Project[150] or the AFLOWLIB.ORG Consortium[151] can be expected to help guide the early selection and screening of alloy-based anode materials for Li-ion batteries. Indeed, the information that can be extracted from DFT calculations is sufficient to approximate the gravimetric and volumetric capacities as well as the attainable volumetric and gravimetric energies when implemented in a full cell.[23] However, these studies will need to remain to a certain extent guided by experiment to avoid identifying phases that are experimentally inactive as potential candidates.[152]

Table 4. Fully Lithiated Phase and Average Voltage of Various Elements As Determined by Experiment (See Table 3) and by DFT Results Obtained from the Materials Project[150a]

	experiment		DFT	
element	fully lithiated phase	average voltage (V)	fully lithiated phase	average voltage (V)
Mg	$Li_{1.95}Mg$	0.0325		
Ag	γ_3-$Li_{2.7}Ag$	0.175	LiAg	0.42
Zn	LiZn	0.31	LiZn	0.42
Al	LiAl	0.38	Li_9Al_4	0.23
Si	$Li_{15}Si_4$	0.4	$Li_{21}Si_5$	0.27
Sn	$Li_{4.4}Sn$	0.504	$Si_{17}Sn_4$	0.43
Pb	$Li_{4.5}Pb$	0.423	$Li_{17}Pb_4$	0.35
Sb	Li_3Sb	0.948	Si_3Sb	0.84
Bi	Li_3Bi	0.822	Li_3Bi	0.71

[a]According to DFT calculations, Li and Mg do not form a stable phase.

3.6. The Electrochemistry of Silicon

The behavior of Si upon lithiation in a Li-ion cell at room temperature is feature-rich and depends on many parameters including particle size, morphology, and rate. Electrochemical studies in the late 1970s of the Li−Si system at temperatures near 400 °C showed the formation of binary crystalline Li−Si phases, which closely matched the Li−Si phase diagram.[141,153] In 1995, Wilson and Dahn studied Si-containing electrodes at room temperature in half cells, in the form of both nanodispersed Si and bulk Si powder.[154] The voltage curves obtained differed significantly from the high temperature results. In this section, the electrochemistry of Si will be discussed in detail. To highlight the impact of particle size and morphology, the discussion will be sectioned in terms of the electrochemistry of bulk Si, thin film Si, and nano Si (n-Si). While many questions remain, the volume of work on this topic has already warranted review articles.[13]

3.6.1. The Electrochemistry of Bulk Silicon. Limthongkul et al. were the first to identify the amorphization of crystalline Si upon lithiation.[142] Obrovac and Christensen identified the

existence of a new Li−Si phase, $Li_{15}Si_4$, at full lithiation based on XRD studies and voltage curve features.[83] Several in situ studies have contributed to the understanding of the structural changes occurring in bulk Si during lithiation and delithiation at room temperature. These include: in situ XRD,[84,155] in situ Mössbauer,[156] in situ NMR,[155] in situ acoustic emission (AE),[157] in situ stress measurement,[115] and in situ TEM.[158,159]

3.6.1.1. Lithiation of Crystalline Silicon. Figure 24 shows the voltage profile of bulk polycrystalline Si powder (denoted here as

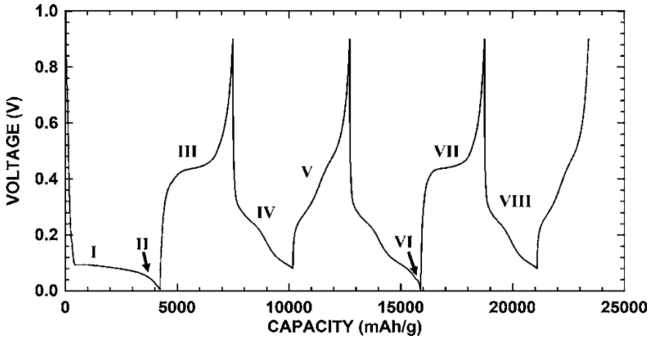


Figure 24. Voltage curve of bulk Si powder. Reproduced with permission from ref 161. Copyright 2007 The Electrochemical Society.

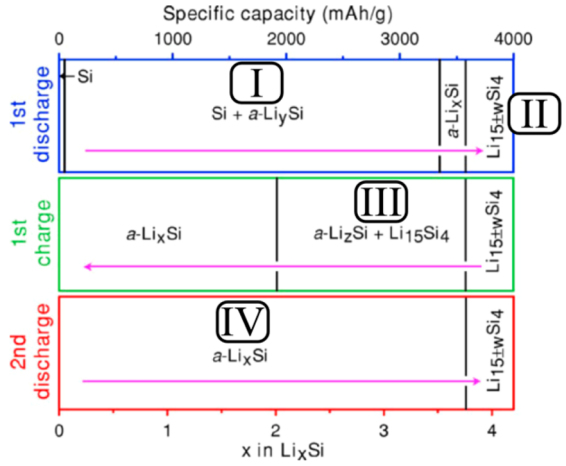


Figure 25. Schematic phase diagram as a function of lithiation. Roman numerals correspond to those in Figure 24. Adapted with permission from ref 84. Copyright 2007 The Electrochemical Society.

x-Si). Figure 25 shows a schematic phase diagram as a function of lithiation, which has been labeled so that regions in the phase diagram may be identified with regions in the voltage curve shown in Figure 24. The initial potential near 1 V is consistent with the calculated potential of surface lithiation.[160] The potential quickly drops to a low, gently sloping plateau, which extends for most of the Si capacity. This plateau corresponds to a two-phase reaction between x-Si and a heavily lithiated amorphous Li_ySi phase and is marked as "I" in Figures 24 and 25. Obrovac and Krause determined the potential at which x-Si is lithiated to be precisely 170 mV.[161] Figure 26 shows a TEM image in which the front of the a-Li_ySi phase can be seen consuming the Si core.[159] Similarly narrow fronts are found during lithiation of Si wafers[115] and nanowires.[158] Once this front has reached the core, the particle consists of a-Li_xSi where many of the Si atoms are paired as dimers and some Si atoms are surrounded by Li atoms.[144,155,160] Further lithiation results in the formation of crystalline $Li_{15}Si_4$.[83] The electrochemical feature of $Li_{15}Si_4$ formation is an extremely small voltage plateau during lithiation found near 50 mV vs Li and is indicated by "II" in Figures 24 and 25.[83]

The $Li_{15}Si_4$ phase was first observed by Obrovac and Christensen.[83] It is metastable and has only been observed via electrochemical lithiation of Si at or near room temperature. In the $Li_{15}Si_4$ structure, all Si atoms are isolated and have equivalent crystallographic sites. The sudden crystallization of $Li_{15}Si_4$ during lithiation is not a feature typically seen in alloy anodes, as crystalline phases are usually attained through two-phase reactions. Crystalline Li−Si phases with lower Li content than $Li_{15}Si_4$ contain Si arrangements ranging from Si rings and stars in $Li_{12}Si_7$ to Si dimers in $L_{13}Si_4$.[133] Because $Li_{15}Si_4$ is the phase with the lowest Li content having completely isolated Si atoms, it appears that during lithiation the lower Li content crystalline phases are unattainable due to energy barriers to Si rearrangement, even though they are lower-energy configurations. Once the Si atoms have become isolated, the similarity in structure of the a-Li_ySi and $Li_{15}Si_4$, and the high mobility of Li atoms, allows the system to attain a lower energy state at room temperature.[143,144,160,162] While Obrovac and Christensen were able to identify stoichiometric $Li_{15}Si_4$ using Rietveld refinement, Key et al.[155] and Li et al.[84] found by in situ NMR and XRD, respectively, that the $Li_{15}Si_4$ phase appears to be able to accommodate a small range of Li concentrations.

The formation of $Li_{15}Si_4$ at full Si lithiation corresponds to a gravimetric capacity of 3579 mAh/g. Many papers have stated $Li_{21}Si_5$ (4008 mAh/g) or $Li_{22}Si_5$ (4199 mAh/g) as the fully lithiated phase of Si, likely due to the assumption that Si lithiation would reach the most Li-rich phase of the Li−Si phase diagram. While many papers show initial lithiation levels that go beyond 3579 mAh/g, for room temperature studies one can likely attribute this extra capacity to surface reactions stemming from either SEI formation or lithiation of surface oxides. XRD and TEM results have confirmed the final lithiation state as $Li_{15}Si_4$ for bulk Si,[83,84] Si thin films,[163] and nano Si.[159]

Upon heating, electrochemically lithiated Si will eventually form the phases found in the equilibrium phase diagram. Crystallization events have been found to occur in the 150−350 °C temperature range.[164,165] Activation energies for crystallizations requiring a reworking of the Si framework (~300 kJ/mol) were roughly twice as large as those requiring mainly Li rearrangements (~150 kJ/mol).[165]

3.6.1.2. Delithiation of $Li_{15}Si_4$. Figures 24 and 25 show that the electrochemical feature of $Li_{15}Si_4$ delithiation is a large plateau near 0.45 V, identified by "III". The plateau indicates that delithiation is occurring by means of a two-phase reaction where the crystalline $Li_{15}Si_4$ is converted to a-Li_zSi, where z is approximately 2.[84] Further delithiation yields a rising voltage indicative of a solid solution reaction where the a-Li_zSi phase is uniformly delithiated until amorphous Si is obtained. Once bulk Si has been fully lithiated and delithiated, the resulting amorphous Si is essentially independent of the structure of the starting bulk Si. Indeed, whether one has started with crystalline Si, amorphous Si, or a Li−Si phase, the amorphous Si resulting from a single lithiation and complete delithiation will be essentially the same.[161]

3.6.1.3. Lithiation of Amorphous Silicon and Delithiation of Amorphous Li_xSi. The lithiation of bulk a-Si follows the voltage curve marked as region "IV" in Figure 24, also corresponding to region "IV" in Figure 25. The voltage curve of bulk a-Si lithiation

dx.doi.org/10.1021/cr500207g | Chem. Rev. 2014, 114, 11444−11502

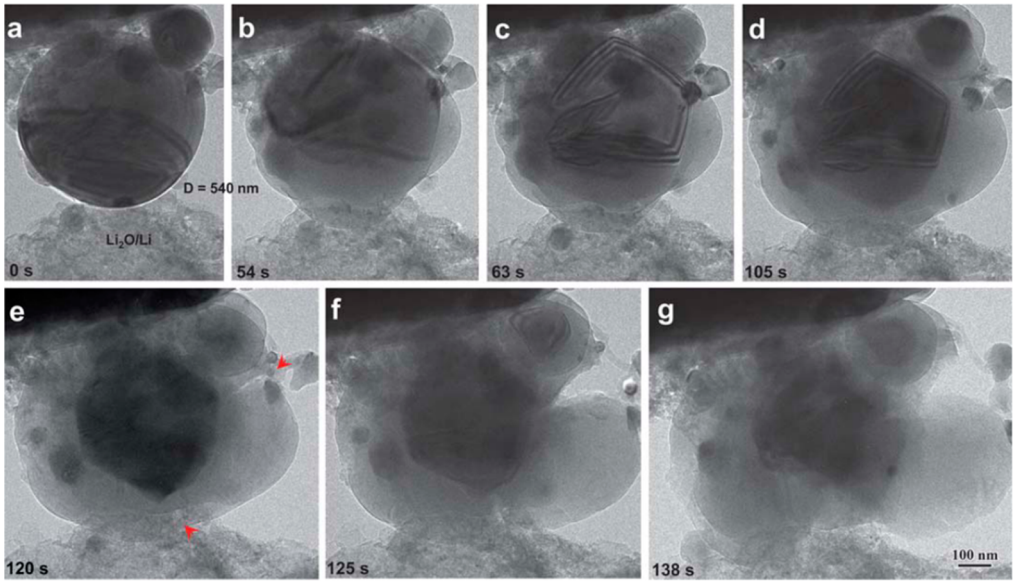


Figure 26. Lithiation induced cracking and fracture of a big Si particle with a diameter of 540 nm. (a) Pristine Si particle in contact with the Li_2O/Li electrode. (b–d) Steady lithiation stage without cracking. The anisotropic lithiation resulted in a faceted Si core and some bumps in the Li_xSi shell with a light contrast. (e–g) Crack formation and fracture. When the Li_xSi shell is 150–200 nm thick, cracks were initiated from the particle surface (e), then developed (f), and finally broke the particle into pieces (g). Reproduced with permission from ref 159. Copyright 2011 The Royal Society of Chemistry.

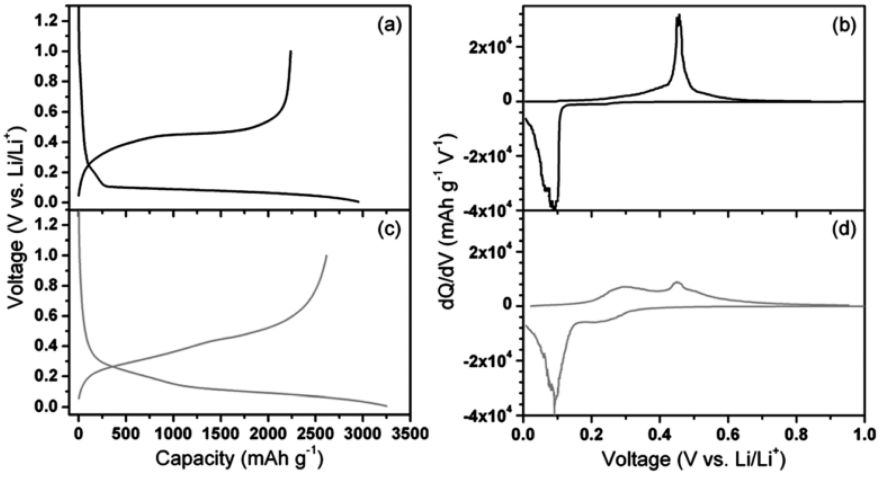


Figure 27. Voltage and differential capacity profiles for the first cycle of (a and b) as-received 1–5 mm Si or (c and d) ball milled 1–5 mm Si powders, at a current density of 480 mA/g (~C/7). Reproduced with permission from ref 167. Copyright 2013 The Royal Society of Chemistry.

is gently sloping with two quasi-plateaus showing up as two characteristic "humps" in the differential capacity. A similar voltage curve is obtained if one starts with "fresh" amorphous Si obtained either by sputtering or by ball milling. In situ Mössbauer studies of Si with a Sn probe[156] as well as computational simulations of Si lithiation[144] indicate that the higher voltage quasi-plateau is characteristic of Li entering an atomic environment dominated by Si neighbors or equivalently of Si atoms being mainly bonded to other Si atoms. The lower quasi-plateau corresponds to Li entering environments dominated by Li atoms or equivalently when Si atoms have mainly Li neighbors. The overall sloping voltage is characteristic of a solid-solution type reaction, indicating that lithiation occurs essentially homogeneously throughout the particle. If amorphous Si is lithiated such that its potential reaches ~70 mV or lower, the $Li_{15}Si_4$ phase will form (as evidenced by the subsequent "VII" plateau), and delithiation will be identical to the previously described $Li_{15}Si_4$ delithiation.[83,161] This is shown in Figure 24, "VI". However, as shown in Figure 24, "IV", if the lithiation of Si is interrupted before ~70 mV is reached, then the formation of $Li_{15}Si_4$ is avoided and amorphous Li_xSi can be delithiated.[83,161] The delithiation of a-Li_xSi takes place via the reverse solid-solution reaction as the lithiation of a-Si.[83,156,161] This is evidenced by the sloping delithiation voltage profile with two plateaus marked as "V" in Figure 24.

McDowell et al. have shown that a lithiation front is still observed when one starts with fresh a-Si, and that a voltage plateau is obtained, although it is more sloping than that of crystalline Si.[166] The amorphous Si resulting from subsequent delithiation was also found to have a 25% greater volume, likely indicative of a more open a-Si with a greater number of dangling bonds.[166] The flatness of the voltage plateau during the first lithiation is therefore a measure of the degree to which a two-phase reaction is taking place and of the energy required for Li to penetrate the Si structure. A good example of this has been recently published, comparing crystalline Si and Si that had been

ball milled to obtain micrometric Si particles that had ~10 nm nanocrystalline domains.[167] Figure 27 shows that the initial lithiation voltage of nanocrystalline Si is significantly more sloped than that of crystalline Si, indicating a diminished two-phase front. Also of note is the suppression of the $Li_{15}Si_4$ phase for the nanocrystalline Si as evidenced by the lack of a significant plateau at 0.45 V during delithiation. However, in the experience of the current authors, $Li_{15}Si_4$ would still be formed if lithiation had been carried out a slower rates, such as *C*/40 instead of *C*/7.

3.6.1.4. Particle Fracture during the Cycling of Bulk Silicon. The two-phase reaction occurring during initial lithiation of Si and its narrow conversion front cause high stresses leading to particle fracture. This has been observed directly by in situ TEM, as shown in Figure 26. Acoustic emission (AE) studies have also shown that massive fracturing occurs during the lithiation of bulk x-Si.[157] Figure 28 shows contours indicating AE activity

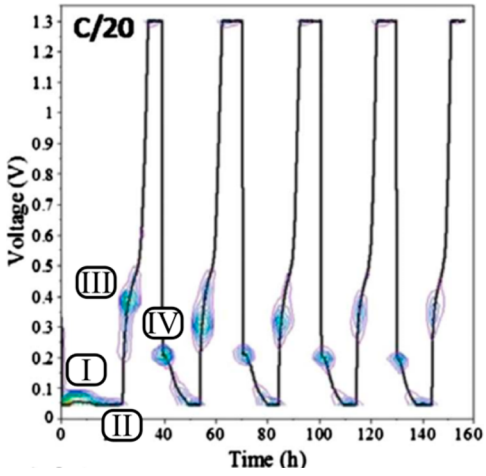


Figure 28. Contours of acoustic emission activity indicating fracture. Roman numerals correspond to those in Figure 24. Adapted with permission from ref 157. Copyright 2010 The Electrochemical Society.

corresponding to particle fracture. This figure has been labeled with roman numerals corresponding to those in Figures 24 and 25. Particle fracture also occurs during the two-phase delithiation of $Li_{15}Si_4$.[157] These observations are in agreement with the long-standing theory that two-phase reactions in alloy materials are detrimental to cycle life, as discussed in section 3.4. In contrast, the lack of a well-defined lithiation front during the cycling of a-Si helps reduce the stress occurring during expansion and minimizes particle pulverization. Figure 28 shows that the fracture events during the lithiation of amorphous Si ("IV") are considerably less than those occurring during the lithiation of crystalline Si ("I") due to the absence of a two-phase reaction.[157] By maintaining the potential of Si above 170 mV and thereby avoiding $Li_{15}Si_4$ phase formation (and associated two-phase regions), Obrovac and Krause were able to cycle bulk Si for 100 cycles with little fade.[161] Many theoretical and numerical models have been proposed to calculate the stresses that occur during Si lithiation, for which we refer the reader to McDowell et al.'s review.[13]

3.6.2. The Electrochemistry of Nanosized Silicon. The complete lithiation of Si causes an expansion of approximately 280% leading to considerable concerns related to pulverization of particles. Control of pulverization and mitigation of disconnection through particle size has been a long-standing approach in the field.[20] Many groups have therefore proposed nanosized Si (n-Si) as an answer to capacity fade, and this approach has been the subject of a number of reviews.[18,168−170] Many implementations have been exemplified, where the n-Si is present as an independent component of the electrode and directly in contact with the binder/electrolyte, including Si nanoparticles,[171−182] Si nanowires,[117,183−190] nanotubes,[191−193] Si thin flakes,[194,195] Si nanopillars,[107,196,197] Si nanospheres,[198,199] nanostructured spheres,[200] and even combinations of nanoparticles and nanowires.[201] In other approaches, the n-Si is coated, encapsulated, or nanodispersed, typically in some form of carbon, thereby avoiding direct contact with the electrolyte.[154,187,202−208] While the electrochemistry of n-Si is very similar to that of bulk Si, nanosizing has important consequences on particle fracture, $Li_{15}Si_4$ formation, SEI growth, and packing density.

3.6.2.1. Fracture Control via Nanosizing. The early conclusions that nanosized particles would limit particle fracture and pulverization[20,173,209] have been beautifully confirmed in a number of recent in situ TEM experiments detailing the size-dependence of n-Si fracturing.[166,179,180,188,197] These studies show that Si nanowires[188]/nanopillars[197] and nanoparticles[179,180] have a critical size of approximately 300 and 150 nm, respectively, under which fracture during lithiation is avoided. In all cases, fracturing starts at the surface of the nanosized Si in the lithiated region and propagated inward. Interestingly, amorphous Si particles have a much larger critical size of at least 870 nm, presumably due to improved kinetics, a broader lithiation front, and isotropic expansion, all helping to lower the lithiation stresses.[166]

3.6.2.2. $Li_{15}Si_4$ Suppression in Nanosized Si. While a relatively clear consensus exists for $Li_{15}Si_4$ as the final phase of bulk Si lithiation, there are various accounts of final lithiation products for n-Si. Recent in situ TEM studies present a strong argument for $Li_{15}Si_4$ as being the final phase in fully lithiated n-Si, as it was directly observed in various nanowires,[159] in CNTs coated with a-Si,[210] and nanoparticles.[180,208] On the other hand, McDowell et al. observed $Li_{15}Si_4$ only in some cases for a-Si nanoparticles by in situ TEM.[166] Using the features of the delithiation voltage curve, and in some cases XRD, Wang et al. found $Li_{15}Si_4$ in bulk Si but not Si nanoparticles,[211] Erk et al. found the presence of $Li_{15}Si_4$ dependent on lithiation rate and binder chemistry for Si nanoparticles.[212] Chevrier et al. saw the presence of $Li_{15}Si_4$ gradually disappear in Si nanoparticles with cycle number and reappear if lithiated at a smaller current.[12] While many papers do not discuss the presence or absence of $Li_{15}Si_4$, the characteristic delithiation voltage plateau at 0.45 V can be used to determine if $Li_{15}Si_4$ was present. For example, a study of the delithiation voltage profiles of nanowire Si in Figure 2c of ref 184 reveals a clear $Li_{15}Si_4$ plateau for *C*/20, but its absence at *C*-rate, even though the nanowires had been lithiated to the same lower cutoff voltage of 10 mV. On the basis of the literature reviewed, it appears that $Li_{15}Si_4$ is also the final lithiation level for n-Si and its absence is a symptom of incomplete lithiation, which may occur even at potentials below 50 mV due to kinetic limitations.

3.6.3. The Electrochemistry of Thin Film Silicon. In most respects, the electrochemistry of thin film Si produced by various forms of physical and chemical depositions is identical to bulk Si and n-Si, including the initial amorphization of Si, the condition-dependent formation of $Li_{15}Si_4$, and a-Si formation resulting from delithiation. However, the form factor of thin film Si results in interesting phenomena such as the possible suppression of $Li_{15}Si_4$ formation and "mudcracking".[112,113,213] Furthermore,

dx.doi.org/10.1021/cr500207g | *Chem. Rev.* 2014, 114, 11444−11502

thin films are particularly conducive to in situ thickness[100] and stress measurements,[115,149,214,215] while the typical absence of binder and the low surface area to capacity ratio of thin films remove some of the implementation variability found for other types of Si. Finally, lithography and other MEMS techniques can be used for the production of well-defined structures.[196,216,217]

3.6.3.1. Impact of Film Thickness on Mudcracking. Figure 22 shows a sputtered 250 nm Si thin film that has undergone "mudcracking" into micrometer scale islands during cycling.[112] In situ optical and AFM studies of SiSn thin films have shown that cracking occurs during delithiation and that the islands maintain a central connection to the substrate, expanding and contracting isotropically with further lithiation and delithiation.[111] The cracking and cycling performance of the thin films depends on the thickness and overall dimensions of the film as well as the nature of the substrate.

Thinner films are consistently found to have superior cycling performance as compared to thick films.[112,113,163,173,213,218] A comparison of 250 nm and 1 μm thick Si thin films showed the 1 μm film buckling and delaminating from the Cu foil substrate.[112] Impressive cycling performance has been demonstrated using thin film Si, with 50−200 cycles with little fade under full depth of discharge.[173,219−221] Roughing the substrate surface[163,219,222] or sputtering a fresh interface layer for improved adhesion[223] improves cyclability. Mudcracking can be avoided by limiting the in-plane dimensions of the film to the micrometer scale, as exemplified with 8 μm × 8 μm sputtered squares on stainless steel,[100] or by making the film thickness very thin, as was found for a 20 nm sputtered Si thin film.[224]

3.6.3.2. Stress Evolution and $Li_{15}Si_4$ Suppression in Thin Film Silicon. Sethuraman et al. have studied the stress evolution in Si thin films in recent years.[115,149,214,215] Figure 29 shows that an a-Si thin film initially compresses elastically up to −1.75 GPa and then quickly undergoes plastic flow while maintaining a nearly steady compressive stress during lithiation.[214] Upon delithiation plastic flow is also found under tensile stress above 1 GPa. Stress−potential coupling has been proposed as a significant contributor to the voltage hysteresis of Si, on the order of 100−120 mV/GPa.[149] The ∼2.5 GPa hysteresis seen in Figure 29 therefore suggests a possible stress contribution of up to 0.3 V. As suggested by Sethuraman et al., the compressive stress can effectively limit the depth of lithiation achieved.[214]

Interestingly, most thin film studies show capacities that are less than the 3579 mAh/g theoretical capacity of Si and cycling curves that are devoid of $Li_{15}Si_4$ features, even at low rates.[100,163,173,220] In one study, $Li_{15}Si_4$ was not formed in 500 nm Si thin films, but observed in thicker films of 2.4 and 4.5 μm.[163] The previous section showed ample evidence for $Li_{15}Si_4$ formation in n-Si, for sizes much smaller than 500 nm; however, the n-Si was typically freestanding. It therefore appears that the substrate plays a significant role in altering the electrochemistry of thin film Si, possibly via a stress contribution. The formation of $Li_{15}Si_4$ in thin film Si is likely avoided due to incomplete lithiation stemming from stress-potential coupling imparted by the substrate. As the thin film increases in thickness, the role of the substrate likely decreases in importance and $Li_{15}Si_4$ formation can be achieved. Additionally, the mudcracking and delamination observed in thicker films would remove stress contributions from the substrate.

3.6.3.3. Surface Properties and Thickness Expansion of Thin Film Silicon. The planar geometry of thin films allows the study of Si without the use of binder or conductive additives while providing a well-defined surface that can be readily accessed.

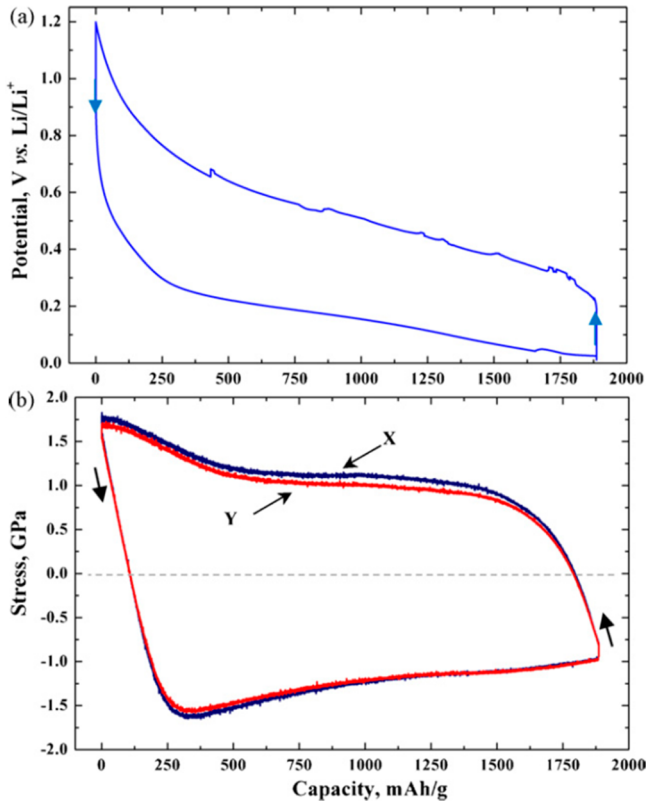


Figure 29. (a) Cell potential versus capacity curve corresponding to lithiation and delithiation of magnetron-sputtered amorphous Si thin film electrode cycled at *C*/4 rate between 1.2 and 0.01 V vs Li/Li^+, and (b) the corresponding stress calculated from the substrate curvature data using the Stoney equation. The curves labeled *X* and *Y* correspond to the stresses calculated from the averaged horizontal and the vertical displacement of the spots, respectively. The arrows in both figures indicate cycling direction. Reprinted with permission from ref 214. Copyright 2010 Elsevier.

Thin film Si has been notably used to experimentally determine the volume expansion of Si upon lithiation using in situ AFM, demonstrating a near 300% expansion for fully lithiated Si.[100] SEI characteristics on thin film surfaces have also been studied using this method and are discussed in section 4.3.1.[222,224,225] Nadimpalli et al. sputtered 20 nm Si films onto sputtered Cu to establish that the baseline irreversible capacity stemming from SEI formation is ∼200 mAh/m^2.[224] However, Al-Maghrabi et al. found an irreversible capacity of only 2% for Si sputtered onto electroplated Ni, which, taking the nominal area of the 5 mm diameter Ni pads, yields a surface normalized irreversible capacity on the order of ∼50 mAh/m^2.[226] They attributed the low irreversible capacity to the use of Ni instead of Cu and to the inert resin surrounding the active area and furthermore highlight the fact that the irreversible capacities spanning 13−33% in the literature are not well explained.

3.7. Alloys of the Active Elements

The study of alloys of the active elements is one of the most active areas of research in negative electrode materials development. The number of journal articles written on this topic is vast. Alloying combinations of active elements often result in electrochemical behavior, which is unlike the parent elements. Alloys also can include multiphase structures with small grain sizes. If the grain sizes of the active phases are made small enough, two-phase regions can be avoided during cycling.

dx.doi.org/10.1021/cr500207g | *Chem. Rev.* 2014, 114, 11444−11502

Additionally, alloying active elements with inactive elements can reduce volume expansion, leading to improved cycle life. A detailed knowledge of how alloy components effects cycling is needed to rationally design practical alloys. Here, an overview of the current understanding of the chemistry of different alloy combinations and their effect on cycling performance is given, from the point of view of practical alloy development.

To compare the energy densities of various alloys, the cell model developed in section 2 is used. Although research has been conducted on nonporous alloy film electrodes (as discussed in section 3.6.3), porous composite particle coatings have been the focus of the vast majority of research and have been implemented in commercial applications. Therefore, unless otherwise stated, we will assume that the active volume in the anode in our cell model is 70%, with the remaining 30% volume being occupied by porosity, binder, conductive diluents, etc. Considering the large variation in irreversible capacity between materials and with different electrolyte formulations, and considering there may be methods to deal with the irreversible capacity (section 7.1), the irreversible capacity of all anodes was assumed to exactly match that of the cathode in the cell model.

3.7.1. Active/Active Alloys. *3.7.1.1. Silicon−(Active Metal) Alloys.* In this section, a review of Si−(active metal) alloys is presented with estimates of their impact on cell energy given, where possible. The addition of active metals to silicon can have profound effects on its electrochemical performance. As discussed below, when Si is present in nanometer-sized regions within a matrix of other active elements, such as Zn and Sn, the formation of $Li_{15}Si_4$ can be suppressed, leading to good cycling. We speculate that the active matrix phase may play a similar role in suppressing the formation of $Li_{15}Si_4$ as does the substrate in Si thin films, which can suppress $Li_{15}Si_4$ formation via the generation of high mechanical stresses during volume expansion, as discussed in section 3.6.3.2.

3.7.1.1.1. Si−H. Hydrogenated amorphous silicon is produced during vapor deposition. Amorphous silicon particles with up to 58 atomic % hydrogen have been synthesized.[227] Because lithium hydride has a very high volumetric capacity (2613 Ah/L), we speculate that hydrogen content in highly hydrogenated silicons may have a significant effect on their electrochemical performance. Although numerous articles describe the cycling of vapor deposited silicon, we are not aware of any that have carefully examined the effect of significant hydrogen content on its electrochemistry.

3.7.1.1.2. Si−Mg. Research on Si−Mg alloys has been focused on Mg_2Si, the only binary compound in the Mg−Si system. Mg_2Si has a reversible capacity of about 1074 mAh/g and an average voltage of about 0.26 V.[3] This corresponds to the insertion of about 3 lithium atoms per formula unit. According to the standard lithiation model,[23] this corresponds to a volumetric capacity of 1254 Ah/L and 73% volume expansion. Putting these figures in our cell stack model results in a stack energy density of about 838 Wh/L, which represents a 15% energy improvement over a conventional graphite anode. Two mechanisms have been proposed for the lithiation of Mg_2Si.

Scheme I:[228−230]

$$Mg_2Si \xrightarrow{Li} Li_2MgSi + Mg \quad (21)$$

$$Mg \xrightarrow{Li} Li_xMg \quad (22)$$

$$Li_2MgSi \xrightarrow{Li} Li_xMg + Li_ySi \quad (23)$$

at low rates.[228]

Scheme II:[3,231]

$$Mg_2Si \xrightarrow{Li} Li_{critical}Mg_2Si \quad \text{(intercalation)} \quad (24)$$

$$Li_{critical}Mg_2Si \xrightarrow{Li} Li_{saturated}Mg_2Si + Mg + Li_xSi \quad \text{(where saturated} \approx 1) \quad (25)$$

$$Mg \xrightarrow{Li} Li_xMg \quad (26)$$

Although it is still not completely resolved which mechanism is correct, it is abundantly clear that the lithiation of Mg_2Si is completely different from its constituent elements,[3] as illustrated in the differential capacity curves shown in Figure 30.

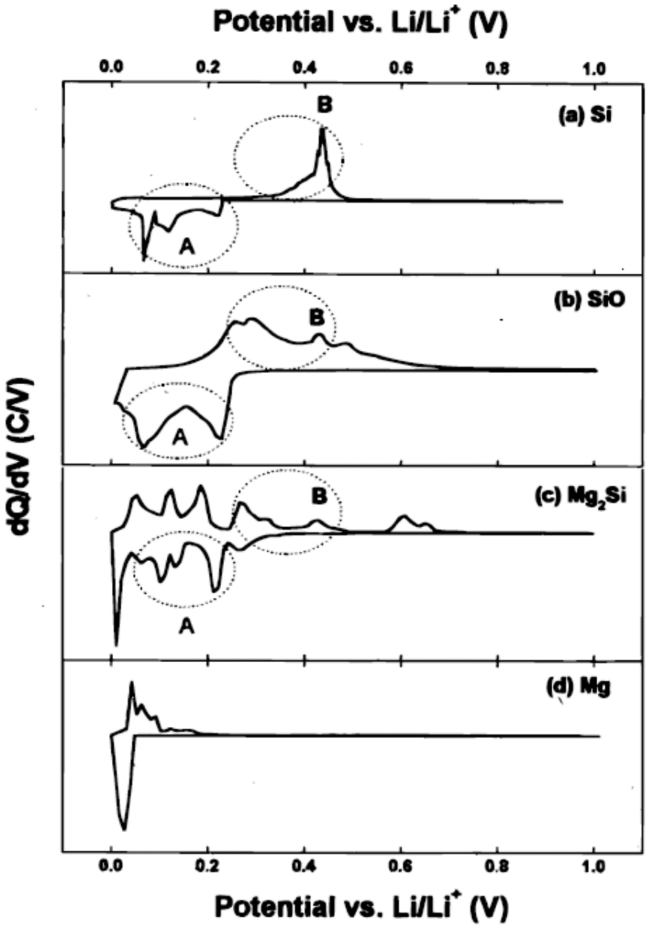


Figure 30. Differential capacity during the first cycle of different negative electrode materials. Si and SiO were tested with a constant current of 30 mA/g, and Mg_2Si and Mg were tested with a constant current of 10 mA/g. Reproduced with permission from ref 3. Copyright 1999 The Electrochemical Society.

Typically, Mg_2Si electrodes cycle poorly,[228] which has been thought to be due to magnesium extrusion during lithiation.[230] However, very thin 30 nm films of Mg_2Si have been shown to cycle at 2240 mAh/g for more than 100 cycles with no capacity fade.[232] Recently, somewhat improved cycling of bulk Mg_2Si particles has been achieved by carbon coating.[233]

3.7.1.1.3. Si−Ca. Wolfenstine reported the lithiation of crystalline and ball milled $CaSi_2$.[42] The voltage curve was sloping and featureless, with an average delithiation voltage of about 0.65

dx.doi.org/10.1021/cr500207g | Chem. Rev. 2014, 114, 11444−11502

V and a first lithiation capacity of almost 2000 mAh/g. Capacity retention was extremely poor. It is difficult to estimate the reversible capacity from the data presented. The lithiation mechanism in $CaSi_2$ is not known.

3.7.1.1.4. Si–Ag. Li, Si, and Ag are known to form the ternary phase $Li_8Si_5Ag_3$.[120] Hatchard et al. prepared Si_xAg_{1-x} films by combinatorial sputtering.[120] Differential capacity plots of these films were suggestive of the formation of $Li_8Si_5Ag_3$ at 0.7 V and Li–Ag phases at lower voltages. When the Ag content was 34 atomic % or less, Ag and Si regions in the film simultaneously aggregated during cycling, causing $Li_{15}Si_4$ to be formed at low voltage. At a high Ag content of 57 atomic %, the Si could no longer aggregate and no $Li_{15}Si_4$ was formed, even after many cycles. Nevertheless, any addition of Ag to Si above 15 atomic % was found to be detrimental to cycling, as compared to that of pure Si.[120] Si–Ag alloys have also been prepared by ball milling,[234,235] and Si/Ag multilayer films have been prepared by sputtering.[236] In contrast to the findings of Hatchard et al., Si–Ag alloys made by these methods show significant improvements in cycling over that of pure Si. In addition, Ag-coatings on silicon particles have been shown to improve cycling performance (see section 4.2).

3.7.1.1.5. Si–Zn. Si and Zn do not form any binary alloys, but a number of ternary Li–Si–Zn alloys are known. Alcantara et al. investigated lithiation and delithiation from layered Li_2ZnSi.[237] Delithiation of Li_2ZnSi resulted in the decomposition of the structure. Lithiation of Li_2ZnSi proceeded by an intercalation mechanism. Lithiation of up to 0.5 Li per formula unit resulted in little change in the unit cell. Higher lithiation amounts up to Li_3ZnSi resulted in more significant expansion of the interlayer spacing, which Alcantara et al. suspected was the cause of poor cycling characteristics. However, according to the lattice constants given, the volume expansion is only 2%, which is much less than graphite. The voltage curve of lithiated, then delithiated, Li_2ZnSi has about 0.5 V polarization. This is suggestive that some structural changes are occurring, rather than simple intercalation. The volumetric capacity of Li_2ZnSi is about 550 Ah/L, which is less than that of graphite.

Hatchard et al. investigated the lithiation of combinatorially sputtered $Si_{1-x}Zn_x$ ($0.12 \leq x \leq 0.62$) films.[238] During the initial lithiation of these films, the formation of binary Li–Zn and ternary Li–Si–Zn phases, such as $LiZn_9$, Li_2SiZn, and LiZn, was observed by in situ XRD. In films with high Zn-content, the formation of a new phase, thought to be $Li_4(SiZn_x)$, was also observed at full lithiation. After subsequent cycling, the films became amorphous, and these phases were no longer observed. In addition, the formation of the $Li_{15}Si_4$ was suppressed at all Zn contents. It was speculated that the formation of ternary Li–Si–Zn phases during cycling effectively dispersed the Zn and Si phases, as these elements could not diffuse apart during delithiation. Therefore, Si–Zn alloys tended to become more amorphous as cycling progressed. Improved cycling was claimed as the Zn-content increased, due to this amorphization effect. However, we point out that the improved cycling was also concurrent with a significantly lowered capacity and, therefore, less volume expansion.

Hatchard et al. make no attempt to explain the trend in capacity of their $Si_{1-x}Zn_x$ films, which vary in capacity from about 3000 to 1000 mAh/g between $0.12 \leq x \leq 0.62$. However, we note that this corresponds very well to a theoretical capacity based on the formation of LiZn and $Li_{15}Si_4$, which ranges from 2814 to 1070 mAh/g in the same range of x. This corresponds to volumetric capacities of 2157–1912 Ah/L, based on the standard lithiation model.[23] The CE of these Zn-containing alloys during cycling was also not discussed by Hatchard et al. Therefore, it is unclear whether Si–Zn alloys suffer from the poor CE exhibited by other Zn-containing alloys (see section 3.1.3.2).

3.7.1.1.6. Si–B. Si–B alloys are discussed in section 3.7.2.3.

3.7.1.1.7. Si–Al. According to the equilibrium Si–Al phase diagram, Si and Al do not form binary alloys, but do form a number of ternary alloys with lithium.[239−244] Understanding the electrochemical performance of these ternary phases is key to understanding the performance of Si–Al alloys. Tillard et al.[242] and Liu and Obrovac[244] studied the lithiation of LiAlSi. About one formula unit of Li could be inserted into LiAlSi, with the formation of $Li_7Al_3Si_4$ in a two-phase process. The cycling performance of LiAlSi was found to be very poor, which was thought to be due to the two-phase lithiation process, because such processes are associated with poor cycle life (see section 3.4).[244] Interestingly, no Li could be removed from LiAlSi up to 1.2 V. Liu and Obrovac even noted that LiAlSi only reacted very slowly with water, suggesting that the lithium is kinetically trapped.[244] Tillard et al. investigated the electrochemistry of Li_5AlSi_2 and Li_9AlSi_3.[242] In contrast to LiAlSi, Li could be partially removed from both of these materials during cycling. While the cycling performance of Li_5AlSi_2 was exceeding poor, Li_9AlSi_3 was found to cycle reversibly in a single-phase region in the composition range $4.25 \leq x \leq 11$ in Li_xAlSi_3, as shown in Figure 31.

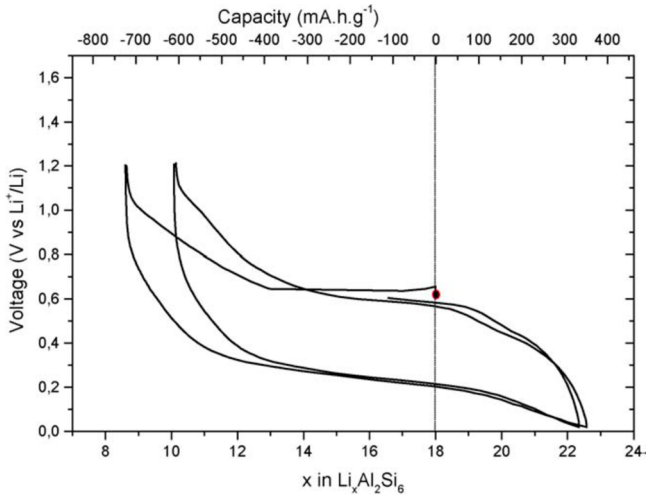


Figure 31. Voltage curve of Li_9AlSi_3 at $C/100$ rate (the composition limits are relative to two unit cells). Reproduced with permission from ref 242. Copyright 2005 Elsevier Masson SAS.

Fleischauer et al. studied the lithiation of combinatorially sputtered $Al_{1-x}Si_x$ ($0 < x < 1$).[5] For high and low values of x, the reversible capacity obtained during cycling was found to agree well with that expected if LiAl and $Li_{15}Si_4$ are formed at full lithiation. However, for intermediate values of x, the capacity was significantly lower than predicted by theory. This was thought to be due to the formation of Li–Al–Si phases from which Li could not be removed, such as LiAlSi. As shown in Figure 32, this effect becomes more apparent as cycling progresses, causing significant capacity fade when the Al:Si ratio is approximately 1:1. Presumably more Li–Al–Si phases form during cycling of these compositions. On the other hand, Al in low amounts (<20 atomic %) was found to suppress $Li_{15}Si_4$ formation and did not form ternary Li–Al–Si phases. Such compositions, like

dx.doi.org/10.1021/cr500207g | Chem. Rev. 2014, 114, 11444–11502

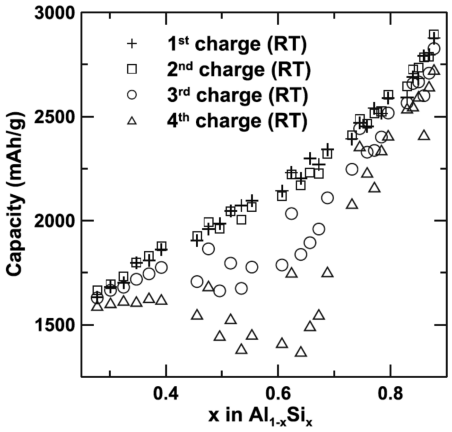


Figure 32. Delithiation capacities of cycles 1−4 of $Al_{1-x}Si_x$ thin films. Reproduced with permission from ref 5. Copyright 2008 The Electrochemical Society.

$Al_{0.25}Si_{0.75}$, were found to have cycling performance superior to that of silicon.

Assuming the average voltage of Al−Si alloys is about 0.40 V (which is about equal to the average voltage of Si and Al), then the energy of full cells comprising Al−Si alloys simply varies between those of pure Al and pure Si. On the basis of the standard lithiation model,[23] we calculate $Al_{0.25}Si_{0.75}$ to have a volumetric capacity of about 1965 Ah/L with a volume expansion of 194%. This results in a full cell energy of about 901 Wh/L or a 24% energy improvement as compared to graphite.

3.7.1.1.8. Si−C. Conceptually, Si−C composites are very attractive, for they combine high volumetric energy silicon with low volume expansion carbon. Because carbon is active toward lithium, the silicon can be completely encased within a carbon matrix without blocking lithium diffusion. These properties create a versatile pallet for design of Si−C-based materials. Typically the Si phase is in the form of nanoparticles, to avoid two-phase regions during cycling, and are encased in a carbon matrix, which serves to reduce volume expansion and lower reactivity with the electrolyte.[245] However, during the synthesis of Si−C composites, Si and C have a tendency to react to form SiC, which is usually inactive toward lithium.

Here, the basic principles of Si−C alloys will be first discussed. This will be followed by a discussion of complex Si−C materials with designed microstructures, which have been the attention of much research activity of late. Usually the carbon in Si−C composite materials is disordered and highly porous. As such, it is difficult to estimate their volumetric capacities accurately. Therefore, we shall not even attempt to calculate it. Instead, the following sections will be limited to only a general description of the chemistry of Si−C, and how it affects trends in gravimetric capacity, which is useful as a guide in preparing these materials. It is rather unfortunate that after years of work in this field by many groups, we cannot estimate how most of their materials would impact cell energy. We encourage future workers in this field to measure the density of these materials and how they expand during lithiation, so that their usefulness in practical applications can be determined.

3.7.1.1.8.1. The Chemistry of Si−C Composites. A variety of methods have been used to make Si−C composites, including CVD,[154,203] pyrolysis of silicon containing polymers,[246] pyrolysis of n-Si with polymers (and optionally graphite),[247] high energy ball milling (and optionally heating),[248−251] dispersion of n-Si in a carbon aerogel,[252] and sputter deposition.[251] More advanced Si−C composites with complex designed microstructures will be discussed in section 3.7.1.1.8.2. Dahn et al. reviewed studies of Si−C composites made by a variety of methods, and concluded that Si−C composites made by "gentle methods", such as physically mixing n-Si with carbon, resulted in capacities that were consistent with a physical mixture of Si and carbon.[251] However, Si−C composites prepared by high energy ball milling or pyrolysis at temperatures at or above 900 °C resulted in capacities that were consistent with the formation of carbon and inactive SiC. Figure 33 compares the predicted capacity based on

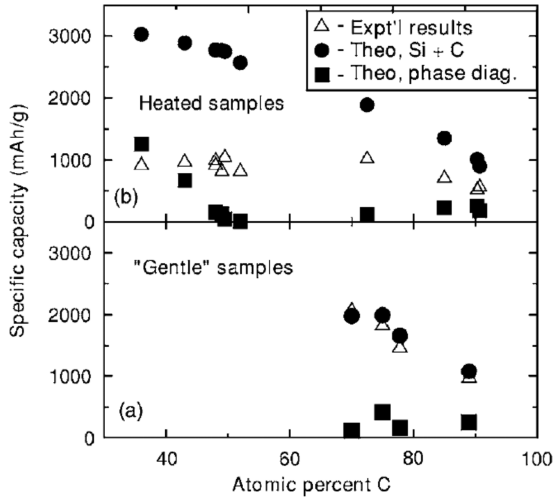


Figure 33. Specific capacity versus atomic percent C in Si−C composites and nanocomposites. The bottom panel is for the "gentle" samples, and the top panel is for the "heated" samples. The "△" are the results from literature. The "●" and "■" are the theoretical predictions based on a physical mixture of Si and C or all of the Si reacting with C to form SiC, respectively. Reproduced with permission from ref 251. Copyright 2007 The Electrochemical Society.

this model to those reported in the literature for Si−C composites. It was noted that SiC may not be detectible by XRD, because it is often formed in an amorphous state.[251] Materials that have been prepared between these extremes had capacities that also lay between the two extremes.

SiC formation and Si−C electrochemical performance have been found to be highly dependent on the precursors used. During pyrolysis, for example, SiC was found to form readily in petroleum pitch/polysilane blends above 800 °C, resulting in lowered reversible capacity.[253] Si−C made from pitch/polysilane blends at 800 °C was found to have high irreversible capacities (>30%), due to the high hydrogen content of the carbon formed at this temperature. Si−C formed from the pyrolysis of Si/PVC blends had less irreversible capacity, especially if graphite was added to the precursors before pyrolysis.[247] SiC has been reported to form more readily from PVDF than from other polymers.[254] Kumpta's group has found that the formation of SiC could be effectively suppressed during the ball milling of Si and C by using polymer additives that act as diffusion barriers between Si and graphite, inhibiting their reaction.[255,256]

Despite the general agreement that the SiC phase is inert in Si−C composites, it has been reported that some forms of SiC are active toward lithiation. Lipson et al. reported that 6H SiC could be lithiated with up to one Li per formula unit.[257] Kumari et al. have reported that n-SiC prepared by CVD can insert up to 2 Li per formula unit and show cycling with reversible capacity of 1332 mAh/g between 0 and 2 V, with an average delithiation

dx.doi.org/10.1021/cr500207g | Chem. Rev. 2014, 114, 11444−11502

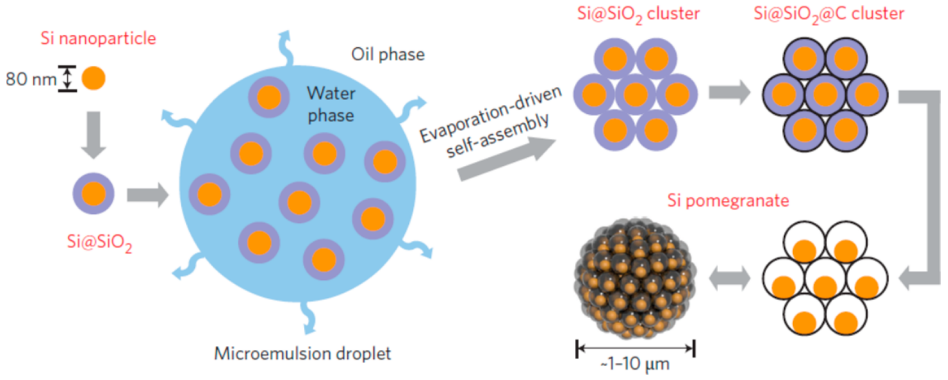


Figure 34. An example of Si−C particle engineering with a sacrificial SiO_2 scaffold. Si nanoparticles are first coated with SiO_2, followed by cluster formation in a microemulsion, carbon coating by pyrolysis, then removal of the SiO_2 scaffold in HF. Reprinted with permission from ref 11. Copyright 2014 Macmillan Publishers Ltd.: Nature Nanotechnology.

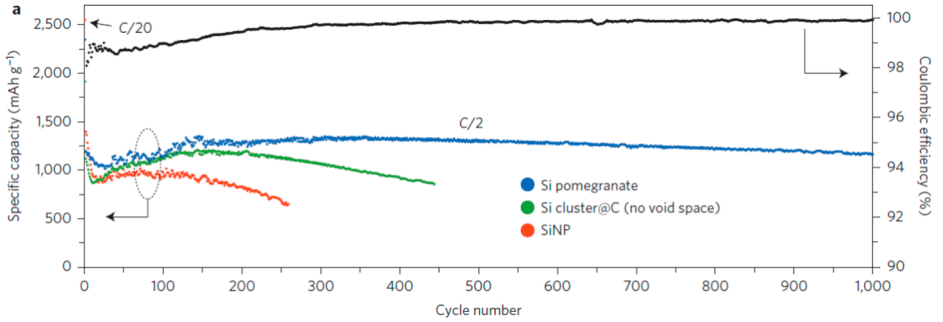


Figure 35. Cycling performance of Si−C "pomegranate" microstructures with void spaces for expansion and microstructures with no void spaces. The cycling is compared to bare Si nanoparticles (SiNP). Reprinted with permission from ref 11. Copyright 2014 Macmillan Publishers Ltd.: Nature Nanotechnology.

voltage of about 1 V.[257] 200 charge/discharge cycles are shown with little capacity fade. Ex situ XRD studies found little change in the diffraction pattern of SiC during cycling, making the lithiation mechanism difficult to explain.

3.7.1.1.8.2. Si−C Composites with Complex Microstructures. In the past few years, new synthesis techniques have enabled the purposeful design of complex Si−C microstructures. One method is the use of silica as a scaffold over which the carbon matrix can be formed.[11,258−260] This method is illustrated in Figure 34, which describes the basic concepts. The particles thus formed have a structure in which the Si resides in voids within a carbon matrix, which have been coined as pomegranate-type particles.[11] The voids can be designed such that they can exactly accommodate the expansion of Si during lithiation, without any outward expansion of the particle.[11,259,260] Furthermore, such particles can present a low surface area in contact with the electrolyte.[11]

Impressive cycling performance has been demonstrated for Si−C materials designed with these concepts. Figure 35 shows the cycling performance of the Si−C pomegranate type particles described in Figure 34. 1000 cycles with little fade is achieved when void space is present to accommodate the Si volume expansion.[11] Furthermore, the structures were shown to be robust toward electrode calendering, with calendered electrodes achieving a coating capacity of 900−1270 Ah/L. From the text of Liu et al., one can estimate the average voltage during delithiation as 0.47 V.[11] Using the cell stack model described in section 2, this corresponds to a stack energy density of 868 Wh/L or a 20% improvement over graphite. These numbers are impressive for a finished electrode. However, it was stated that further improvements are needed for such materials to be practical because of low initial Coulombic efficiency of the amorphous carbon used to form the carbon matrix.[11]

A second method that enables a structural design of complex Si−C microstructures derives from the magnesiothermic reduction of silica.[261−263] In this process, which is illustrated in Figure 36, a silica precursor is heated with magnesium powder in an inert atmosphere, to form MgO and Si. The MgO can then be removed by treatment with HCl solution. Surprisingly, the silicon that forms by this process retains the microstructure of the silica precursor. Pyrolysis or other means can then be used to infiltrate carbon into the structured silicon. A number of precursors for this process have been used, including diatomite, which takes advantage of naturally occurring silica microstructures.[262] Another method employed to make complex Si−C structures is to first form a porous carbon matrix, onto which

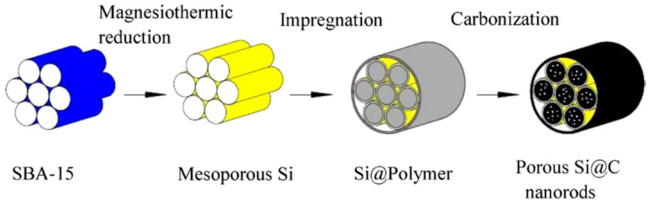


Figure 36. Reaction scheme illustrating the formation of Si−C composites via magnesiothermic reduction of a structured silica precursor. In this case, the precursor is an ordered hexagonal mesoporous silica designated SBA-15. Reprinted with permission from ref 261. Copyright 2012 Elsevier.

dx.doi.org/10.1021/cr500207g | *Chem. Rev.* 2014, 114, 11444−11502

silicon can be deposited. Yao et al. used this method to form complex Si−C composites using crab shells as a template onto which they deposited carbon. The $CaCO_3$ was then dissolved, leaving a porous carbon network onto which Si was deposited by CVD.[264] Recently, Zhao et al. have grown Si nanowires within a carbon matrix.[265]

Although these methods have produced elegant Si−C microstructures, their practical utility is unclear because a proper analysis of their use in cells has rarely been presented. Typically only gravimetric capacities are reported, which in itself, as discussed in section 2, is not useful for predicting cell energy, especially for porous materials. This is highlighted by a telling statement in a recent article: "Worth nothing is that the mesoporous Si/C composite here reported shows a discharge capacity of 895 mAh g^{-1}..."[263] This statement is either intentional or a misprint. In either case, it is true. Reporting only the gravimetric capacities of porous materials is worth nothing in predicting their impact on the energy of a Li-ion cell of fixed volume. Without knowledge of the void volume in such porous materials, an estimation of their volumetric capacity is not possible. In addition to having high void volumes, which decrease their volumetric capacities, such highly porous structures can have high surface area, which has been associated with instability during thermal abuse and increased irreversible capacity.[266] The dearth of information regarding the surface area, void volume, volumetric capacity, and ultimately a reasonable analysis of the usefulness of Si−C materials in practical cells is astounding, so much so, that there is not enough information to determine the impact most of these materials may have on cell energy. To ensure progress in this area, we encourage researchers to provide such information and referees to insist that it is disclosed.

There are rare cases where Si−C materials have been analyzed in sufficient detail such that their volumetric capacity and impact on cell energy can be estimated. The example of "pomegranate" Si−C has already been described above. In another instance, Tao et al.[261] have described Si−C nanorods made by magnesiothermal reduction in sufficient detail to estimate its impact on cell energy and provide a good example of how this can be done. The Si−C nanorods made by Tao et al. were reported to have the properties listed in Table 5.

Table 5. Properties of a Si−C Composite Derived from Data Reported by Tao et al. in Reference 261

Si/C ratio	surface area (m^2/g)	ICE	total void volume (cm^3/g)	capacity (mAh/g)
55/45 w/w	437	61%	0.26	850

The surface area is very high, which is not surprising for such microporous structures. On the basis of the densities of Si and C, we calculate that the void volume corresponds to about 37% of the total particle. A Si and C particle comprising 37% porosity and having the weight ratio of Si/C 55/45 has a theoretical density of 1.43 g/mL. Because the reported reversible capacity is 850 mAh/g, if one assumes that no volume expansion takes place during lithiation (which may or may not be a good assumption), the volumetric capacity is about 1800 Ah/L. Using an average voltage of 0.46 V in our cell stack model, this corresponds to a stack energy density of about 866 Wh/L or a 19% energy improvement as compared to graphite. Here, zero irreversible capacity and a 70% by volume active material loading is assumed. Of course, including the 29% irreversible capacity reported for this material negates this advantage. Nevertheless, simple analyses like this one are highly useful to show that such materials have promise. We again encourage similar analyses by researchers in this area.

3.7.1.1.9. Si−Sn. The Si−Sn system has been studied extensively by the Dahn group[4,100,120,267,268] and by Ahn et al.[269] Sputtered films of $Si_{1-x}Sn_x$ showed no tendency to form crystalline phases during cycling. Furthermore, additions of Sn to Si were reported to result in decreased irreversible capacity and fade rate, as compared to pure Si.[268] However, only 10 charge/discharge cycles were shown. Ahn et al. also reported increased capacity retention of Si−Sn films over pure Si, but only showed 15 cycles.[269] Hatchard et al. showed that the capacity of sputtered $Si_{1-x}Sn_x$ films could be accurately predicted as the linear combination of the theoretical capacity of Si (as $Li_{15}Si_4$) and Sn (as $Li_{4.4}Sn$).[268]

A $Si_{0.66}Sn_{0.34}$ thin film has a reversible capacity of about 1800 mAh/g and an average delithiation voltage of about 0.5 V.[4] Such a thin film would have a volumetric capacity of about 2160 Ah/L with a 264% volume expansion, according to the standard lithiation model.[23] This results in a stack energy density of about 946 Wh/L in our cell model (assuming a zero porosity $Si_{0.66}Sn_{0.34}$ thin film), which represents a 30% improvement over graphite. These figures are impressive; however, the question of the practicality of sputtering for the manufacture of anode materials on a commercial scale has not been answered.

3.7.1.2. Tin−(Active Metal) Alloys. The alloying of Sn with active metals has been shown to improve cycling significantly as compared to pure Sn. This has been achieved in Sn−M alloys (M = Ag, Sb) in which multiple coexisting phases are formed during lithiation.[108,270−276] Such mechanisms tend to preserve alloy microstructure during cycling and suppress the aggregation of Sn into large crystallites. In Sn−C alloys, nanoregions of Sn can be isolated in a carbon matrix such that they do not aggregate during cycling.[6,277−280] Furthermore, the void space in such composites is thought to accommodate the volume expansion of Sn, leading to impressive cycle life.

3.7.1.2.1. Sn−Mg. Larcher et al. and Aldon et al. investigated the lithiation mechanism of Mg_2Sn by in situ XRD and Mössbauer spectroscopy.[281,282] They proposed a three-step reversible mechanism:

$$Mg_2Sn \xrightarrow{Li} Li_xMg_2Sn \quad (27)$$

$$Li_xMg_2Sn \xrightarrow{Li} Li_2MgSn + Mg \quad (28)$$

$$Mg \xrightarrow{Li} Li_xMg \quad (29)$$

The first step in this mechanism was associated with reduced volume expansion (1.3%) as compared to the expected value (30%), leading to their speculation that it proceeds by Li filling empty octahedral lattice positions in Mg_2Sn. After this step, Li_2MgSn is formed with the extrusion of Mg, which then can go on to react with more Li at low voltages. The reaction was fully reversible and was shown to accommodate 4.4 Li overall per Mg_2Sn formula unit or 704 mAh/g. Using the standard lithiation model, this corresponds to 1500 Ah/L, with an associated 100% volume expansion.[23] According to the GITT curve shown in ref 281, the average voltage during delithiation is about 0.45 V. Using our cell model with a 70% active volume Mg_2Sn electrode results in a 837 Ah/L stack energy density, corresponding to a 15% improvement over graphite. Unfortunately, poor cycle life was reported for Mg_2Sn, presumably due to loss of Mg during its

dx.doi.org/10.1021/cr500207g | Chem. Rev. 2014, 114, 11444−11502

reaction with lithium.[281] Cycling was improved when the voltage was limited to avoid this reaction.

3.7.1.2.2. Sn−Ag. Yin et al. have conducted a thorough analysis of ball milled alloys in the entire composition range of the Ag−Sn binary system.[270] Figure 37 shows the cycling

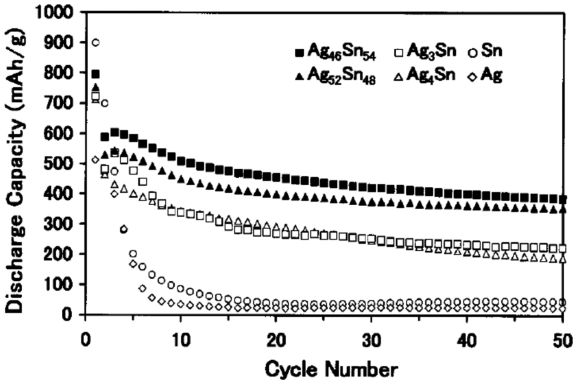


Figure 37. Cycling performance of Ag−Sn alloys. Reproduced with permission from ref 270. Copyright 2003 The Electrochemical Society.

performance of representative alloys in this series. Cycling performance is best for intermediate Ag−Sn compositions. An analysis of features in the voltage curve and XRD patterns of electrodes at different states of charge revealed a complex lithiation mechanism, in which $LiAg_2Sn$ and Li_2AgSn are formed as intermediate phases before $Li_{4.4}Sn$ and LiAg are formed at full lithiation. Interestingly, upon delithiation the reverse reaction proceeds, except Li_2AgSn remains and accumulates during cycling. This was thought to be the origin of accumulated irreversible capacity during cycling. However, the multiphase structure that is formed as a result was thought to be the reason for the observed improved cycling over pure Sn or Ag. From the voltage curve shown, $Ag_{52}Sn_{48}$ has an average delithiation voltage of about 0.5 V and a reversible capacity of about 350 mAh/g after 50 cycles. In our cell model with a 70% active volume negative electrode, this corresponds to an 822 Ah/L stack energy density or a 13% improvement over graphite.

3.7.1.2.3. Sn−Zn. Sn and Zn are immiscible and do not form ternary compounds with lithium. Accordingly, the electrochemistry of Sn−Zn alloys appears to be that of a simple mixture of Sn and Zn.[283−285] However, some improvement in cycling has been shown in these studies over that of pure Sn, which is thought to be due to an improved electrode microstructure.

3.7.1.2.4. Sn−Al. Similarly to Sn−Zn, Sn and Al are immiscible and do not form ternary compounds with lithium. Accordingly, the electrochemistry of Sn−Al alloys appears to be that of a simple mixture of Sn and Al.[286,287] However, some improvement in cycling has been shown in these studies over that of pure Sn, which is thought to be due to an improved electrode microstructure. It has also been noted that the addition of Sn to Al increases Li diffusion substantially.

3.7.1.2.5. Sn−C. Much research has been conducted recently in the field of Sn−C composites. These typically consist of well-dispersed Sn nanoparticles in a porous carbon matrix. Such structures can form from the simple pyrolysis of a tin precursor (e.g., $SnCl_2$ or an organotin compound) with an organic polymer.[6,277−280] Early publications reported structures comprising 200 nm Sn embedded in 2−10 μm sized C particles. As research has progressed, the size of the Sn regions has been reduced. For example, Xu et al. have recently reported the synthesis of 10 nm Sn embedded in 114 nm C particles.[6] Images of these particles are shown in Figure 38, and their differential

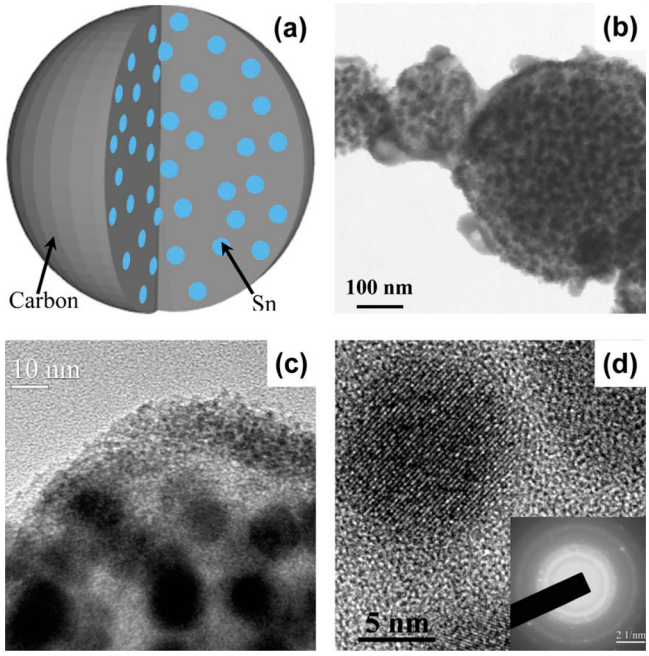


Figure 38. (a) Diagram of Sn−C composite particle, (b) TEM image, and (c,d) high-resolution images of the nano-Sn/C composite particles. Inset: SAED image. Reprinted with permission from ref 6. Copyright 2013 American Chemical Society.

capacity curve, voltage curve, and cycling performance are shown in Figure 39a−c. After the first cycle, the differential capacity curve does not change, which indicates that the Sn regions do not aggregate during cycling. The material has good capacity retention with little fade after 130 cycles. Good cycling in Sn−C composites is generally believed to result from the ability of the pores in the carbon matrix to accommodate the volume expansion of Sn during cycling.[279,280,288] However, the irreversible capacity of Sn−C materials is usually high (e.g., 31%, for the voltage curve of Xu et. al shown in Figure 39b). This is thought to also be a consequence of using porous carbon. Recently, Tan et al. have shown that coating the Sn−C with carbon by a CVD process can reduce the irreversible capapacity.[279] Using this method, the irreversible capacity of a Sn−C composite was reduced drastically from 40.1% to 18.8%.

As with Si−C composites, many complex Sn−C composite structures have been designed, such as yolk−shell structures,[289] Sn core/carbon sheath nanocables,[290] Sn−C embedded on a Ni foam,[291] and electrospun Sn/C fibers.[278,292] Such structures are generally reported as having void space that can accommodate the volume expansion of Sn within a carbon scaffold. Sn-graphene nanostructures have also been reported.[293,294] The graphene provides a substrate for Sn, which is believed to result in improved cycling.

Similarly to Si−C composites, the impact of the performance of most of the above materials on commercial Li-ion cells is impossible to determine from the information provided. This is because the void volume contained in these porous materials can be significant, making an estimation of their density and, consequently, their volumetric capacity impossible. We have found only two reports where sufficient information is given to calculate the impact of Sn−C composites on cell performance.

dx.doi.org/10.1021/cr500207g | *Chem. Rev.* 2014, 114, 11444−11502

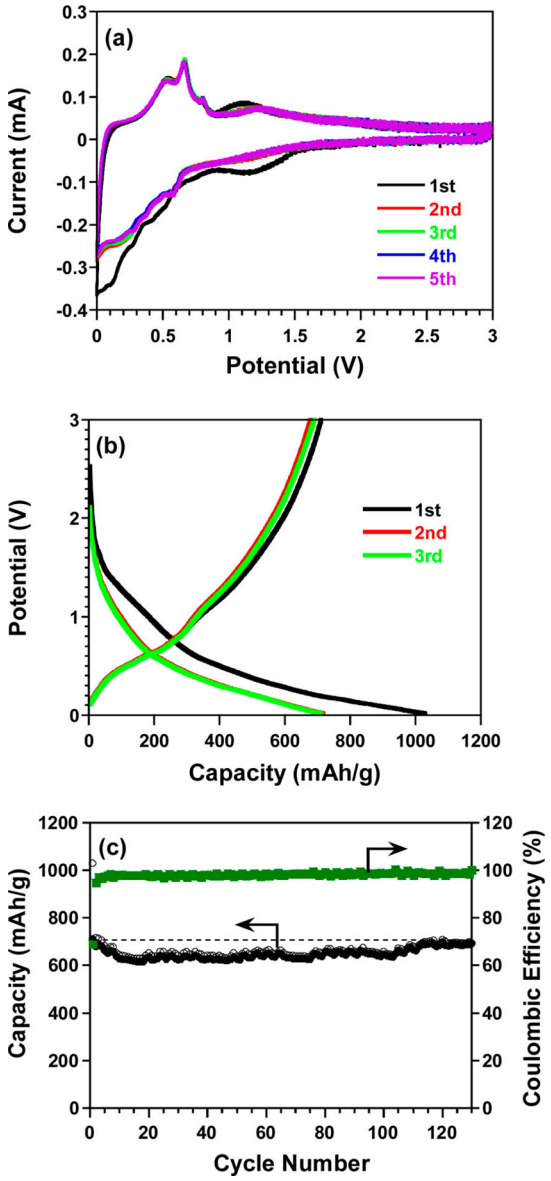


Figure 39. Electrochemical performance of a n-Sn−C composite. (a) Cyclic voltammograms of the initial five cycles scanned between 0−3 V at a rate of 0.1 mV/s, (b) charge/discharge profiles at the initial three cycles, and (c) cycling performance at 0.02−3 V and 200 mA/g. Reprinted with permission from ref 6. Copyright 2013 American Chemical Society.

Xu et al. reported the gravimetric capacity of Sn−C particles made by pyrolysis as 710 mAh/g and the density to be about 4.05 g/mL.[6] Assuming the volume expansion is zero (void volume accommodates all Sn-expansion), this corresponds to a volumetric capacity of 2876 Wh/L. From Figure 39b, the average voltage may also be estimated at 1.5 V. This information is sufficient to calculate the energy density of a cell stack, using our cell model. This calculation results in a stack energy density of only 661 Ah/L or a 9% reduction in cell energy as compared to a standard graphite coating. This result is due to the high average voltage of the Sn−C composite reported by Xu et al. A similar calculation can be made for the CN-encapsulated Sn nanoparticles by Wang et al.[7] These materials were reported to have a volumetric capacity of 1489 Ah/L, and an average voltage of 1.5 V may be estimated from the voltage curve shown. This results in a stack energy density of only 580 Wh/L or a 20% reduction in cell energy as compared to a standard graphite coating. Again, this low value is due to the high average voltage of the Sn−C composite.

We suspect that not all Sn−C composites would result in such low cell energies; however, it is not possible for us to tell. This exemplifies the importance of realistic cell energy calculations when designing battery materials.

3.7.1.2.6. Sn−Si. Si−Sn alloys are described in section 3.7.1.1.9.

3.7.1.2.7. Sn−Sb. Sn−Sb alloys have been shown by a number of groups to have cycling performance superior to that of pure Sn.[108,271−276] There is no agreement within these studies as to which Sn/Sb ratio results in the best cycling performance. However, it is generally agreed that the SnSb phase has good cycling characteristics. SnSb lithiates according to a two-step reaction:

$$\mathrm{SnSb} \xrightarrow{\mathrm{Li}} \mathrm{Li_3Sb} + \mathrm{Sn}\ (\sim 0.82\ \mathrm{V}) \tag{30}$$

$$\mathrm{Sn} \xrightarrow{\mathrm{Li}} \mathrm{Li_{4.4}Sn}\ (<0.66\ \mathrm{V}) \tag{31}$$

resulting in a theoretical capacity of 825 mAh/g. This two-step mechanism is believed to impart good cycling characteristics, where the initial reaction creates a Li_3Sb matrix that can "buffer" the volume expansion of the Sn phase. The presence of Sb also improves lithiation kinetics. The two-phase separation during cycling is further thought to relieve mechanical strain, result in a nanostructured morphology during cycling, and prevent the Sn-phase from aggregating during cycling.[274] A detailed in situ X-ray microscopy study by Chao et al. seems to verify this behavior.[108] While Sn particles lithiate via a two-phase reaction zone, Li_3Sb is first formed during the lithiation of SnSb, forming cracks throughout the particle. After this initial step, the particle homogeneously expands due to fast Li^+ diffusion in the cracked structure. Yant et al. demonstrated enhanced cycling characteristics when the voltage was restricted to below 0.8 V, such that only the Sn phase was active during cycling.[272] However, this method results in a large irreversible capacity due to the Li trapped in the Li_3Sb phase.

To calculate the impact of SnSb on full cell energy, the average delithiation voltage was estimated from the voltage curve of SnSb created by carbothermal reduction by Zhao et al.,[276] shown in Figure 40, to be 0.8 V. Using the theoretical capacity of SnSb, the results of a full cell model calculation are shown in Table 1, which shows a 10% improvement over graphite.

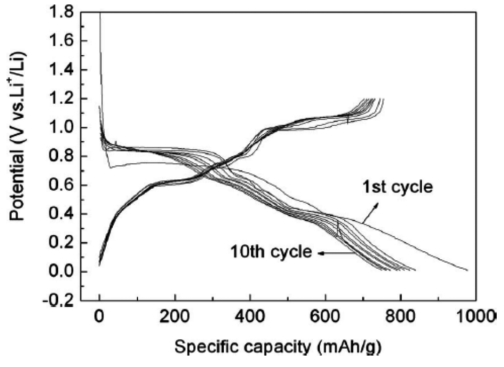


Figure 40. Voltage curve of SnSb synthesized by carbothermal reduction. Reproduced with permission from ref 532. Copyright 2006 The Electrochemical Society.

dx.doi.org/10.1021/cr500207g | *Chem. Rev.* 2014, 114, 11444−11502

3.7.1.2.8. Sn−Bi. Sn and Bi are immiscible and do not form ternary compounds with lithium. Accordingly, the electrochemistry of Sn−Bi alloys appears to be that of a simple mixture of Sn and Bi. However, Sn−Bi alloys are reported to have improved cycling characteristics as compared to pure Sn, which is thought to be due to a two-step lithiation mechanism.[274]

3.7.2. Active/Inactive Alloys. Active elements can be alloyed with inactive elements to modify voltage characteristics, grain structure, and reduce overall alloy volume expansion. When the active phase is present as nanometer-sized regions in an inactive matrix, two-phase regions are often avoided, resulting in improved cycling performance.[295] Interestingly, it has been found that the formation of $Li_{15}Si_4$ is suppressed in nanostructured (active Si)/inactive alloys, leading to improved cycling.[12,35] We speculate that the matrix phase in (active Si)/inactive alloys may play a similar role in suppressing the formation of $Li_{15}Si_4$ as does the substrate in Si thin films, which can suppress $Li_{15}Si_4$ formation via the generation of high mechanical stresses during volume expansion, as discussed in section 3.6.3.2. As will be discussed below, additions of an inactive phase can lead to higher energy densities at a given volume expansion. In some cases, the inactive element can also take part in lithiation reactions, forming ternary Li-active-inactive phases or undergoing displacement type reactions. This can significantly affect the voltage curve, cycling performance, and lithiation kinetics. As a motivation, the active/inactive alloy design strategy to maximize energy density is first discussed, followed by a discussion of the chemistry of Si and Sn based active/inactive alloys.

3.7.2.1. Active/Inactive Alloy Design. Active/inactive alloys can be classified into two types: those that comprise a completely active phase and a completely inactive phase (denoted here as Type I alloys), for example, an Si/$FeSi_2$ alloy, where $FeSi_2$ is completely inactive, and those alloys that lithiated via a displacement reaction (denoted here as Type II alloys), like Sn_2Fe or SnO_2. For simplicity, only Si-based Type I alloys will be considered in this discussion. The theory can be easily modified to include other active elements or Type II alloys by including the voltage depression and the additional volume expansion associated with the displacement reaction.[23]

The basics of active/inactive design are described in ref 23, in which an alloy "energy density" was used as a figure of merit. As discussed in section 2, this definition of energy density does not adequately weigh the voltage and volume considerations in a real cell. Therefore, the discussion is reformulated here in accordance with the cell model described in section 2. The basis for alloy design derives from the detrimental effects of volume expansion on cycling,[23] which are discussed in section 3.3. Generally, alloy cycle life becomes worse when volume expansion is increased. The maximum volume expansion tolerable will depend on the cell format, alloy particle size, binder, coating, and electrolyte formulation, as discussed in the relevant sections in this Review. With these considerations, an alloy should be designed so that cell energy is maximized at the volume expansion, which is designated to be tolerable during cycling.

To calculate cell energy in terms of volume expansion, some general expressions are needed that relate volume expansion to capacity and alloy composition. Fortunately, such expressions are simple because all Li alloys obey Vegard's law,[23] as shown in Figure 18. The volume expansion (ξ) of any lithiated Type I alloy is given by[23]

$$\xi = \frac{kx}{v_0} \times 100\% \tag{32}$$

This equation can also be written in terms of commonly measured quantities:

$$\xi = \frac{k\rho_{alloy}c_{alloy}}{F} \times 100\% \tag{33}$$

where k is the molar volume of lithium in alloys (~9 mL/mol), ρ_{alloy} is the density of the unlithiated alloy in g/mL, c_{alloy} is the alloy specific capacity in Ah/g, and F is the Faraday constant ($F \approx$ 26.802 Ah/mol). Thus, only the density and specific capacity of an alloy are needed to determine its volume expansion during cycling. The composition by volume of an active/inactive alloy at a given volume expansion at full lithiation, ξ_f, is also easy to calculate:[23]

$$\%\text{volume active component in alloy} = \frac{\xi_f}{\xi_o} \times 100\% \tag{34}$$

where ξ_o is the expansion of the active portion of the alloy at full lithiation. This can also be written in terms of easily measured quantities:

$$\%\text{volume active component in alloy} = \frac{\rho_{alloy}c_{alloy}}{\rho_{active}c_{active}} \times 100\% \tag{35}$$

For the purposes of this discussion, it will be assumed that the maximum tolerable volume expansion is 100%. Using the above equations, it is easy to show that an active/inactive Si alloy with 100% volume expansion at full lithiation is comprised of 36% by volume active silicon and 64% by volume of an inactive component and will have a volumetric capacity of 1495 Ah/L. Because the inactive phase acts as a bystander during the lithiation of the active phase, it should not have an effect on the voltage curve. On the basis of this, the voltage curve of a 36/64 v/v Si/inactive alloy as a function of volume expansion is shown in Figure 41. Because the silicon phase is fully lithiated, the average voltage is simply the average voltage of Si or about 0.41 V, assuming the Si phase is amorphous.

Another method to limit the volume expansion of a-Si is simply to restrict its capacity during lithiation. The voltage curve of a-Si is also shown in Figure 41. As illustrated in the figure, a pure a-Si particle will have the same volumetric capacity when restricted to cycle to the same volume expansion as a Si/inactive alloy. However, while the Si/inactive alloy is cycled over the entire voltage range of the active Si phase to achieve 100% volume expansion, pure a-Si must be limited to cycle only at the top of its voltage curve. Therefore, the average voltage of pure a-Si is much higher than the Si/inactive alloy. For this reason, the energy density of a Si/inactive alloy is higher than that of pure a-Si, when cycled to the same volume expansion.[23] Therefore, adding an inactive phase has increased the energy density. In addition to having a lower energy density, limiting the voltage of a pure a-Si electrode may not be practical, because high density alloy electrodes are likely to be blended with graphite, as discussed in section 7.2. In such electrodes, the alloy phase must be cycled to low voltages, so that the graphite is active.

The energy density of a cell stack and an 18650 cell using a Si/inactive alloy anode is shown in Figure 42. The volume percent active Si in the alloy is indicated in the figure. Also shown are energies for cells having a pure a-Si anode. For the reasons discussed above, the cell energy is significantly higher at a given

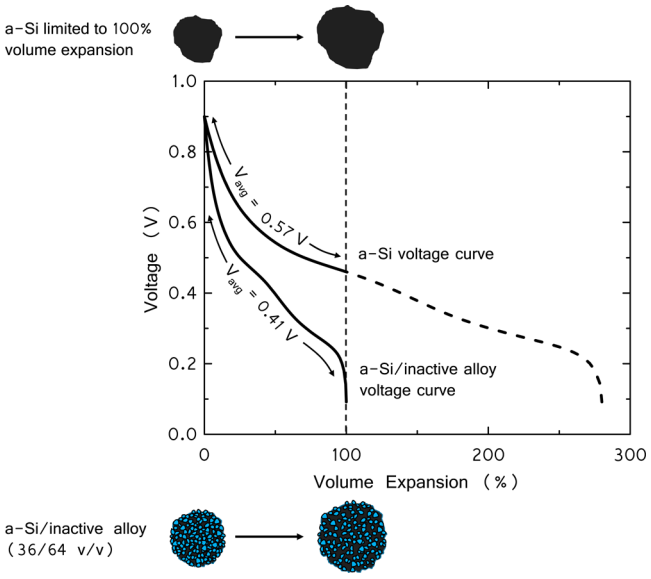


Figure 41. Voltage curve of a-Si that is cycled such that its volume expansion is restricted to 100% (the remainder of the a-Si voltage curve is shown as a dashed line), as compared to the voltage curve of a 36/64 v/v a-Si/inactive alloy cycled over its entire voltage range.

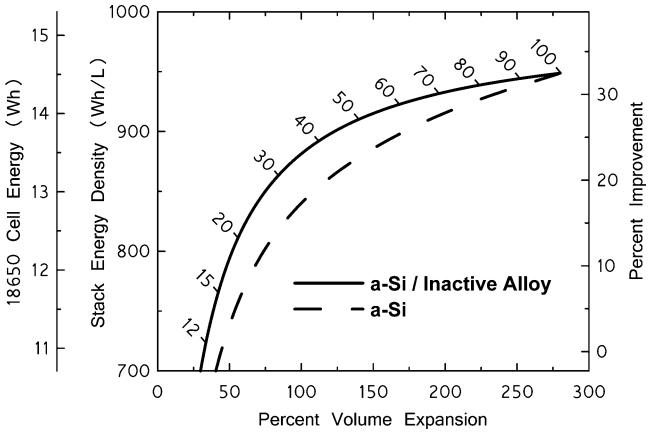


Figure 42. Modeled stack energy density and 18650 cell energy for a-Si/inactive alloys and a pure a-Si alloy as a function of volume expansion. The volume percent Si in the a-Si/inactive alloys is indicated at points along the a-Si/inactive alloy curve.

volume expansion when an inactive phase is present. The cell energy is increased dramatically as compared to a standard graphite cell when Si/inactive alloys with up to 140% volume expansion at full lithiation are used, corresponding to 50 vol % active Si in the alloy. At higher Si content and volume expansion, the gains are only slight. For instance, fully lithiated pure Si has double the volume expansion as compared to a 50/50 v/v Si/inactive alloy, but only results in a 4% improvement in cell energy. Alloy anode researchers should consider if the use of pure active elements (and their associated massive volume expansion) is justified for such small increases in energy over active/inactive phases.

3.7.2.2. Si−(Inactive Metal) Alloys. Si reacts with inactive metals to form silicides. Theoretically, such silicides are active with lithium via displacement-type reactions,[152,296] and indeed they are reactive with lithium at elevated temperatures.[296] However, it was found that at room temperature $TiSi_2$ and VSi_2 are completely inactive with lithium, $FeSi_2$ and $CoSi_2$ have a low capacity (~60 mAh/g), and $NiSi_2$ has a higher capacity (~200 mAh/g).[63,297] The voltage curves of all of these silicides were noted to be similar, as shown in Figure 43. Therefore, it was

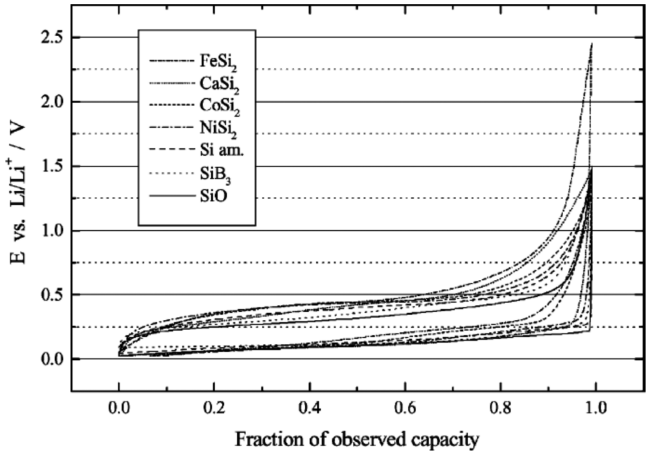


Figure 43. Voltage curves of various Si-alloys during their first delithiation and second lithiation. Reprinted with permission from ref 297. Copyright 2004 Elsevier.

theorized that the lithiation of $FeSi_2$, $CoSi_2$, and $NiSi_2$ results in the in situ formation of amorphous Si.[297,298] However, this is in contrast to the many results discussed below, which claim that transition metal silicides are inactive. In refs 63, 297, and 298, it is not mentioned where the silicides were obtained from and diffraction patterns are not shown. As an alternate explanation, we point out that because Si has a very high capacity, only small Si impurities can result in measurable reversible capacities. Because $TiSi_2$, VSi_2, $FeSi_2$, and $CoSi_2$ are all congruently melting, these silicides are expected to form with low Si impurity. The amount of Si impurity needed to result in the 60 mAh/g observed for $FeSi_2$ and $CoSi_2$ is only about 6 atomic %. On the other hand, $NiSi_2$ does not melt congruently and would be extremely difficult to make phase pure. Therefore, one would expect a higher Si impurity content for $NiSi_2$, leading to a higher observed capacity.

Subsequent studies have reported that (Cr + Ni)Si,[299] MnSi,[299] $FeSi_2$,[300−302] FeSi,[299] $CoSi_2$,[303] $NiSi_2$,[83,304,305] Ni_3Si_2,[306] Cu_3Si,[307] Cu_5Si,[308] and SiMm[309] (Mm = mischmetal) are all inactive toward lithiation. This is exemplified in Figures 44 and 45, which show the capacity of sputtered Si−M films as a function of the inactive metal, M, content. In the case of (Cr + Ni), Fe, and Mn, sputtering results in the formation of Si/SiM alloys.[299] The agreement with the predicted capacity based on the SiM phase being inactive is excellent. In the case of Si−Co, Si/$CoSi_2$ alloys are formed during sputtering.[303] The agreement with the predicted capacity based on $CoSi_2$ being inactive is also excellent.

In contrast to the above results, it has been reported that some silicides can have high reversible lithiation capacities. Wang et al. and Zhao et al. have reported reversible capacities of 1180 and 1220 mAh/g for NiSi made by ball milling and pulsed laser deposition, respectively.[310,311] Both explain this high capacity based on all of the silicon in NiSi being displaced during lithiation in a reversible reaction similar to

$$NiSi \xrightarrow{Li} Ni\,Li_{15}Si_4 \quad (36)$$

This reaction has a theoretical capacity of 1158 mAh/g, which is indeed close to the reversible capacities they report. Liu et al.

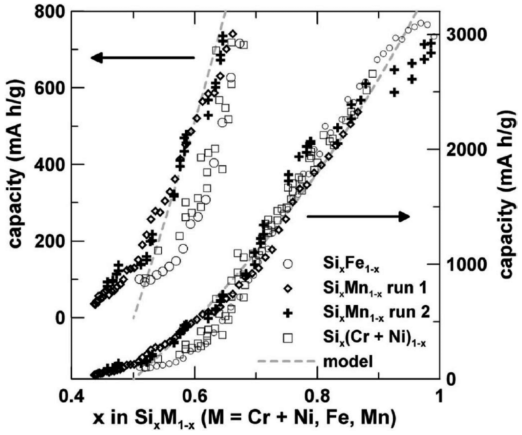


Figure 44. Capacity of sputtered Si_xM_{1-x} films as a function of x. The dashed line was calculated assuming Si_xM_{1-x} consists of $(2x - 1)Si + (1 - x)$ SiM, where the Si phase is active and the SiM phase is inactive. Reproduced with permission from ref 299. Copyright 2005 The Electrochemical Society.

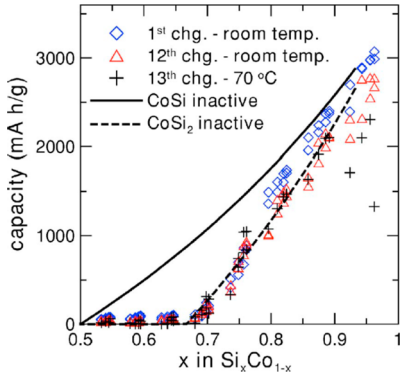


Figure 45. Delithiation capacity of sputtered Si_xCo_{1-x} films as a function of x. Solid and dashed lines indicate capacities calculated assuming full lithiation of the a-Si phase in coexisting regions of active Si and inactive CoSi, or $CoSi_2$, respectively. Reproduced with permission from ref 303. Copyright 2007 The Electrochemical Society.

synthesized Si/NiSi (1:1 atomic ratio) alloys by ball milling.[312] They determined by in situ synchrotron XRD that the NiSi reversibly lithiates according to

$$NiSi \xrightarrow{Li} Li_xNiSi;\ 0.3{-}1.0\ V \tag{37}$$

$$2Li_xNiSi \xrightarrow{Li} Li_ySi + Ni_2Si;\ <0.3\ V \tag{38}$$

Zhang et al. grew $Ni_3Si/Ni_{31}Si_{12}$ nanosheets from Ni substrates and observed 540 mAh/g capacity with no change in their XRD patterns during lithiation, suggesting intercalation.[313] Finally, Zhao et al. made a metastable $TiSi_2$ phase with a layered structure similar to graphite and reported that it could intercalate lithium with a reversible capacity of 943 mAh/g, forming Li_4TiSi_2.[314] However, we note in the latter case that their $TiSi_2$ contained a considerable amount of silicon oxide, which may impact reversible capacities. Nevertheless, there is considerable convincing evidence that under some circumstances Si−(inactive metal) phases may be active with high reversible capacities.

3.7.2.3. Si−B. Netz et al. reported that lithium could be inserted into SiB_3 with an initial insertion capacity of 922 mAh/g, but with substantial irreversible capacity.[298] The voltage curve of SiB_3 is shown in Figure 43. Because of its similarity with the voltage curve of amorphous Si, Netz et al. concluded that the first lithiation of SiB_3 involves the formation of amorphous Si. This is a similar mechanism that they suggest for the lithiation iron, cobalt, and nickel disilicides, which is discussed in the previous section. As mentioned in that section, we are skeptical regarding this mechanism, and this is also true in the case of SiB_3. As with the other silicides, a Si impurity in the SiB_3 sample of Netz et al. could well explain their observed electrochemistry. Although Netz et al. mention that SiB_3 is unstable above 1270 °C, it has been shown in other studies that it is metastable and decomposes into Si and SiB_6 at much lower temperatures.[315] There is no mention in the study by Netz et al. of where the SiB_3 was obtained from, and diffraction patterns are not shown. Confirmation of their results is needed.

Rousselot et al. prepared Si−B alloys with up to 14.3 atomic % B by ball milling.[316] They observed no difference in capacity or rate performance as compared to pure Si. We note that if boron is all inactive in $Si_{85.7}B_{14.3}$, then the capacity of this alloy would be 3362 mAh/g. This is only about 200 mAh/g lower than that of pure Si, which is within the stated error of Rousselot et al. Therefore, it is inconclusive if the B in this alloy is active or not. Rousselot et al. reasoned that the increased electrical conductivity induced by B-doping Si did not improve its performance, because the lithiation of Si also increases its electrical conductivity. Instead, they noted that improvements in coating formulation have a much greater effect than improving the electrical conductivity of Si.

3.7.2.4. SiO. SiO-based anode materials have evolved to have impressive performance and are currently under intense research for potential development in commercial cells. SiO materials are discussed in detail in section 7.3.2.

3.7.2.5. Other Silicon−Inactive Alloys. Kim et al. have made Si/TiN and Si/TiB_2 composites by ball milling.[317,318] Such composites were reported to be made up of nano-Si and TiN or TiB_2 finely dispersed in agglomerate particles. Increasing the fraction of the inactive phase resulted in a decreased capacity, but markedly improved cycling performance. Lee et al. investigated $Si/Li_2O_2/Al_2O_3$ composites made by reactive ball milling dispersed in graphite.[319] The addition of Li_2O_2 was found to be beneficial to the electrochemical properties. It was thought that the formation of Si/oxide composites by reactive ball milling results in finely dispersed Si and good cycling performance.

3.7.2.6. Sn−(Inactive Metal) Alloys. Thermodynamically, Sn−M alloys (M = a transition metal or a rare earth) are expected to form lithiated tin and metal M upon full lithiation:

$$Sn{-}M \xrightarrow{Li} Li_{4.4}Sn + M \tag{39}$$

However, depending on the metal M, stoichiometry, and alloy morphology, this reaction can be kinetically hindered or even completely prevented. Todd et al. investigated the lithiation of combinatorially sputtered Sn−M alloy films for M = Ti, V, Cr, Mn, Fe, Co, Ni, and Cu.[320] Sn alloys with Ti, V, Cr, and Co had composition regions in which the sputtered alloy was amorphous, while the other Sn−M alloys were crystalline in their entire composition range. Figure 46 shows the first delithiation capacities of all of the Sn−M alloys studied by Todd et al. The results generally agree with Sn−M alloys made by different methods.[321−336] Ti, V, Cr, and Co alloys showed featureless voltage curves when cycled in their amorphous range. The voltage curves remained featureless after many cycles for Ti, V, and Cr. Therefore, it was reasoned that no aggregation of Sn occurs during cycling and no expulsion of the transition metal

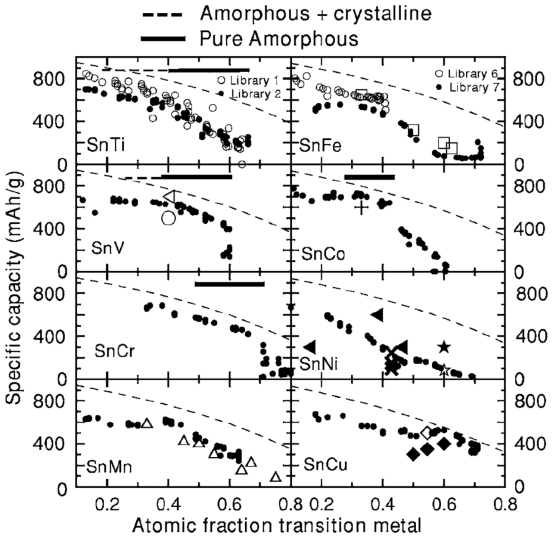


Figure 46. Specific first delithiation capacity of sputtered $Sn_{1-x}M_x$ alloys as a function of x for different transition metals, M, by Todd et al.[320] The dashed lines give the specific capacity that would be obtained if all of the Sn atoms could react with 4.4 Li atoms per Sn atom and the M atoms were inert. The results are compared to Sn−M alloys from other studies that have been prepared by different methods: (left-pointing △) from ref 327, (○) from ref 328, (Δ) from ref 329, (□) from ref 323, (+) from ref 330, (left-pointing ▲) from ref 331, (×) from ref 332, (☆) from ref 333, (★) from ref 334, (◇) from ref 335, and (◆) from ref 336. Reproduced with permission from ref 320. Copyright 2006 The Electrochemical Society.

occurs during lithiation for these metals. Such amorphous alloys with no Sn aggregation during cycling had the best cycling characteristics. Sn−Ti, V, and Cr alloys also showed near theoretical capacities over the entire alloy composition range, indicating that Li can penetrate in these amorphous alloys without difficulty. The amorphous region of Sn−Co alloys has low Co content and resulted in Sn aggregation during cycling and reduced capacity.

As shown in Figure 46, Sn−M alloys with M = Co, Fe, and Mn all have lower than expected capacities at high M content. It was hypothesized that the displacement of metal M during the lithiation of these Sn−M alloys causes a metal "skin" to form on the alloy surface, passivating the alloy from further reaction.[320,323,337] At higher Sn concentrations, the capacity is near the theoretical prediction for a full displacement reaction with lithium. It has been speculated that the open framework of the $FeSn_2$ and $MnSn_2$ structures aids lithium insertion.[323,329] However, this structural explanation of why these alloys are active is difficult to reconcile with the fact that Ti, V, Cr alloys can reach their theoretical capacities throughout their entire composition range even though they are fully amorphous, as discussed above.

According to Figure 46, Cu−Sn alloys nearly reach their full theoretical capacities for the entire composition range studied by Todd et al. Such alloys have been well studied. During lithiation, Cu_6Sn_5 has been shown to reversibly form an intermediate Li_2CuSn phase prior to Cu displacement from the alloy.[324,338] Restricting the voltage range above 200 mV such that the Cu displacement does not take place results in improved cycling.[324,325] Cu_3Sn is inactive at room temperature.[326,339] Interestingly, Kwon et al. have shown that Cu_3Sn can be thermally activated by electrochemical lithiation at 120 °C, which results in the formation of Cu and lithiated Sn. During delithiation at room temperature, Cu_6Sn_5 is formed, which can then cycle reversibly.[339]

In Figure 46, the capacity of sputtered Sn−Ni alloys is low for all compositions.[320] There is also much scatter in the capacity of Sn−Ni alloys prepared by other methods. Lee et al. found that ball milled Ni_3Sn_4 had low capacities (~200 mAh/g), which became lower if the alloy was annealed. They concluded that lithiation only occurred within the alloy grain boundaries.[332] Higher capacities have been achieved in porous and nanocrystalline Sn−Ni alloys.[334,340] Apparently the lithiation kinetics are slow in Sn−Ni alloys, and the reversible capacity is highly dependent on alloy morphology.

Sakaguchi et al. and Vaughey et al. studied the lithiation of $CeSn_3$ and $LaSn_3$, respectively.[8,341] These alloys have a theoretical capacity of about 713 mAh/g, but only have about 250 mAh/g reversible capacity. Vaughey et al. showed that the lithiation of $LaSn_3$ results in the formation of inactive La_3Sn_5 and lithiated Sn.[8] Vaughey et al. also states that the observed capacity of 250 mAh/g "is too low to compete significantly with standard graphite electrodes of state-of-the-art lithium-ion batteries." In our cell model, a 70% active volume $LaSn_3$ would result in about the same energy density as graphite because of its high volumetric energy density (1114 Ah/L) and reasonably low average voltage (~0.6 V). This is another good example of how the use of gravimetric capacities can be misleading.

3.7.2.7. Tin Oxide-Based Electrodes. Tin oxide-based electrodes include simple binary Sn−oxides, such as SnO or SnO_2. Complex oxides that include transition metals, alkali metals, glass formers such as B, P, Li, Al, Si, or other active elements including Sb, Bi, or In and Sn hydroxides have been studied to improve cycling performance and reduce irreversible capacity. Composites of these materials with carbon nanotubes, graphite, and carbon coatings, etc., have also been made, to increase performance further. For a detailed description of these materials, readers are directed to a recent and outstanding review by Reddy et al., in which Sn−oxide-based electrodes and oxide electrodes in general are exquisitely described.[342] However, we have not found a study or review in which the volumetric capacity or volume expansion of Sn−oxides is described or what impact Sn−oxide-based electrodes will have on cell energy; therefore, we shall attempt to do this here for some simple, but representative examples.

The lithiation and delithiation of SnO and SnO_2 proceeds stepwise according to the reactions:[93,342]

$$\text{step 1: } SnO_n \xrightarrow{Li} n Li_2O + Sn \text{ (irreversible)} \quad (40)$$

$$\text{step 2: } n Li_2O + Sn \xrightarrow{Li} n Li_2O + Li_{4.4}Sn \text{ (reversible)} \quad (41)$$

Figure 47 shows the voltage curve of SnO, which is typical of Sn−oxide-based anodes. Initially the lithiation of SnO proceeds via reaction 40, irreversibly consuming 2 equivalent units of Li and forming an active/inactive composite of n-Sn within a Li_2O matrix.[93] This reaction is responsible for the typically high irreversible capacity of Sn−oxide-based materials. Although the reverse reaction of eq 40 can be somewhat made to occur at high voltages, accessing the reverse reaction typically leads to capacity fade.[93,342] Subsequent to reaction 40, the thus formed composite can be reversibly cycled, according to reaction 41.

Figure 48 shows the differential capacity of a SnO:0.1-B_2O_3:0.1P_2O_5 glass during cycling. As cycling progresses, sharp peaks form in the differential capacity curve, which are indicative of the aggregation of Sn and are associated with poor cycling

dx.doi.org/10.1021/cr500207g | Chem. Rev. 2014, 114, 11444−11502

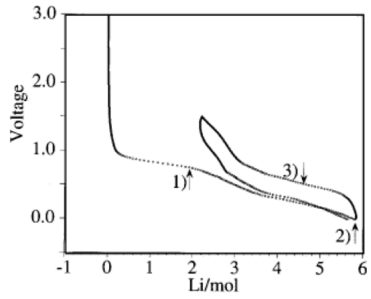


Figure 47. Voltage curve of a SnO electrode. Reproduced with permission from ref 533. Copyright 1999 The Electrochemical Society.

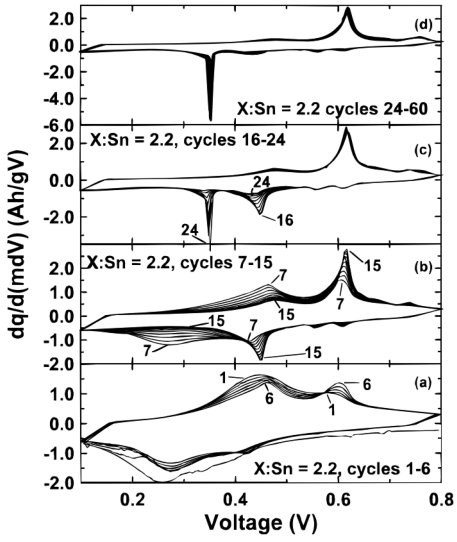


Figure 48. Differential capacity versus voltage of SnO:0.1B_2O_3:0.1P_2O_5 cycled between 0.1 and 0.8 V, showing the progressive aggregation and crystallization of Sn regions: (a) cycles 1−6, (b) cycles 7−15, (c) cycles 16−24, and (d) cycles 24−60. Adapted with permission from ref 295. Copyright 1999 The Electrochemical Society.

characteristics.[295] Sn aggregation in Sn−oxide materials has been observed by Mössbauer diffraction and directly by TEM,[343] as shown in Figure 49. Sn aggregation can be prevented by limiting voltage limits during cycling or increasing the proportion of inactive oxide.[295]

The original studies by Fujifilm Celltech still show some of the best cycling performance for Sn−oxide materials. Idota et al. demonstrated excellent cycling of a $Sn_{1.0}B_{0.56}P_{0.40}Al_{0.42}O_{3.6}$ glass (named TCO-1).[9] Such an oxide has been shown to be a mixture of active SnO and spectator B_2O_3, P_2O_5, and Al_2O_3 phases.[295,344] The voltage curve of TCO-1 is shown in Figure 50a, and its cycling performance in a full cell is shown in Figure 50b. Superior cycling performance was demonstrated as compared to SnO, which is likely due to the presence of the spectator phases that impede Sn-aggregation. Idota et al. estimated the volumetric capacity of TCO-1 as simply the product of its density (3.70 g/mL) and reversible capacity (600 mAh/g), resulting in a value of about 2200 Ah/L.[9] This has been cited many times. However, because volume expansion is not taken into account in this estimation, it cannot be correct, as will be demonstrated below.

The molar volume, volume expansion, and fully lithiated volumetric capacity associated with reactions 40 and 42 for SnO, SnO_2, and TCO-1 were calculated using the bulk crystal densities for Sn (7.3 g/mL), SnO (6.45 g/mL), SnO_2 (6.95 g/mL), B_2O_3 (2.46 g/mL), P_2O_5 (2.39 g/mL), Al_2O_3 (3.95 g/mL), and Li_2O (2.02 g/mL). These values are listed in Table 6. For SnO, the first displacement step of reaction 40 results in a 49% increase in volume, corresponding to the formation of one formula unit of Li_2O. In the case of SnO_2, two formula units of Li_2O are formed

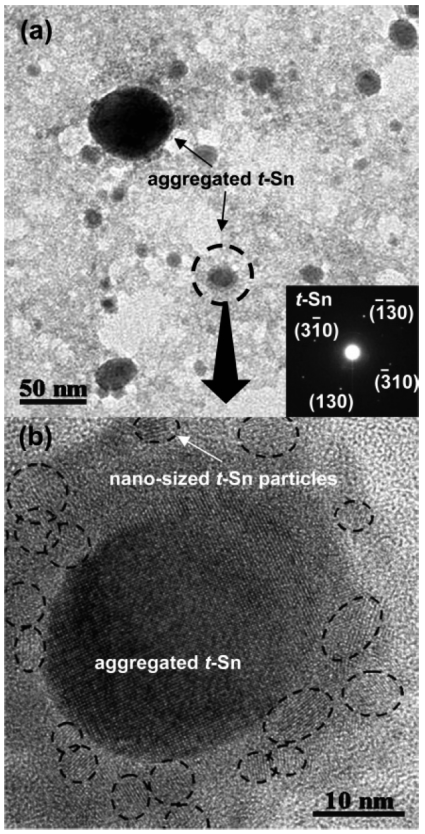


Figure 49. (a) High-resolution TEM image of ∼8 nm-sized SnO_2 nanocrystals after 30 cycles. Aggregation into larger clusters is shown. The inset image is a SAD pattern along the [001] zone axis showing tetragonal Sn. (b) Magnified image of the circled region in (a). A few nanosized Sn nanoparticles aggregate into the larger Sn clusters, to minimize the surface energy among the particles. Reprinted with permission from ref 343. Copyright 2005 American Chemical Society.

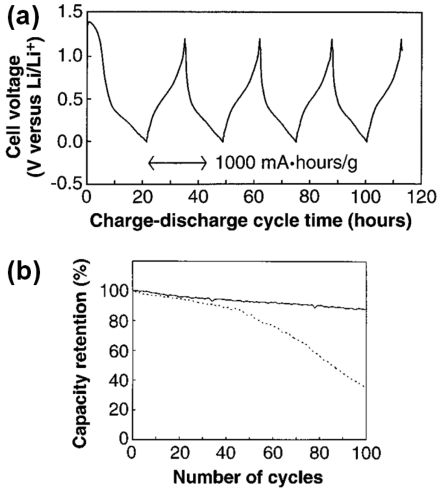


Figure 50. (a) Voltage curve of $Sn_{1.0}B_{0.56}P_{0.40}Al_{0.42}O_{3.6}$ in a lithium half-cell. (b) Cycling performance of a $LiCoO_2/Sn_{1.0}B_{0.56}P_{0.40}Al_{0.42}O_{3.6}$ cell (solid line) and a $LiCoO_2$/SnO cell (dashed line). Reprinted with permission from ref 9. Copyright 1997 AAAS.

Table 6. Molar Volume and Volume Expansion That Occur during the Lithiation of SnO, SnO_2, and TCO-1 ($Sn_{1.0}B_{0.56}P_{0.40}Al_{0.42}O_{3.6}$), Based on Bulk Crystal Densities and According to Reactions 40 and 41[a]

species	molar volume (mL/mol Sn)	expansion with respect to original oxide (%)	reversible expansion during cycling (%)	capacity (Ah/L)
SnO	21.0			
step 1	31.0	49		
step 2	70.6	238	128	1670
SnO_2	21.7			
step 1	45.8	111		
step 2	85.4	293	86	1380
TCO-1	46.4			
step 1	55.9	21		
step 2	95.3	73	70	1230

[a]The volumetric capacity is given for the fully lithiated species.

during the initial displacement reaction, resulting in a large expansion of 111%. The overall expansions of both SnO and SnO_2 are quite large, being 238% and 293%, respectively.

In contrast to SnO and SnO_2, the theoretical volume expansion during the initial displacement reaction and overall volume expansion are much smaller for TCO-1, being only 21% and 73%, respectively, as shown in Table 6. This is because of the presence of inactive spectator phases, which effectively dilute the expansion. In addition, the reversible expansion during reaction 41 becomes progressively smaller as the volume of the inactive matrix phase increases. We suspect that TCO-1 cycles well not only because of suppressed Sn-aggregation, but also because of significantly reduced overall volume expansion, as compared to SnO and SnO_2. Of course, as the volume of spectator phases increases, the volumetric capacity decreases. The volumetric capacity of TCO-1 as calculated from bulk crystalline densities is about 1230 Ah/L. Because crystalline phases are generally denser than amorphous phases, the actual volumetric capacity of TCO-1 is probably less than this. This is much smaller than the value of 2200 Ah/L calculated by Idota et al.,[9] as expected.

Using the volumetric capacity values listed in Table 6, the theoretical cell stack energies based on our cell model for SnO, SnO_2, and TCO-1 anodes were calculated assuming zero cell irreversible capacity. The theoretical cell stack energies calculated this way are 843, 804, and 778 Wh/L, respectively, representing a 16%, 11%, or 7% improvement over graphite. SnO has a decent energy improvement over graphite, but it generally does not cycle well.[342] SnO_2 cycles well, but generally only when methods that reduce it volumetric capacity further are employed (e.g., poorly packed nanoparticles or porous nanocomposites).[342] Even in the case where zero cell irreversible capacity is assumed, the 7% gain in energy provided by TCO-1 may not be worth the sacrifice of cycle life as compared to graphite. When the high irreversible capacities of these materials are included in cell energy calculations, they all result in theoretical cell energies that are well below that of graphite. We suspect this is another reason why the commercialization of such materials was not pursued.

We have not attempted to calculate the cell energies of the many composite and nano Sn−oxides that have been published, because there is insufficient information to do so (i.e., particle and packing densities). On the basis of the results above, it is imperative for researchers in this field to make such calculations.

4. BINDERS, SURFACE COATINGS, AND ELECTROLYTES

The influence of binders and electrolytes on the advancement of alloy anodes and the understanding of alloy chemistry cannot be understated. Figure 51 shows a voltage curve measured in 1995

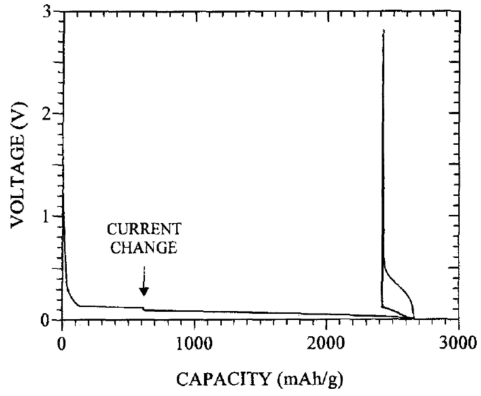


Figure 51. Silicon voltage curve measured in 1995 using a PVDF binder. Reproduced with permission from ref 154. Copyright 1995 The Electrochemical Society.

of Si particles in a PVDF binder with 1 M $LiN(CF_3SO_2)_2$ in a 50/50 v/v mixture of propylene carbonate and ethylene carbonate electrolyte. This voltage curve is typical of the electrochemical performance obtained prior to the development of more advanced binder/electrolyte chemistries that will be reviewed in this section. Considering the performance shown in Figure 51, it is of little wonder that the electrochemistry of Si was not well understood in the 1990s.

4.1. Binders

Coatings usually can be fully lithiated during the initial half-cycle, even when poor binders are used. As lithiation proceeds the particles expand and remain in good contact. However, unless a binder with good adhesion to the alloy particles is used, the alloy particles in a coating can become disconnected during delithiation as they contract. This is exemplified in Figure 51, which shows the voltage curve of Si cycling in a conventional PVDF binder. The full lithiation capacity is achieved, but almost no delithiation capacity is observed. In addition, SEI growth can insulate alloy particles and cause them to be disconnected.[103] The failure mechanisms that occur when conventional binders are used in alloy coatings are now fairly clear. In conventional PVDF coatings coated from NMP slurries, the PVDF forms a thin net of fine (<30 nm) polymer threads.[345] This leaves much of the alloy surface exposed to electrolyte and leads to significant SEI growth during cycling.[103] The electrolyte decomposition products increase electrode impedance and cause some alloy particles to become isolated.[102,103] In addition, PVDF does not chemically bond to the alloy particles or current collector and experiences severe swelling when exposed to electrolyte. This compromises the mechanical integrity of the electrode.[103] During cycling the mechanical integrity of the electrode is compromised further by alloy expansion, and alloy particles can easily become disconnected. These effects are illustrated graphically in Figure 52a. When combined they lead to severe capacity fade.

Binder research has reached a fairly unanimous solution to these failure mechanisms. It is generally recognized that good binders should have the following properties:

dx.doi.org/10.1021/cr500207g | Chem. Rev. 2014, 114, 11444−11502

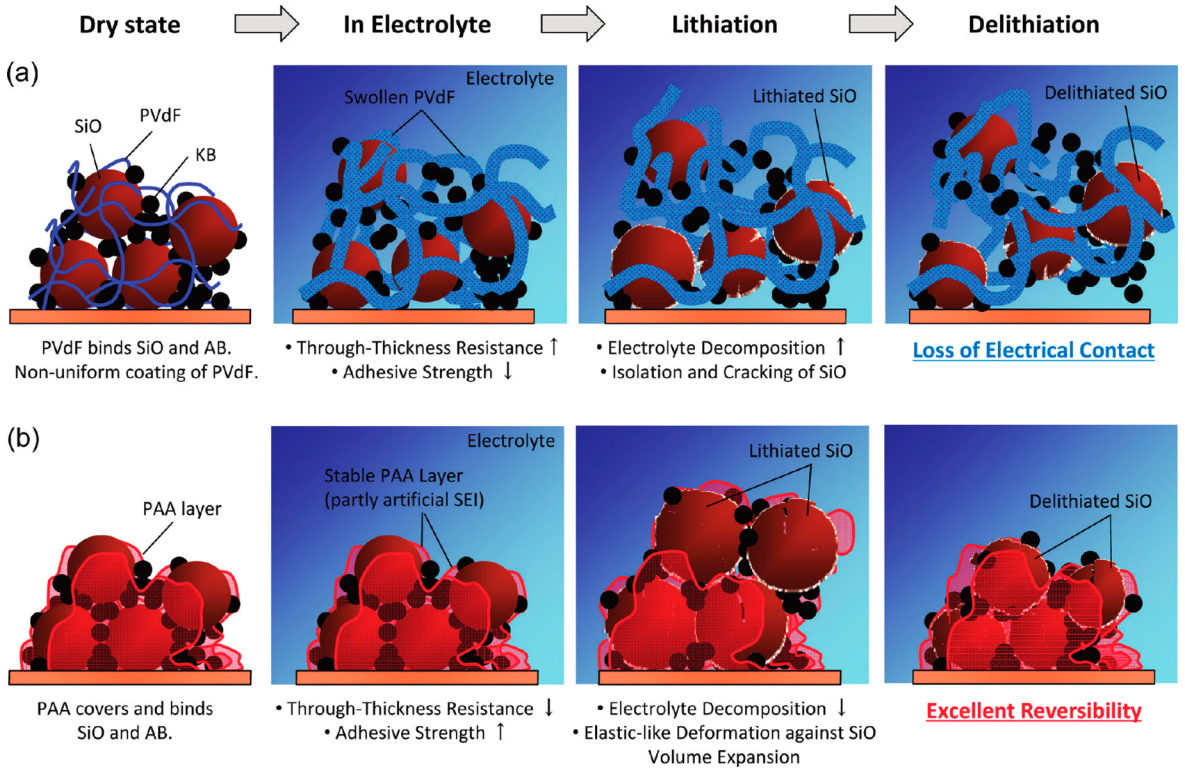


Figure 52. Mechanism proposed by Komaba et al. to explain superior cycling of SiO in PAA binder as compared to PVDF. (a) SiO coating with PVDF binder showing PVDF swelling upon exposure to electrolyte and poor adhesion. (b) SiO coating with PAA binder, showing no swelling, the formation of an artificial SEI layer, and strong binder adhesion. Reprinted with permission from ref 357. Copyright 2011 American Chemical Society.

- good adhesion to alloy particles and to the current collector
- ability to entirely coat the surface of alloy particles to inhibit SEI formation, while facilitating Li^+ ion conduction
- ability to tolerate volume expansion by stretching or self-healing

In addition to the above, a good electrically conductive network must be maintained. When only part of these requirements are met, only partial improvement results. For instance, Li et al. found that PVDF forms a continuous coating on alloy surfaces in electrodes that were heated above the PVDF melting point, resulting in improved cycling, as shown in Figure 53.[346] All coatings were able to achieve the prescribed 2000 mAh/g initial lithiation, but the delithiation capacity increased monotonically in the following voltage limited cycling as the quality of the PVDF coating on the alloy particles improved.

A number of approaches to attain binders with the above properties have been made. In general, binders that have the above listed properties result in good cycling performance, regardless of the binder chemistry, including cross-linked fluoroelastomer binders that incorporated a silane adhesion promoter,[267] and polyacrylonitrile.[347] Choi et al. and Kim et al. have shown particularly excellent cycling performance for micrometer-sized silicon particles at 100% depth of discharge in electrochemically active polyimide binders.[348,349] Most recent studies however have focused on water-based binders based on poly(carboxylic acid)s and their alkali metal salts, including carboxymethyl cellulose (CMC),[177,350−354] poly(acrylic acid) (PAA),[103,355−357] and alginate.[358]

The native surface of silicon is made up of silicon oxide (Si−O−Si) and silanol (Si−OH).[221,352,359] Poly(carboxylic acid) binders have been shown to bond to silicon surfaces with either strong ester-like covalent bonds or weaker hydrogen bonds, depending on the pH of the coating slurry.[177,352,353] The solution pH can also alter the configuration of the polymer to enhance binding with the alloy surface.[354] Although the hydrogen bonds formed between poly(carboxylic acid)s and alloy surfaces are fairly weak, they are believed to have self-healing properties,[353] as illustrated in Figure 54. Considering that the native oxide on Si is believed to be significantly changed during cycling,[221,359−361] this self-healing concept may have a lot of merit.

It has been somewhat of a mystery how poly(carboxylic acid)s, which are generally brittle, can withstand the large volume expansions encountered during cycling. In this regard, Lestriez et al. pointed out that "the mechanical properties of a polymer in the bulk can be much different than the mechanical properties of a bundle of a few chains of the same polymer. For example, gelatin is a stiff polymer, however a few chains of gelatin have been shown to be able to extend over extraordinary large surface-to-surface distances up to five times their full stretched length."[351] Furthermore, hydrogen bonding is thought to induce cross-linking in poly(carboxylic acid)s, improving their mechanical properties.[357] Recently, Cerbelaud et al. showed by simulations that CMC binders tend to aggregate in particle−particle contact sites and suggested that such polymer aggregations may act like springs between the alloy particles.[354]

The cycling of poly(carboxylic acid) binders improves as the density of carboxylic acid groups increases.[352] Accordingly, much research has been devoted to PAA-based binders, which has a much greater carboxylic acid density than CMC and much improved cycling characteristics.[103,355−357] Figure 55 illustrates the marked increase in cycling performance in the order PVDF < CMC < PAA, which is generally found in most studies. Komaba et al. have shown that PAA-based binders do not swell in contact

dx.doi.org/10.1021/cr500207g | Chem. Rev. 2014, 114, 11444−11502

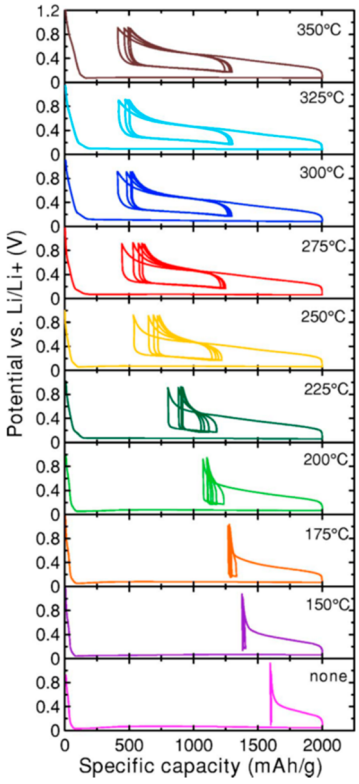


Figure 53. Potential versus specific capacity for five cycles of cells having Si electrodes with PVDF binder. These PVDF-based Si electrodes were heated at different temperatures as indicated for 12 h in Ar and then compared to the ones without heat-treatment. All cells were first discharged to 2000 mAh/g, followed by cycling at 150 mA/g between 0.17 and 0.9 V. Reproduced with permission from ref 346. Copyright 2008 The Electrochemical Society.

with electrolyte, maintain strong adhesion to alloy surfaces, and cover the alloy surface completely to form an artificial SEI and impede SEI growth.[103,357] The properties that lead to the excellent performance of PAA binders are graphically represented in Figure 52b.

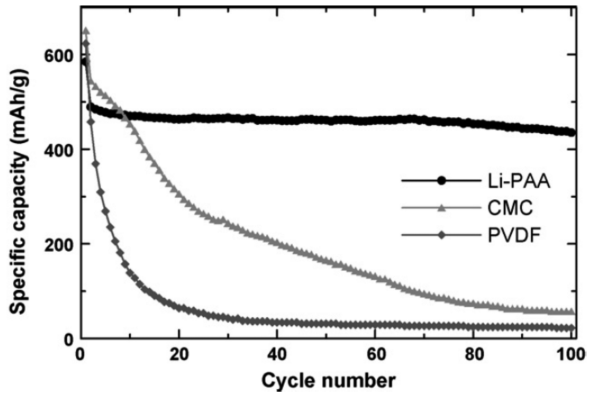


Figure 55. A comparison of the cycling performance of $Sn_{30}Co_{30}C_{40}$ electrodes using LiPAA, CMC, and PVDF binders. Reprinted with permission from ref 355. Copyright 2010 Elsevier.

Research in improving binder characteristics further is ongoing. Recently, Wang et al. demonstrated binders with enhanced self-healing properties that are able to withstand large volume expansion during cycling.[362] Koo et al. have reported that blending PAA and CMC forms a highly cross-linked binder that has superior performance as compared to the individual polymers.[363] The use of conducting polymer binders has also been of recent interest. Such binders were the focus of early alloy binder research. In the late 1980s, Jow et al. and Maxfield et al. showed that Li−Pb and Na−Pb alloys in poly(*p*-phenylene) binder could be cycled hundreds and even thousands of times with good capacity retention.[122,364] Wu et al.[365] and Xun et al.[123] have reinvestigated the use of conducting polymers with impressive results. In particular, Wu et al. reported achieving 5000 cycles at over 90% capacity retention for an electrode comprising a conductive polymer and Si nanoparticles.[365]

4.2. Surface Coatings

Surface coatings on alloy particles have been shown to enhance cycling performance. This is believed to be due to increased electrical conductivity and the formation of a more stable SEI layer. Such surface coatings include carbon,[233,264,319,366,367]

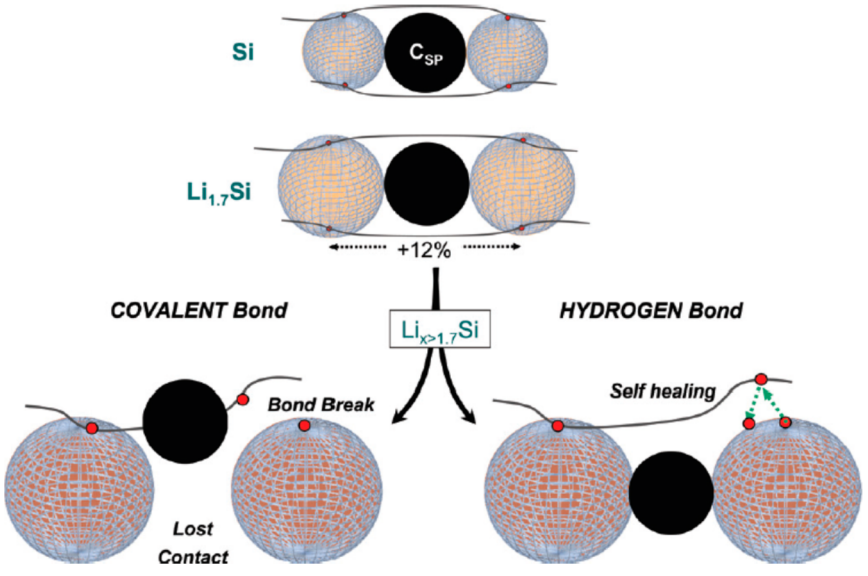


Figure 54. An illustration of how hydrogen bonds can respond to alloy expansion by detaching and then reattaching to the alloy particle ("self-healing"), while covalent bonds can break and cannot repair themselves. Reproduced with permission from ref 353. Copyright 2011 The Electrochemical Society.

dx.doi.org/10.1021/cr500207g | *Chem. Rev.* 2014, 114, 11444−11502

electroless metallic Cu and Ag coatings,[137,368−370] SiO_x,[371] TiO_2,[372] SnC_2O_4,[373] and $TiSi_2$.[374] The effect of coating electrodes can be quite profound. For instance, Yamada et al. have shown that uncoated SiO/graphite electrodes have extremely poor capacity retention and high irreversible capacity.[366] Performance is improved drastically after the electrode is carbon coated (as shown in Figure 81 in section 7.3.2).

4.3. Electrolytes and Additives

The cycling performance of alloys is highly dependent on electrolyte salts, solvents, and additives. It is generally believed that SEI formation can be more severe for alloys as compared to graphite, because continual alloy expansion and contraction during cycling can disrupt the SEI passivating film, leading to continual SEI growth.[21,102,375] In addition, the fracturing/pulverization of the alloy during cycling can create fresh surfaces onto which additional SEI is formed.[102,221,376] This may irreversibly trap lithium in the SEI or isolated fragments of the alloy, leading to capacity fade. For these reasons, alloys generally have poor cycling characteristics and low CE in conventional electrolytes comprising $LiPF_6$ and alkyl carbonates. The control of SEI chemistry and morphology is crucial to obtaining good cycling with alloy anodes.

4.3.1. Electrolytes for Silicon Alloys. The native surface of Si is made up of silicon oxide (Si−O−Si) and silanol (Si−OH).[221,352,359] Phillip et al. have reported that upon exposing the Si surface to electrolyte containing $LiPF_6$, the native silicon oxide reacts with HF (from the hydrolysis of $LiPF_6$) and is slowly replaced with SiO_xF_y.[361] HF may also react with Si to form SiF_6^{2-}, leading to the formation of cracks in the alloy.[377] During the first steps of lithiation, the native layer is believed to irreversibly react with lithium, organic solvents, or lithium salts,[221,359−361] and SEI formation commences. There exist conflicting reports as to the mechanism of SEI formation, its evolution during cycling, and its composition and the role of additives. However, it is generally recognized that additions of VC and especially FEC to conventional electrolytes can markedly improve cycling performance,[221,225,378−380] as is demonstrated in Figure 56.

In one mechanism of SEI formation, derived chiefly from the results of ex situ XPS experiments, the native oxide layer irreversibly reacts with lithium during the initial lithiation to form Li_xSiO_y[360,361] or, as reported by Lee et al., completely breaks down.[359] In $LiPF_6$ containing electrolytes containing no additives, the SEI may comprise fluorinated species on the electrode surface that are formed from the reduction of $LiPF_6$, such as LiF, LiP_xF_y, or $Li_xPO_yF_z$,[222,359,377,379,381−383] in addition to solvent decomposition products, including alkyl carbonates.[221,359,378,382] Such reactions irreversibly consume lithium,[224] and increased irreversible capacity has been shown to result when particle size is decreased (surface area increased).[376] These decomposition products are thought to form a porous or unstable SEI layer, resulting in continual SEI formation, capacity fade, and impedance growth.

The addition of FEC to conventional electrolytes containing $LiPF_6$ is generally believed to inhibit the decomposition of $LiPF_6$ or electrolyte solvent, resulting in a more stable and impervious SEI that is thinner and whose growth is significantly impeded as compared to electrolytes with no FEC. The composition of this stable SEI layer formed in the presence of FEC is has been reported to predominantly comprise LiF.[221,360,379] FEC has also been reported to polymerize to form passivating polyene

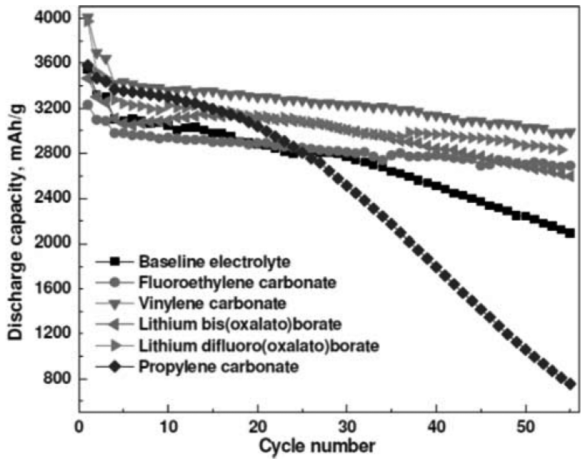


Figure 56. Cycling performance of thin film Si electrodes in 1.0 M $LiPF_6$ EC/DMC/DEC (1/1/1, vol %) (baseline electrolyte) with 3 wt % FEC, 5 wt % VC, 5 wt % LiBOB, or 1 wt % LiFOB electrolyte, as indicated in the figure. Also shown is the cycling performance of thin film Si electrodes in 1.0 M $LiPF_6$ PC/DMC/DEC (1/1/1, vol %) electrolyte. Reproduced with permission from ref 385. Copyright 2012 The Electrochemical Society.

compounds,[360,378] as shown in Figure 57. In an interesting study, Mazouzi et al. measured the thickness and weight of cycled

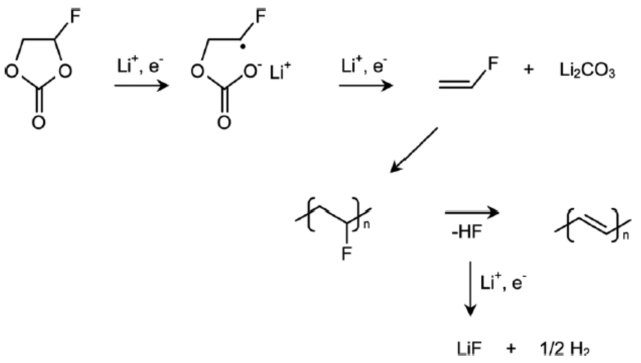


Figure 57. Proposed reaction scheme of FEC on a silicon anode surface, forming an SEI comprising lithium fluoride and a polyene-compound. Reproduced with permission from ref 378. Copyright 2011 The Electrochemical Society.

n-Si electrodes after cycling.[380] They found that both the electrode thickness and the weight are highly correlated to the capacity loss. The thickness, weight gain, and capacity loss could be greatly reduced when FEC and VC additives were present in the electrolyte, in conjunction with a good performance binder. Kajita et al. observed the SEI thickness growth on C-SiO electrodes directly using TEM cross-section images, shown in Figure 58.[384] A "heterogeneous layer" formed on the outside of the C−SiO particles during cycling and was comprised of decomposed Si−O and electrolyte solvent. This layer increased in thickness with increasing cell fade at 20 °C. Interestingly, at 60 °C the thickness of this layer did not depend on cell fade, suggesting a different mechanism for fade at higher temperatures.

Other studies have found essentially the complete opposite of the mechanism proposed above. Dalavi et al. found that 1.0 M $LiPF_6$ EC/DMC/DEC 1/1/1 v/v solutions resulted in passivating films with high LiF content (from $LiPF_6$ decomposition) and low concentrations of lithium alkyl carbonates and Li_2CO_3.[385] Additions of FEC resulted in a low LiF content (due

dx.doi.org/10.1021/cr500207g | Chem. Rev. 2014, 114, 11444−11502

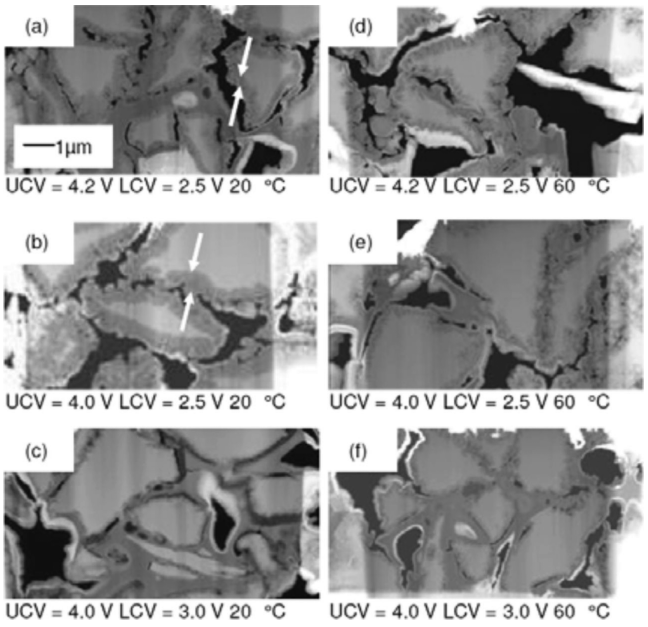


Figure 58. TEM dark field cross-section images of C-SiO particles taken from $LiNi_{0.8}Co_{0.15}Al_{0.05}O_2$/C-SiO full cells after 500 cycles with different upper and lower cutoff voltages (UCV and LCV) at 20 and 60 °C. The heterogeneous phase that was formed during cycling is indicated with white arrows. Reproduced with permission from ref 384. Copyright 2013 The Electrochemical Society.

to inhibited $LiPF_6$ decomposition) SEI that is rich in lithium alkyl carbonates, polycarbonates, and oxalates. They propose that these organic species can effectively passivate the alloy surface, while LiF cannot. In another variation, using ^7Li, ^{19}F, and ^{13}C NMR, Delpuech et al. found that SEI growth and irreversible capacity is not due to $LiPF_6$ decomposition.[386] Instead, they found that the SEI is mainly in the form of nonlithium containing oligomers or polymers that result from solvent decomposition. Finally, also in contrast to the mechanism proposed above, McArthur et al. measured the SEI thickness by in situ ellipsometry and found that it was thickest when FEC or VC additives were present.[387] Interestingly, they also found that the SEI thickness changes during cycling, becoming thinner during alloy delithiation and thicker during lithiation. McArthur et al. argue that the ex situ methods may damage the SEI, leading to erroneous results. Another explanation for differing results among authors may simply lie in the fact that the SEI is very dynamic and its composition and morphology are strongly dependent on cycling history and voltage, as has been shown by almost all of the above studies.

Besides FEC, other electrolyte additives that are film forming or otherwise avoid or inhibit $LiPF_6$ decomposition have been shown to significantly improve the cycling performance of Si, including VC,[225,380,385−388] LiBOB,[377,385] LiFOB,[385] LiFSI,[361] tris(pentafluorophenyl) borane,[389] succinic anhydride,[381] and silanes.[383,390] Electrolyte combinations are also now being explored for synergistic effects. For instance, Li et al. found that Si had superior cycling performance in electrolytes containing mixtures of $LiPF_6$ and LiBOB, as compared to electrolytes with a single salt.[391]

4.3.2. Electrolytes for Tin Alloys. As compared to Si, there are relatively few studies on electrolyte interactions with Sn electrodes. In air the native surface layer on Sn comprises SnO_2 or $SnO_2{\cdot}xH_2O$.[392,393] These species can be fully reduced during the initial steps of lithiation to form Li_2O and Sn.[89] This presents a situation different from that in the case of Si in which most studies consider the native oxide layer to be modified, but not completely reduced during lithiation.[221,359−361] Beattie et al. reported that clean Sn surfaces catalyze electrolyte reduction at about 1.5 V.[394] The reduction reaction was not self-passivating and was so severe that it impeded lithiation altogether. To avoid electrolyte reduction on Sn, Beattie et al. found that an initial current pulse applied to the Sn electrode resulted in a noncatalytic Li−Sn alloy to be formed on the Sn surface, after which lithiation could proceed. However, the severe catalytic electrolyte reduction resumed if the Sn was completely delithiated during cycling.

Baek et al. studied the chemistry of the SEI formed on Sn in 1 M $LiPF_6$ in EC:DMC (1:1) electrolyte.[395] Upon contact with the electrolyte and above 1 V vs Li, they found that the surface of Sn was covered by P and F containing species that remained stable during lithiation. Below 0.63 V an organic surface layer was formed that was subsequently destroyed below 0.1 V. The generation of such species was thought to be responsible for irreversible capacity during the cycling of Sn. Song et al. showed that the P and F containing species and the organic species accumulated on Sn surfaces during cycling between 0.1 and 1.0 V.[396] They concluded that these species were not effective for passivating the Sn surface during cycling.

As with Si, additives like VC and FEC have been found to have beneficial effects for Sn-based alloys. Bridel et al. showed that the catalytic electrolyte reduction on Sn surfaces can be eliminated if 10% VC is added to the electrolyte.[388] Smith et al. showed that the CE of $Sn_{30}Co_{30}C_{40}$ electrodes during cycling is significantly improved when FEC is added to the electrolyte.[397]

5. EVALUATION OF ALLOY CYCLING PERFORMANCE IN CELLS AND COATINGS

This section will focus primarily on methods for the evaluation of alloys in cells allowing prolonged cycling (coin, pouch, or cylindrical) as well as the evaluation of electrodes composed of composite particle coatings, as these correspond the most closely to what has and continues to be commercialized. Classical methods include cycling alloys at constant voltage limits and constant capacity limits, in half-cells, in symmetric cells, or in full cells, as well as EIS and dilatometry. Here, we also discuss more recent methods such as acoustic emission and in situ high precision calorimetry. By using a combination of these methods, a detailed picture of the failure mechanisms that occur during prolonged cycling can be obtained. Many other methods that will not be discussed in detail here have been used to characterize alloys and, while being extremely powerful, are either ex situ or require specialized cells for in situ operation that preclude long-term cycling. Some of these methods have already been discussed in this Review such as XRD (throughout section 3, and sections 7.3.1 and 7.3.3), NMR (sections 3.6.1.1 and 4.3.1, see also refs 9, 155, 177, 178, 360, 386, 398−401), XPS (section 4.3.1, see also refs 49, 186, 212, 357, 401−408), AFM (sections 3.3 and 3.6, also ref 404), optical microscopy (section 3.3), and Mössbauer spectroscopy (section 7.3.1 and throughout section 3). Electron microscopy is ubiquitous in the literature for studying the effect of cycling on alloys (section 3.3) or determining their microstructure (Figures 38, 49, 58, 83). Perhaps most exciting is the development of in situ TEM studies of the lithiation of alloys (section 3.6.1). Electron microscopy also features prominently in other recent reviews such as refs 13, 22, 170, 409. Other methods used to study lithiation mechanisms include

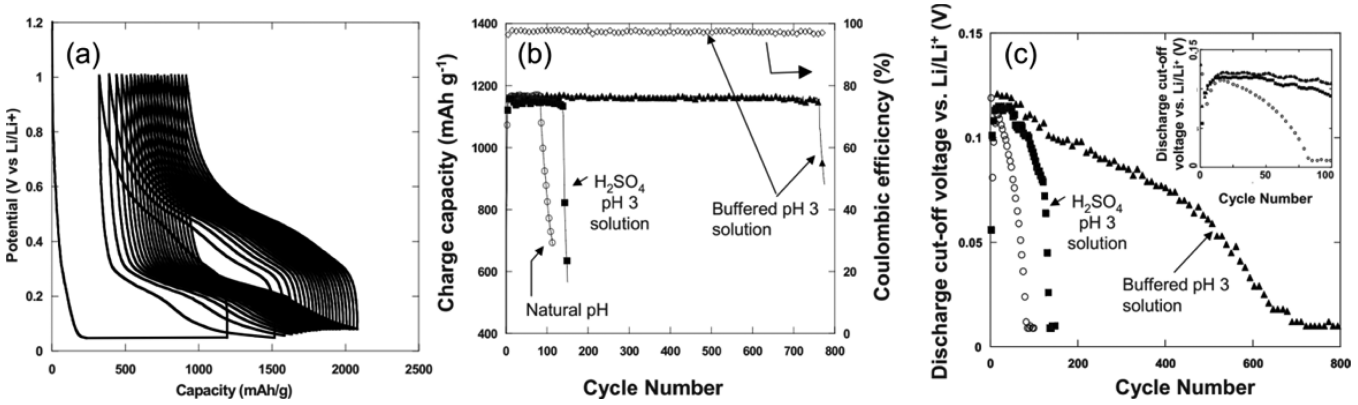


Figure 59. (a) Potential versus Li composition at C-rate for the first 20 cycles for a n-Si/CMC composite electrode prepared in buffered solution at pH 3. (b) Charge specific capacity and Coulombic efficiency and (c) potential at the end of discharge versus cycle number for electrodes prepared in (○) DI water, (■) aqueous H_2SO_4 pH 3 solution, and (▲) buffered solution at pH 3. Adapted with permission from ref 425. Copyright 2009 The Electrochemical Society.

Raman,[103,172,204,216,360,410−419] EELS,[18,412,419] TOF-SIMS,[378] tomography,[420] and ellipsometry.[387] These methods have been discussed in detail elsewhere. Readers are encouraged to consult the appropriate references for further information. Finally, alloy research would benefit from the application of methods recently developed in the Li-ion field such as in situ studies of 18650s using synchrotron X-ray diffraction[421] or in situ pair distribution function analysis of nanocrystalline electrode materials.[422]

5.1. Half-Cells

Half-cells are easy to build and understand, and are the natural first step in evaluating an alloy material. Half-cells are commonly constructed with a large excess of lithium and electrolyte as compared to full cells. Electrolyte levels are rarely mentioned in the literature; however, in our experience laboratory cells have ≥13 g/Ah of electrolyte, while commercial cells aimed at long life have 3−10 g/Ah of electrolyte, and high energy commercial cells have only <3 g/Ah. As a result, laboratory cells can potentially cycle much longer than full cells or symmetric cells, which have a limited amount of lithium or electrolyte or both. Although this artificially extends cycle life, it also effectively decouples intrinsic failure (i.e., particle fracture, particle disconnection) from other failure mechanisms related to electrolyte cosumption.

5.1.1. Half-Cell Cycling Using Constant Voltage Limits. Cycling alloy electrodes in half-cells at constant voltage limits is by far the most popular method to evaluate cycling performance. Typically such cells are held at constant voltage at the end of full alloy lithiation until a minimum current is reached. This simulates the constant current constant voltage (CCCV) charging protocol that is typically used in full cells. Because the amount of electrolyte and lithium is usually not limited in half-cells, as mentioned above, the capacity fade in half-cells cycled between fixed voltage limits can be directly linked to failure of the alloy, electrode coating, and SEI growth. Caution must be exercised during half-cell cycling for extended periods, because impedance growth at the lithium electrode may eventually induce fade or dendritic Li may cause internal shorts.[12] In addition, erroneous results may arise when the voltage limits are near the potential of a two-phase region. For example, cycling x-Si to voltages between 0−170 mV can result in the progressive lithiation of more x-Si during every cycle.[161]

As mentioned in section 4.1, capacity fade in an alloy coating usually occurs during delithiation as pulverization, binder failure, or network failure becomes more evident as the alloy particles contract. Figure 55 shows examples of alloy coatings cycled in half-cells exhibiting various degrees of binder failure. This type of failure typically manifests itself from the beginning of half-cell cycling and results in relatively linear capacity fade during the first few cycles. Buildup of SEI products can also cause fade.[103] In contrast to binder failure, impedance growth from SEI products over many cycles can result in capacity versus cycle number plots to have an inflection point, where impedance growth has caused the cutoff potential and alloy voltage plateau to coincide, resulting in increased fade. This is exemplified in Figure 56.

5.1.2. Half-Cell Cycling Using Constant Capacity Limits. Constant capacity cycling has been used extensively to evaluate alloy cycling performance. This method is especially used for Si electrodes, because limiting the capacity of Si using voltage limits is difficult.[161] It can be effectively used to compare the effects of different lithiation levels (or alloy volume expansion) on cycle life. A series of papers from the CNRS (French National Center for Scientific Research) has studied Si-based electrodes through limited capacity cycling, showing that increased Li loss due to SEI formation occurs as Si is cycled at higher capacities, and that SEI growth can be quantitatively measured through mass measurements.[178,380,386,423,424]

A typical capacity curve obtained from limited capacity cycling is shown in Figure 59.[425] As cycling progresses, more Si becomes disconnected during delithiation. Figure 60 shows an evaluation of various conductive additives and their impact on limited capacity cycling.[424] The combination of VGCF and MWCNTs is shown to give the best results as the VGCF accommodates volume changes at the micrometer scale in the electrode and the MWCNTs ensures electrical contact between the Si particles and the VGCF network. Figures 59b and 60 show that when all of the Si has become disconnected due to network failure, the capacity drops sharply to zero. The amount of Si loss can be tracked by monitoring the cutoff voltage during cycling, as shown in Figure 59c. Typically the number of cycles reached before this capacity drop is used as a figure of merit for alloy/coating performance. There are unfortunately many articles that provide neither voltage nor cycles to failure information, thereby rendering the exercise essentially useless. Even when this information is given, its relationship to full cell performance is a matter of debate. This is because during constant capacity cycling lithium is accumulated in the anode up to the point at which the capacity drops.[178] Figure 61a shows cumulative capacity loss in a limited-capacity cycled Si-based electrode. After 50 cycles the best

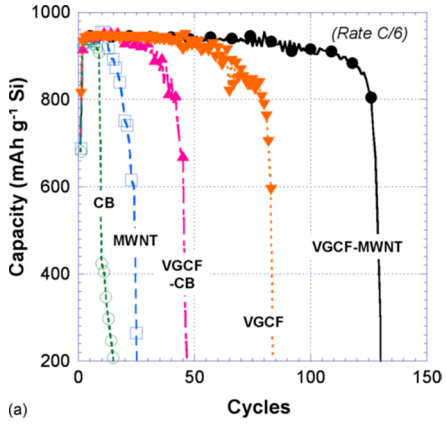


Figure 60. Constant discharge capacity versus cycle number for electrodes containing 80 wt % Si, 8 wt % CMC, and 12 wt % additive. Additives used were CB, MWNTs, 1:2 VGCF:CB, VGCF, and 1:2 VGCF:MWNT as noted in the figure. The rate is *C*/6, that is, 0.15 A/g. Upper voltage cutoff was fixed at 1 V. Adapted with permission from ref 424. Copyright 2009 The Electrochemical Society.

performing electrode has already slipped by more than the 1200 mAh/g cycled capacity. This mode of cycling would never occur in a full cell due to the limited amount of Li available in the cathode. Therefore, it is not entirely clear how this method would reflect alloy performance in a full cell.

5.1.3. Differential Capacity Analysis. Voltage plateaus are easily identifiable as sharp peaks in the differential capacity (d*Q*/d*V* vs *V*) of half-cells, the peak height indicating the flatness of the plateau, and its area a measure of the plateau's capacity. It can therefore be used to identify plateaus and their evolution during cycling and even identify Li ordering within a phase.[426] Lithiation in alloys can occur via two-phase reactions (indicated by a voltage plateau) or single phase reactions (sloping voltage), as detailed in section 3.4. Differential capacity analysis can be used to understand the phases being formed by alloys during lithiation (multiple examples throughout section 3.1). An important example is the identification of $Li_{15}Si_4$ formation during the cycling of Si, as detailed in section 3.6.2.2. In active/inactive alloys (section 3.7.2.1), the electrochemical behavior of the active phase typically depends on the domain size, with single phase reactions being favored as the domain size decreases. Differential capacity analysis is therefore extremely sensitive to the microstructure or nanostructure of alloys, provided data collection is sufficiently accurate. Differential capacity has been used to determine the impact of chemistry on microstructure in Si−M alloys[299] and Sn−M alloys (section 7.3.1). A particularly powerful feature of differential capacity analysis is the ability to monitor microstructure with cycling. In particular, grain growth in alloys, as exemplified in section 3.7.2.7, and in Figure 48, can be detected by this method. As the domains of the active phases in the alloys grow, single phase reactions gradually become two-phase reactions, as indicated by differential capacity peak growth. Finally, due to the differences in the average voltages and plateaus of graphite and alloys, differential capacity analysis of alloy/graphite composite electrode coatings in half-cells can easily reveal the independent behavior of graphite and alloy components during cycling.[12]

5.2. Symmetric Cells

Symmetric cells contain nominally identical electrodes with the exception that one of them is lithiated and one of them is delithiated.[427] While still having excess electrolyte, symmetrical cells do not have excess lithium, and do not have Li foil, eliminating the possibility of impedance growth on a Li foil electrode or possible electrode interactions. In addition to any fade discernible in half-cells, symmetrical cells will also show fade from lithium-consuming reactions with electrolyte. Symmetric cells are therefore most useful when assembled from electrodes showing little to no fade in half-cells. Few publications have investigated alloys with symmetric cells.[12,428−430] Applestone and Manthiram used symmetric cells to evaluate the benefits of VC, VEC, and FEC electrolyte additives for Cu_2Sb−Al_2O_3−C alloys. With traditional chemistries, symmetrical cells have been shown to be useful for screening electrolytes and additives, identifying negative/positive electrode interactions, and studying impedance growth.[427,428,431−434] As the alloy field moves toward increasingly good cycling performance in half-cells, symmetrical cell studies should become increasingly relevant.

5.3. Full Cells

To make a full cell yielding relevant results, a number of criteria must be met. Marks et al. detailed requirements on the electrodes themselves in their "Guide to Li-Ion Coin-Cell Electrode Making

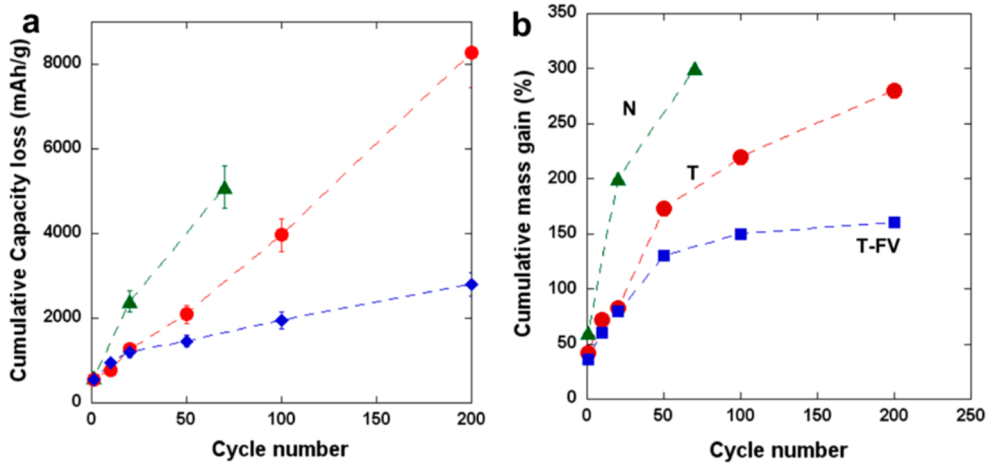


Figure 61. Neat Si/carbon black/binder electrodes with 100 nm Si nanoparticles cycled at a fixed 1200 mAh/g capacity. N, neutral pH slurry; T, slurry buffered with citric acid and KOH to pH 3; T-FV, 10 wt % FEC and 2 wt % VC added to electrolyte. (a) Cumulative capacity loss, (b) cumulative mass gain (%). Reprinted with permission from ref 380. Copyright 2012 Elsevier.

for Academic Researchers";[435] further requirements are mentioned in sections 2 and 7. To simulate conditions in commercial energy cells, the reversible loading of the electrode coatings should be greater than about 2 mAh/cm^2. A full cell should also have a negative electrode that slightly overlaps the positive electrode, to prevent lithium plating on the edges.[436] As explained in section 2.1, the ratio of the areal capacity of the negative electrode to the positive electrode (N/P) with the chosen voltage cutoffs should be greater than 1 to prevent lithium plating and less than ~1.2 to be representative of commercial full cells. The amount of electrolyte should be sufficient to wet the separator and fill the porosity of the electrodes, as in commercial cells, but the cell should not be flooded. Laminate cells allow controlled electrolyte volumes in laboratory settings. On the basis of Figure 6, the usefulness of making full cells from electrodes that have CEs of less than 99.7% in half-cells is doubtful.

Most of the full cell examples found in the literature do not meet the criteria listed above, making the interpretation of their results difficult. Fortunately, some studies appear to have reasonable full cell designs.[366,384,415,437,438] Kajita et al. reported full cells with a carbon-coated SiO, graphite, carbon fiber composite paired with NCA cathodes having an N/P of 1.25.[384] We calculate the cells to have reversible loadings near 2 mAh/cm^2. Unlike many authors, Kajita et al. not only cycled the cells to failure but explored various combinations of lower cutoffs (2.5, 3.0 V), upper cutoffs (4.0, 4.1, 4.2 V), and temperatures (20, 45, 60 °C). Figure 62a shows an example of failure through impedance growth caused by SEI buildup. Cells were cycled at a 1*C* rate with a slow *C*/10 cycle occurring every 50 cycles. The increasing gap between the *C*/10 and 1*C* cycled capacity when

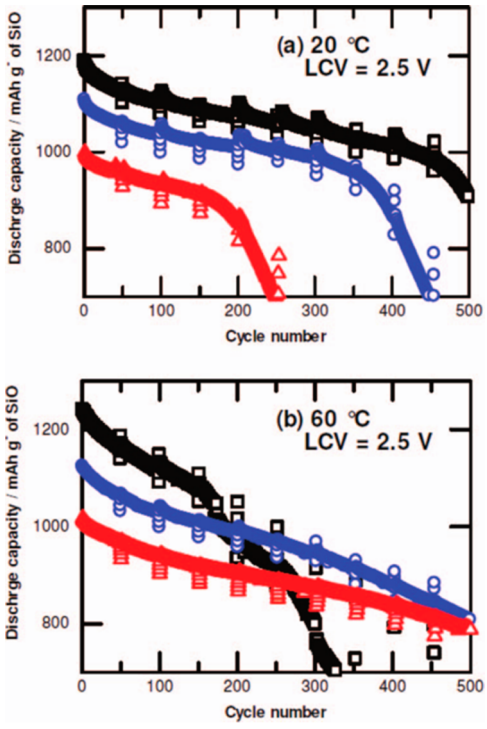


Figure 62. Cycling performance of full cells with C-SiO anodes and NCA cathodes with a 2.5 V lower cutoff voltage and an upper cutoff voltage of (black) 4.2 V, or (blue) 4.1 V, or (red) 4.0 V at (a) 20 °C or (b) 60 °C. Adapted with permission from ref 384. Copyright 2013 The Electrochemical Society.

significant capacity fade starts occurring is a signature of impedance growth. Also note that failure occurs earlier for lesser upper cutoff voltages. Kajita et al. identified impedance growth due to SEI as the main failure mechanism in these cells. Figure 58a and b shows that a thicker SEI was obtained with the 4.0 V upper cutoff voltage.[384] Figure 62b also shows sudden failure, but this time it occurs for the higher upper cutoff voltage and is due to complete electrolyte consumption via reactions at the cathode surface.[384] These results show that full cells implementing alloys need to be carefully designed and their cycling protocols optimized.

The problem of parasitic reactions appears to be the most important roadblock to real-world implementation of alloy materials. On the basis of citations and number of recent review articles,[18,168−170,409] the academic community is gravitating toward the nanosized approach as its main focus, for which the problem of parasitic reactions is even greater. It is unfortunate that plots of Coulombic efficiencies on reasonably expanded scales (95−100%) and relevant full cell data or symmetric cell data are either rare or nonexistent. There is a great need for careful studies of failure in full cells. High precision studies of failure[439] and the use of newly developed modeling[440,441] and diagnosis[442] tools would also help move the field forward.

5.4. Impedance Analysis

Impedance growth resulting from pulverization or network failure can readily be detected by GITT in half-cells.[443] Figure 63 shows the voltage curve of a Si-based half-cell undergoing GITT. Impedance is seen to rise sharply as the Si contracts during delithiation and increasing pressure on the cell increases the reversible capacity. GITT can also be effectively used to monitor increased impedance from SEI growth. Figure 64 shows that cycling Sn in dioxolane, which is stable in the anode cycling voltage window, results in greater capacity retention as compared to PC and lower impedance growth as detected by GITT.

Electrochemical impedance spectroscopy (EIS) is a standard method for characterizing Li-ion battery electrodes. The cell's response to an applied sinusoidal voltage with frequencies in the ~100 kHz to ~0.01 Hz range is typically presented as real and imaginary impedance in the form of a Nyquist plot. Briefly, high frequency (>100 kHz) impedance is related to electronic conductivity, midfrequency (100 kHz to 10 Hz) impedance is related to charge transfer resistance (transfer of Li^+ ions from the electrolyte to the active material and vice versa), and low frequency (<1 Hz) impedance is related to bulk diffusion.[178,444] EIS can be used with half-cells, symmetric cells, or full cells.

Many studies have used EIS to characterize alloy electrodes.[103,175,178,186,190,207,225,353,357,359,376,405,412,418,445−448] Because of its nondestructive nature, EIS can be performed at various states of charge and cycle numbers on a single cell. Focus is typically given to the midfrequency region and the charge transfer resistance (R_{ct}) as it is sensitive to SEI buildup and network failure. Figure 65a shows a Nyquist plot by Oumellal et al. of a n-Si electrode where the midfrequencies roughly correspond to the semicircles in the inset.[178] Equivalent circuits can be fit to the EIS data, and the width of the semicircle corresponds to the R_{ct}. Figure 65b shows the R_{ct} increasing with cycle number.

Results are fairly implementation dependent. Early studies of various alloys by Wang et al. showed impedance growing during lithiation.[376] On the other hand, Oumellal et al. found decreasing impedance during lithiation in n-Si cells.[178] Chen et al. found VC effective in minimizing the impedance growth of Si thin films

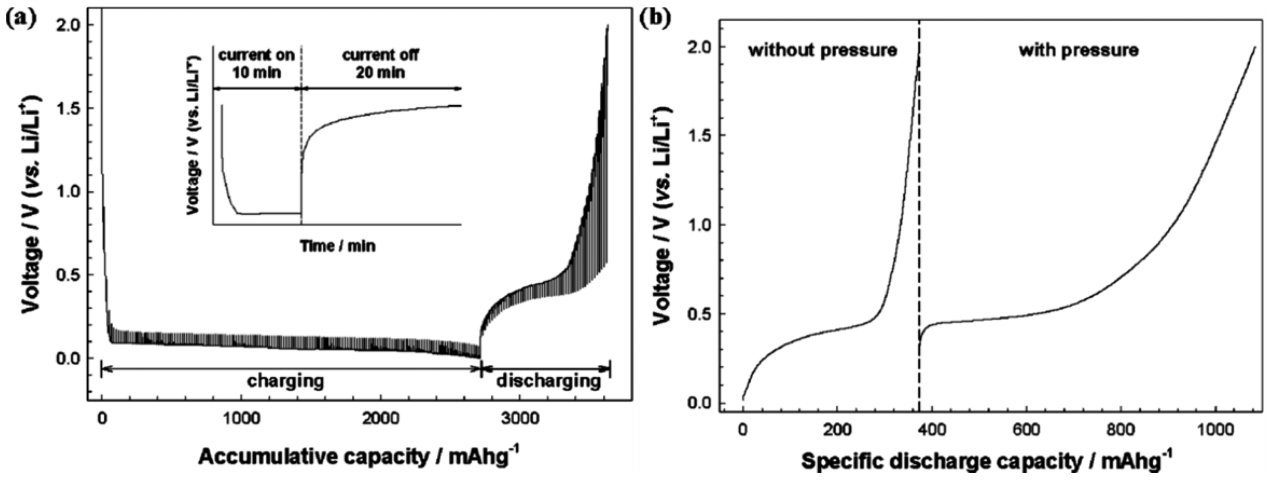


Figure 63. (a) Transient voltage profiles obtained with GITT. Inset: A typical voltage transient traced in one current pulse cycle showing rising impedance upon delithiation. (b) Delithiation voltage profile of a pouch cell recorded under normal conditions without pressure and obtained under a pressure (1.3 kg/cm^2). Adapted with permission from ref 443. Copyright 2004 The Electrochemical Society.

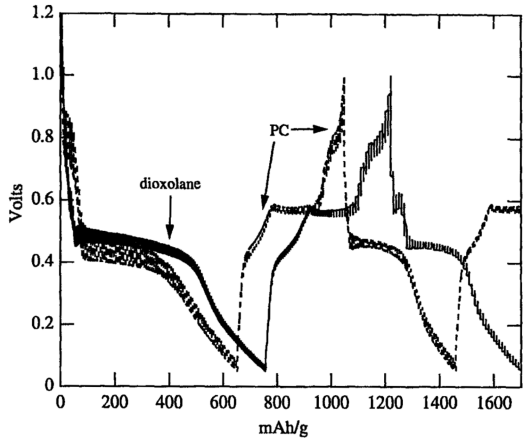


Figure 64. Voltage profiles of fresh tin electrodes cycled in dioxolane and PC electrolyte. The current was interrupted every 10 min. Cells were cycled between 1.0 and 0.05 V at a $C/30$ rate. Reproduced with permission from ref 102. Copyright 2001 The Electrochemical Society.

with cycling,[225] while Hu et al. found VC increased the R_{ct} of SiO-based electrodes.[412] Ding et al. reported a lower R_{ct} with EC-DEC-based as compared to PC-based electrolytes for Si electrodes.[448] Ruffo et al. found R_{ct} to decrease with cycling for Si nanowires,[186] while Oumellal et al. found increasing R_{ct} with cycling in n-Si electrodes, as shown in Figure 65.[178]

Another easy method for tracking the impedance of electrodes with cycling is the addition of a rest step at the end of each lithiation and delithiation. The time dependence of the voltage relaxation can be used as an impedance metric.[12] This approach is a variant of the traditional area-specific impedance metric.[449]

5.5. Acoustic Emission Analysis

Acoustic emission studies (AE) were originally performed on Li/MnO_2 cells[450] and are particularly well-suited to the study of alloy materials; unfortunately, few have been published.[157,451,452] As presented in section 3.6.1.4 and shown in Figure 28, the pulverization of Si particles can be quantified during cycling using AE.[157] To our knowledge, the ability to provide a quantitative measure of particle fracture averaged over the whole electrode is unique to this technique.

5.6. Dilatometry

The importance of thickness expansion in alloy approaches was recognized early. Already in 1996 Yang et al. reported dilatometry studies of alloy cycling.[453] Several papers have been published using various techniques to measure the expansion of electrodes using dilatometers,[20,399,411,453,454] displacement gauges,[349,455] noncontact dilatometer,[456] or ex

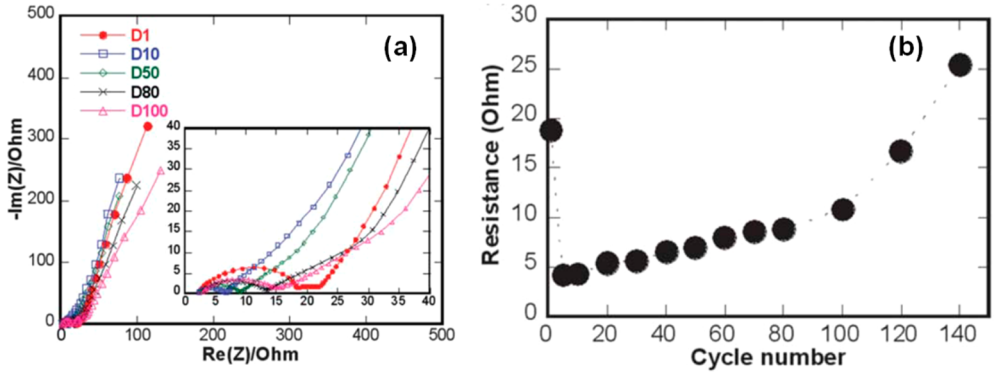


Figure 65. EIS results of n-Si electrodes in three-electrode cells. (a) Nyquist diagrams upon cycling at the end of lithiation after 1, 10, 50, 80, and 100 cycles. (b) Evolution of the charge transfer resistance (R_{ct}) with cycle number. Reproduced with permission from ref 178. Copyright 2011 The Royal Society of Chemistry.

dx.doi.org/10.1021/cr500207g | Chem. Rev. 2014, 114, 11444−11502

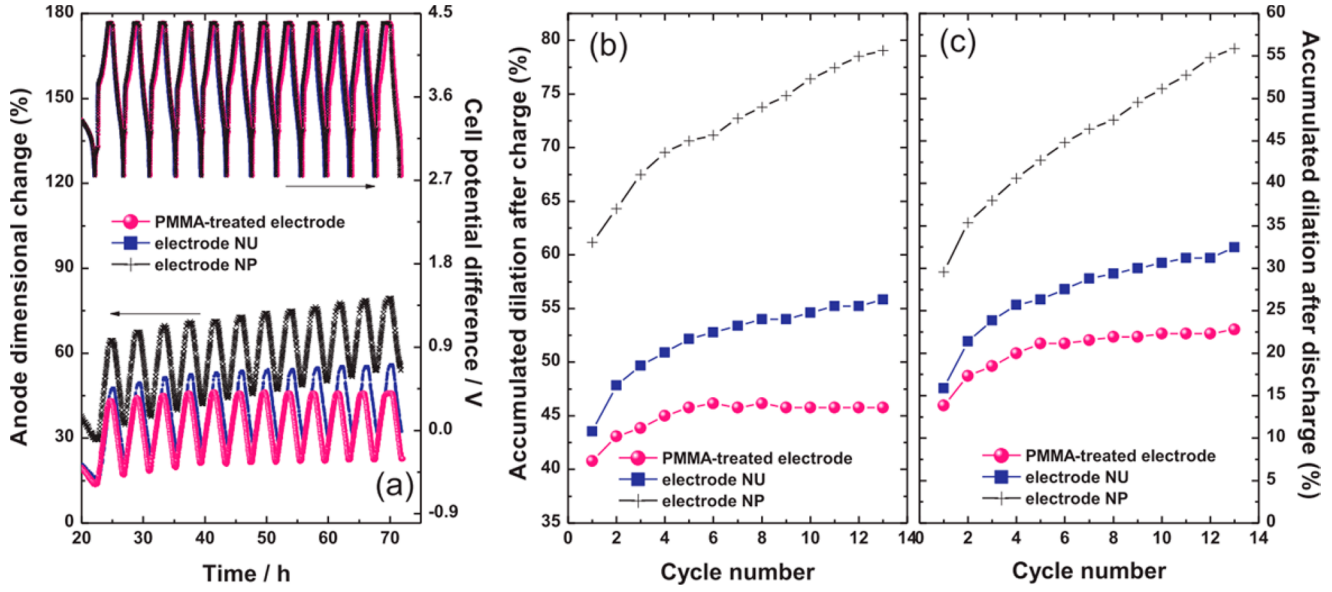


Figure 66. Full cells of $Si_{75}Fe_{25}$/Super P/polyimide anodes paired with $LiCoO_2$ cathodes. Anodes were unpressed (NU), pressed (NP), or unpressed with porosity controlled by PMMA. (a) Voltage profile and dilation behavior of full cells in the load cell during cycling, (b) variations in the accumulated dilation after each charge step, and (c) variations in the accumulated dilation after each discharge step. Reprinted with permission from ref 454. Copyright 2011 Elsevier.

situ micrometer.[35,380] Figure 66 shows data from full cells of $Si_{75}Fe_{25}$/Super P/polyimide anodes paired with $LiCoO_2$ cathodes. The volume is seen to increase nearly linearly with full cell charging and decrease with cell discharging in a very repeatable manner. Figure 66b and c shows that the overall thickness of the cell is increasing with cycle number at the end of both charge and discharge. The porosity of the electrode is seen to have a major effect on dilation behavior.[454] Given that most portable electronics use pouch cells with tight dimensional tolerances, the expansion of alloy-based electrodes will become an increasingly relevant topic.

5.7. Isothermal Calorimetry

Krause et al. have shown that in situ calorimetry and high precision coulometry can be combined with symmetrical cells to quantitatively measure parasitic reactions on a per cycle basis.[457] In a recent paper, Chevrier et al. used this technique with high-loading (~3 mAh/cm^2) alloy/graphite/SP/LiPAA composite electrodes of equal volumetric capacity containing either micrometer-sized active/inactive Si-based alloy particles or 60 nm Si nanoparticles.[12] The electrodes had similar capacity retention, although the active/inactive Si-based alloy resulted in a CE of 99.8% as compared to 99.2% for Si nanoparticles. Parasitic reactions with electrolyte at the anode surface were found to scale with surface area resulting in significantly higher parasitic reactions for Si nanoparticles. Parasitic reaction measurement results have also been presented using the same active/inactive Si-based alloy demonstrating the ability to quantitatively distinguish network failure, where Li atoms are lost by disconnection, from parasitic failure, where Li atoms are lost to SEI.[429] Figure 67 shows combined coulometry and calorimetry data for a reference graphite electrode where a linear relationship was found between number of Li lost during cycling and thermal parasitics.[429] In graphite electrodes, the vast majority of Li is lost to SEI, and the slope can be used to calculate the average enthalpy of reaction of the SEI products (220 kJ/mol). A well-designed Si alloy containing electrode with small flake graphite (V6/HE1/KS6) is shown to lie on the same 220 kJ/mol line,

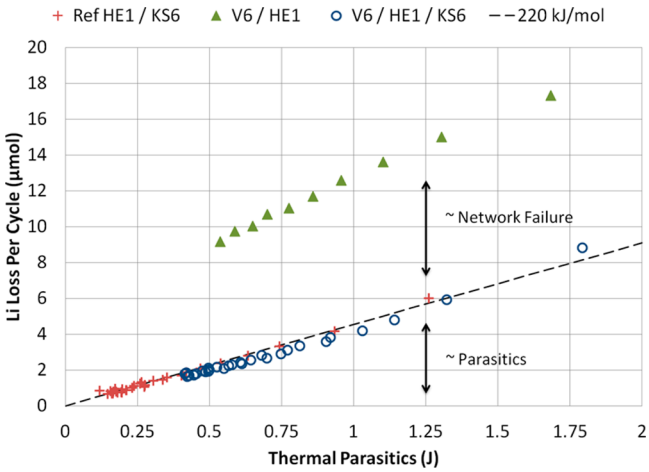


Figure 67. Energetics of lithium loss shown for various electrodes. Electrodes are (red +) reference graphite electrode consisting of Hitachi HE1/Timcal KS6/SP/LiPAA: 75/13/2/10, (green ▲)V6" Si-based active/inactive alloy/HE1/SP/LiPAA: 26/62/2/10, and (blue ○) V6 alloy/HE1/KS6/SP/LiPAA 26/44/18/2/10. Addition of KS6 is seen to significantly mitigate network failure. Adapted with permission from ref 429.

indicating little network failure and similar decomposition products. However, an electrode without a flake graphite component to maintain network conductivity is seen to have significantly greater Li loss for a given level of thermal parasitics. The amount of Li lost beyond the expected 220 kJ/mol can be attributed as being lost to the electrode through network failure.

6. THERMAL STABILITY OF ALLOY NEGATIVE ELECTRODES

The academic literature related to the thermal stability of alloy anodes is limited, and much remains to be studied. Thermal stability studies have until now focused on Si, $Sn_{30}Co_{30}C_{40}$ or SiO. These materials are found to have better thermal stabilities

dx.doi.org/10.1021/cr500207g | Chem. Rev. 2014, 114, 11444−11502

than graphites of equivalent surface area. Reports of safety testing on full cells are few. Safety testing on full cells was reported by Yamada et al. for a SiO−C composite paired with a LCO:NMC blend,[437] and by Kataoka et al. for SnC_2O_4-coated Si paired with LFP.[373] In both cases, the full cells passed nail penetration and overcharge tests without going into thermal runaway. The SiO−C/LCO:NMC cell also successfully underwent a 150 °C oven test without experiencing thermal runaway.

6.1. Reactivity of Alloy Anodes As Compared To Graphite

Wang and Dahn published a series of papers focused on the reactivity of lithiated Si as compared to graphite using accelerating rate calorimetry (ARC).[164,458,459] Electrodes of micrometer-sized Si or mesocarbon microbeads (MCMB) graphite having active material/Super S/PVdF weight ratios of 80/12/8 were lithiated to various levels. The Si and the MCMB had respective surface areas of 1.04 and 0.81 m^2/g. The weights of active materials for ARC were designed to compare Li_xSi and $Li_{0.81}C$ in quantities yielding equivalent moles of Li. In all conditions, Li_xSi was found to have lower self-heating rates than graphite, although the features of the self-heating curves were similar. The most significant difference in the thermochemistry of Li_xSi and $Li_{0.81}C$ in pure EC:DEC was the formation of lithium silicates and SiC above 300 °C for Li_xSi. The authors did not find the higher average voltage of Si to impact thermal results significantly and conclude: "We believe this effect to be very general: materials of high volumetric capacity will have lower self-heating rates than materials of low volumetric capacity that contain the same number of moles of lithium and have the same particle size."[458] Using similar techniques, Zhou et al. compared lithiated $Sn_{30}Co_{30}C_{40}$, LiSi, and $Li_{0.81}C$ and found that their thermal stability was in the order of: lithiated $Sn_{30}Co_{30}C_{40}$ > LiSi > $Li_{0.81}C$.[460] Whereas Si led to the formation of lithium silicates, the CoSn grains did not react with the electrolyte up to 350 °C.

6.2. Impact of Solvent and Salt on Alloy Thermal Stability

The sequence of reactions for lithiated Si in electrolyte has been found to start with the decomposition of the SEI below 100 °C, followed by the decomposition of $LiPF_6$ above 100 °C, and, depending on conditions, the possible complete reaction of Si with the solvent at higher temperatures.[461] Wang and Dahn[458] as well as Profatilova et al.[461] found the reactivity of lithiated Si to be significantly reduced by the presence of $LiPF_6$. Between 107 and 140 °C, decomposition products from $LiPF_6$, including LiF, form a protective film and suppress the reaction between the Li in the active material and the solvent. Wang and Dahn found the addition of LiBOB salt to also suppress reaction, but through the production of Li_2CO_3 and alkyl carbonates. Profatilova et al. found that LiTFSI was ineffective in preventing exothermic reactions.[461]

As detailed in section 4.3, FEC and VC are known to have considerable impact on the cycling of alloys and the chemistry of the SEI. Profatilova et al. studied the effect of FEC and VC on the thermal stability of lithiated n-Si.[462] Figure 68 shows that the presence of FEC or VC delays the onset of large exothermic reactions from 153 to 200 and 214 °C, respectively. Not only is the SEI formed by FEC or VC during electrochemical cycling thermally stable, but further surface passivation from FEC or VC decomposition at higher temperature delays the onset of thermal runaway.

6.3. Impact of Surface Area on Alloy Thermal Stability

As mentioned above, Wang and Dahn found lower self-heating rates for lithiated Si and $Sn_{30}Co_{30}C_{40}$ than for lithiated graphite

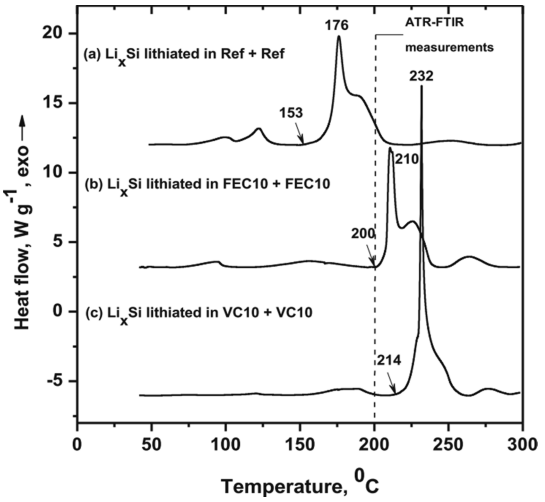


Figure 68. DSC profiles of Li_xSi heated in contact with the same electrolyte that was used for lithiation at a temperature ramp of 2 °C/min. The lithiated electrodes were rinsed in a DMC solvent and scratched off the current collector prior to DSC measurements. The dashed line indicates the temperature at which ATR-FTIR spectra were recorded. (a) Reference electrolyte: 1 M $LiPF_6$ in EC:DEC 3:7 by mass, (b) reference electrolyte + 10 wt % FEC, and (c) reference electrolyte + 10 wt % VC. Reprinted with permission from ref 462. Copyright 2013 Elsevier.

using materials having low surface areas (≤1 m^2/g).[164,458] Self-heating began to be detectable starting at ∼200 °C for Li_xSi in electrolyte, and thermal runaway (20 °C/min) was either not reached[164,458] or was only detected above 275 °C,[460] depending on test conditions. On the other hand, Profatilova et al. studied the thermal stability of lithiated 12 m^2/g n-Si in the presence of electrolyte.[461,462] This led to major exotherms in DSC measurements between 150 and 200 °C. Park and Lee compared the thermal stability of lithiated Si powders having particle sizes of 15 μm, 5 μm, and 30−50 nm.[463] Figure 69 shows the large impact of particle size, and consequently surface area, on the thermal stability of lithiated Si. In agreement with previous ARC studies,[164,458,460] micrometer-sized Si is found to be more

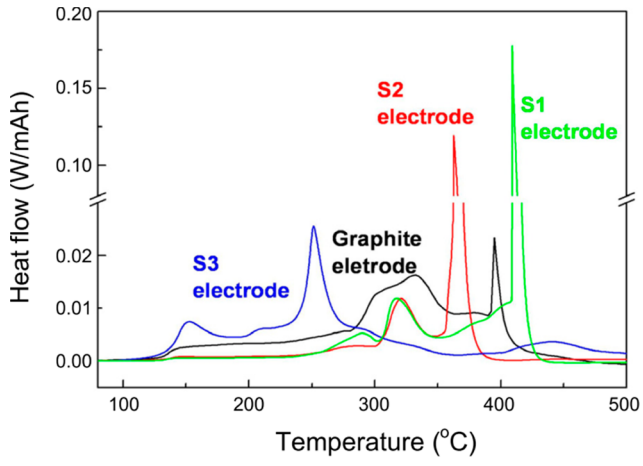


Figure 69. Capacity normalized heat flow from DSC measurements conducted on various active materials lithiated to 5 mV. S1:15 μm Si, S2:5 μm Si, S3:30−50 nm Si, graphite: carbon coated natural graphite. Reprinted with permission from ref 463. Copyright 2011 The Korean Chemical Society.

dx.doi.org/10.1021/cr500207g | Chem. Rev. 2014, 114, 11444−11502

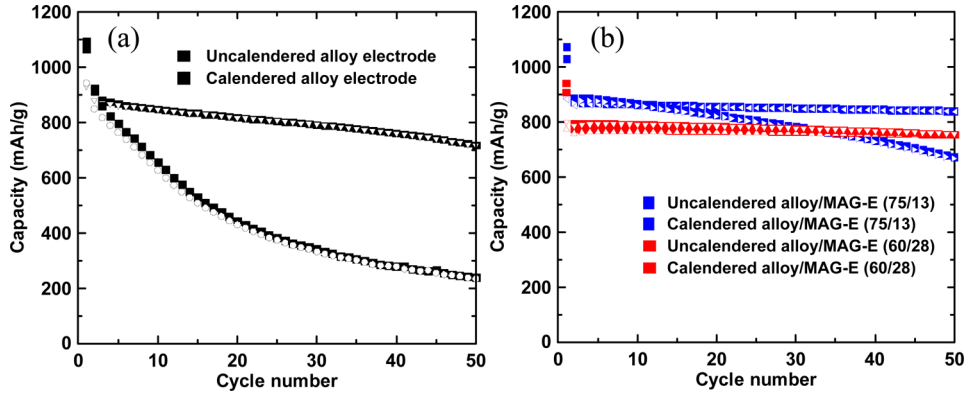


Figure 70. (a) The effects of calendering on a Si alloy/PAA binder electrode. (b) The cycling of calendered and uncalendered electrodes comprising Si Alloy/MAG-E/PAA with different alloy/MAG-E weight ratios (MAG-E = Hitachi massive artificial graphite). Reproduced with permission from ref 35. Copyright 2014 The Electrochemical Society.

thermally stable than graphite; however, n-Si is found to be less thermally stable than graphite. These results warrant further study of the thermal stability of the various nanoapproaches proposed for Si.

It should be noted that all of the studies of thermal stability cited above were conducted on materials that were lithiated or delithiated only once. Given the large impact of cycling on the SEI and surface area (pulverization) of alloy materials, there appears to be a need for thermal stability studies of cycled alloys.

7. IMPLEMENTATION IN COMMERCIAL CELLS

This section will describe how alloys might be implemented in commercial cells. Calculations showing the impact of alloy volumetric capacity, voltage, irreversible capacity, and coating porosity on cell energy have already been described in section 2. Methods of dealing with irreversible capacity and making coatings with low volume expansion and low porosity will be described. This will be followed by a review of some high performance alloys that have been used or have been suggested for use in commercial cells.

7.1. Irreversible Capacity Management

As shown in Figure 5, anode irreversible capacity can severely reduce cell energy. The maximum cell energy is obtained when the anode irreversible capacity exactly matches that of the cathode.[12,464] Any greater increase in the anode irreversible capacity causes the cell energy to decrease. Therefore, one method of dealing with high anode irreversible capacity is to choose a cathode material that also has high irreversible capacity.[12,464] High energy density cathode materials that also have high irreversible capacities (up to ~30%) are known to exist.[465,466] The use of such materials could go a long way in eliminating the effects of irreversible capacity of alloy materials.

The methods for managing irreversible capacity in full cells reported in the academic literature chiefly involve adding a source of sacrificial lithium. This includes prelithiating the anode prior to cell assembly or adding lithium powder to the anode, which then spontaneously lithiates the anode after electrolyte is added to the cell.[467−469] Lithium compounds have also been suggested as a source of sacrificial lithium, such as $Li_{2.6}Co_{0.4}N$.[470,471] Usually the sacrificial lithium powder or lithium compound is blended directly with the anode coating. Careful coating design is required, because the sacrificial lithium will occupy some coating volume. Additionally, because many of these compounds are not water-stable, they are not compatible with water-based binders. Recently, Armand et al. suggested adding lithium salts with an oxidizable anion to the cathode as a method of compensating for irreversible capacity at the anode.[472] During the initial charge, the salts decompose and act as a source of lithium in the cell (effectively increasing the irreversible capacity of the cathode).

7.2. Coating Design for Commercial Cells

Commercial graphite electrodes for energy cells have high loadings (>2 mAh/cm^2), large thicknesses (>30 μm), comprise large amounts of active graphite (>~95% by mass), and low amounts of inactive components, such as binder or carbon black. Such coatings are typically calendered under high pressures, reducing the porosity from ~50% as-coated to 10−40%. Calendering improves the electrode density, the electrode cycling stability, the coating adhesion, and the electrical conductivity. On the other hand, an electrode that has been overcalendered will not have sufficient porosity to allow liquid-phase Li diffusion from the electrolyte to the electrode particles, resulting in high electrode impedance, and reduced rate performance.[435,473−476] As a point of reference, a typical commercial graphite coating comprising graphite/binder in a 97/3 w/w ratio with 20% porosity has a capacity of about 550 Ah/L at full lithiation and has an average voltage of about 125 mV. This results in a full stack energy density of about 726 Wh/L, using the cell stack model developed in section 2.

According to Figure 5, a pure Si coating with 50% active volume will have a 20% improvement in energy density compared to a conventional graphite cell. Therefore, the high volumetric capacity of Si potentially allows a completely different approach than conventional high density coatings and allows for the design of coatings with porosity that may accommodate volume expansion. Beattie et al. showed that Si/Super P/CMC in a 1/1/1 weight ratio with no calendering could yield a viable electrode with ~3 mAh/cm^2 at low rate.[176] Bridel et al. further optimized and studied this system[177,353] reporting 100 cycles with ~86% capacity retention, a 50% initial porosity, and ~110% expansion and 960 Ah/L capacity at full lithiation. Assuming an average voltage of 0.4 V (pure Si), such an electrode would result in a 813 Wh/L full cell capacity or a 12% improvement as compared to graphite, using our full cell model. This is quite decent.

The approach described above would not be appropriate for alloys of Si or Sn that have much reduced capacities as compared to the pure elements. At about 50% porosity, many alloy coatings are likely to have inferior energy densities than highly calendered

dense graphite coatings. For such alloys there is a need to reduce porosity by calendering. Many studies report calendering or pressing their electrodes.[103,304,319,345,362,373,400,415,419,447,477−482] Few provide sufficient information for calculating the resulting electrode volumetric capacity; however, some exceptions can be found. For instance, Jeong et al. made calendered $Si_{75}Fe_{25}$/Super P/polyimide electrodes, optionally containing PMMA to control porosity.[454] These coatings contained only Si alloy as an active material. Jeong et al. state that the volumetric capacity of their coating at full lithiation is 587 Ah/L.[454] This corresponds to an energy of only 689 Wh/L in our full cell model or a 5% decrease in energy as compared to a calendered graphite coating. This illustrates that careful design of electrode active materials and porosity is required to provide electrodes that result in high energy full cells.

We are aware of only two studies that thoroughly examine the effects of calendering on alloy electrodes.[35,476] The statement by Gauthier et al. highlights the need for further studies: "An important prospect to achieve realistic and practical electrode density for commercial Li-ion batteries would then be to study the influence of calendaring on the cycling behavior of silicon-based composite electrodes, which has never been reported as far as we know."[167]

In 2014, the importance of graphite blending on energy density and cyclability in alloy-containing electrodes with 20% porosity was carefully studied by Du et al.[35] Calendered alloy/binder electrodes were found to cycle poorly due to the inability of the Si-alloy to sustain calendering without fracturing into smaller particles, as shown in Figure 70a. The addition of sufficient graphite to the electrode allows calendering without particle fracture, improves cycling, lowers the average voltage, and ultimately increases the achievable energy density in full cells as compared to graphite. This effect is shown in Figure 70b. Using volumetric capacities after expansion, an improvement of 17% in energy density as compared to graphite was obtained in a full cell model. Finally, Du et al. showed that the particle size of the alloy and the graphite must be compatible to ensure a good dispersion.[35] Chevrier et al. also reported that industrial slurry mixing methods usually rely on high shear, whereas academic papers routinely use milling techniques such as planetary milling with media, which may lead to higher surface area.[12] Through the addition of small flake graphite, alloy/graphite composites electrodes obtained from high shear-mixed slurries had a good particle dispersion, and better capacity retention and CE than those obtained from planetary milling.

7.3. Some Industrially Developed Alloy Materials

The commercial implementation of alloy materials remains elusive. Only a handful of alloys have made it to commercial cells. To our knowledge, the first attempt was made in the late 1990s by Fujifilm Celltech with the "Stalion" cell containing a Sn−oxide amorphous glass containing P, B, and Al.[9] This attempt was unsuccessful, likely due to the challenges resulting from the large irreversible capacity, voltage-dependent aggregation of Sn, and relatively low volumetric energy gains, as discussed in section 3.7.2.7. The remainder of this section will focus on materials that are currently commercialized or for which commercialization is being attempted.

7.3.1. Sn−Co−C Alloys. In 2005 Sony announced and commercialized the "Nexelion" cell for hand-held camcorder battery packs using the following description: "The newly developed tin-based amorphous anode is a material consisting of multiple elements such as tin, cobalt, carbon, where the elements are mixed on a nanometer level."[483] Sony subsequently presented the material at conferences, describing the alloy as having Co−Sn grains dispersed in an amorphous carbon matrix.[484,485] Sony did not present further studies in the academic literature and to our knowledge has not stated the exact composition of the SnCoC alloy nor its synthesis method. Academic researchers have pointed to various forms of ball milling.[486,487] In 2011, Sony announced another iteration of the Nexelion cell in an 18650 format aimed at Notebook PCs having 3.5 Ah and 723 Wh/L in a 2.0−4.3 V range.[488]

Following Sony's 2005 announcement, detailed studies of this composition space were published mainly by Dahn, Ferguson, and Todd et al.,[10,78,320,355,460,487,489−501] as well as Scrosati and Hassoun.[502−504] Published accounts of Nexelion cell disassembly and cycling were published by Fan et al.,[505] Zhang et al.,[506] and Wolfenstine et al.[507,508] These literature studies form the basis of the discussion below.

Disassembly of Nexelion cells revealed ∼1 um alloy particles with a majority of Sn and Co in a 1:1 atomic ratio and small amounts of Ti (<5 at. %).[505,507] TEM images revealed Sn−Co grain sizes of ∼5 nm, and the reversible capacity of the alloy was approximately 400 mAh/g.[505] Literature studies of Sn−Co−C alloys through sputtering,[78] high energy ball milling,[503,504] and attritor milling[10] quickly narrowed to the $Sn_{30}Co_{30}C_{40}$ composition. Figure 71 shows the impact of synthesis method on the microstructure. Sputtering yields an extremely homogeneous microstructure having CoSn grain sizes on the order of 1 nm, which is much smaller than the commercial alloy. Attritor milling with $CoSn_2$ + Co + graphite starting materials yields a microstructure of ∼6 nm CoSn grains (white in Figure 71b) in a C matrix (gray-black in Figure 71b) that is very similar to the commercial alloy. The carbon matrix is necessary to prevent the agglomeration of larger Sn regions during cycling, thereby imparting excellent cycle life.[78]

Sony's Sn−Co−C material is reminiscent of the Sn−Fe−C materials previously reported by Mao et al.[323,509−511] Cobalt is an expensive transition metal; a good reason for its choice in a commercial product must therefore exist. Todd et al. developed a rationale for the choice of Co as the ideal transition metal for the Sn−TM−C composition space.[501] In sputtered Sn−M (M = Ti, V, Cr, Mn, Fe, Co, Ni, Cu) libraries, only Ti, V, Cr, and Co displayed substantial amorphous regions.[320] Given the benefit of amorphous microstructures in alloy cycling, the other transition metals were eliminated as candidates. For all Sn−Co compositions, whether the starting material was crystalline or amorphous, cycling ultimately resulted with the aggregation of Sn.[320] Ternary $Sn_{1-x-y}M_xC_y$ (M = Ti, V, and Co) ($0 < x < 0.5$ and $0 < y < 0.5$) combinatorial libraries were then electrochemically and structurally studied.[501] For both Ti and V, the addition of carbon was found to precipitate crystalline Sn as determined by XRD in the as-sputtered films. On the other hand, for Co the addition of carbon did not result in the formation of crystalline Sn. Electrochemical cycling of the Sn−Co−C compositions showed stable differential capacities characteristic of amorphous microstructures and no sign of Sn agglomeration. Study of the phase diagrams of M−C revealed that Co was the only transition metal that does not form carbides in equilibrium conditions. Sn also does not form carbides. The presence of Co ensures a nanocrystalline/amorphous active environment with Sn while diluting the volume expansion, and the C offers a stable matrix keeping the active CoSn grains separated. Furthermore, the C matrix contributes capacity.[78] Figure 72 shows Todd et al.'s

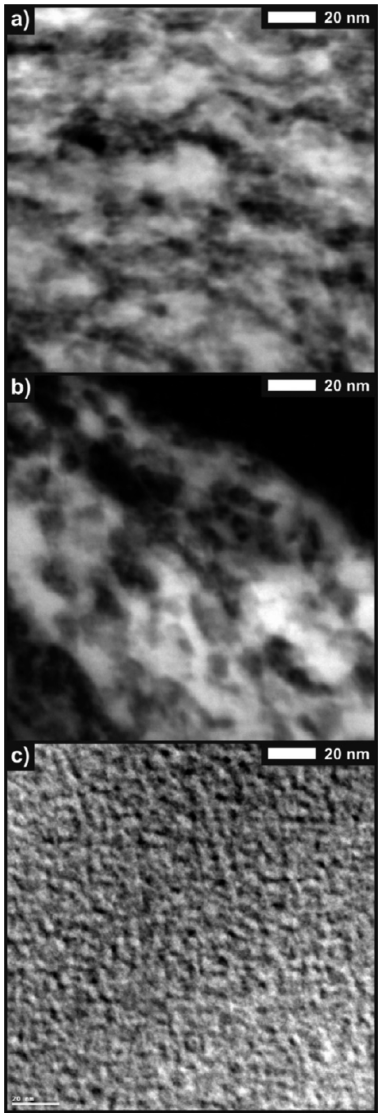


Figure 71. TEM images of $Sn_{30}Co_{30}C_{40}$ alloy prepared by (a) 16 h of attritor milling with CoSn, graphite starting materials, (b) 16 h of attritor milling with $CoSn_2$, Co, graphite starting materials, and (c) sputtering from $Sn_{50}Co_{50}$ and graphite targets. Reprinted with permission from ref 491. Copyright 2012 Elsevier.

schematic decision tree resulting in Co as the only viable choice for Sn−M−C alloys.[501]

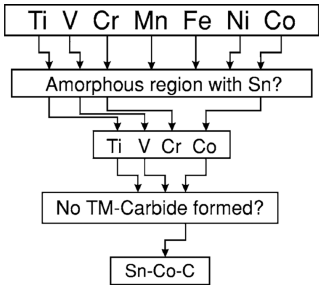


Figure 72. Roadmap to the selection of the Sn−Co−C system as the best choice among Sn−M−C systems for negative electrodes in Li-ion batteries. Reproduced with permission from ref 501. Copyright 2007 The Electrochemical Society.

Considerable details on the electrochemistry of the Sn−Co−C system can be found in Todd et al.'s review and references therein.[487] We summarize here the key points. Figure 73 shows

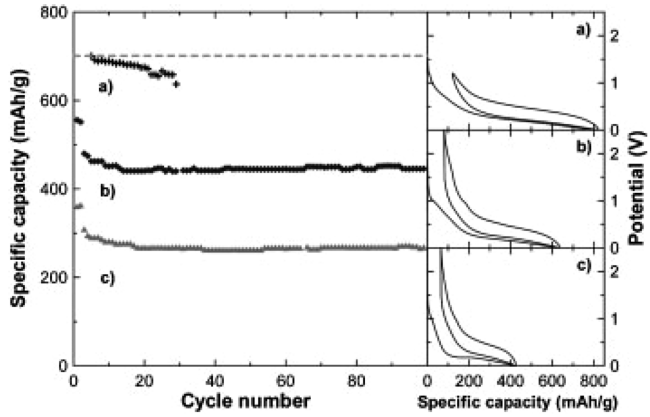


Figure 73. Left panel: Specific capacity versus cycle number for $Sn_{30}Co_{30}C_{40}$ electrodes: (a) combinatorially sputtered film, (b) attritor milled $CoSn_2$ + Co + graphite, and (c) attritor milled CoSn + graphite. Right panel: Potential versus specific capacity of the first cycle for samples described in left panel of this figure. Electrodes formulations were: 80% attrited powder, 12% conductive carbon black, and 8% binder. Testing was done at 30 °C. Reproduced with permission from ref 487. Copyright 2010 John Wiley & Sons, Ltd.

cycling results and voltage versus capacity curves for alloys of identical composition ($Sn_{30}Co_{30}C_{40}$) but different synthesis methods as described in the caption. The voltage curves are smooth and characteristic of single-phase lithiation/delithiation. Through a series of XRD,[10,489,500] Mössbauer,[489,493−496,500] small angle neutron scattering,[490,492] and TEM[491] studies, the grain size of CoSn has been established as the dominant factor dictating the achievable capacity in $Sn_{30}Co_{30}C_{40}$ alloys. The material obtained by sputtering has the smallest grain size (~1 nm) resulting in the most active CoSn grains, achieving about 610 mAh/g reversible capacity.[10] $Sn_{30}Co_{30}C_{40}$ by mechanical attrition achieved about 470 mAh/g. Zhou et al. indicate this material as having a density of 6.7 g/cm^3 and 150% expansion yielding a volumetric capacity of 1260 Ah/L.[460] Assuming an average voltage of about 0.45 V from the voltage curves shown leads to a 796 Wh/L stack energy density or a 10% improvement over graphite using our cell model. Recent high precision charger measurements of half-cells containing attrited $Sn_{30}Co_{30}C_{40}$ alloy powder electrodes have shown CEs at cycle 25 of 99.75% and 99.65% with and without 10% FEC, respectively, as compared to 99.90% for graphite in similar cells.[397] It is worth noting that other phases in the Sn−Co−C phase diagram exist and become relevant if one steers away from the Sn:Co 1:1 ratio. Ferguson et al. explored the impact of varying x in $(Sn_xCo_{1-x})_{60}C_{40}$. Figure 74 shows the capacity decrease for $x < 0.5$ due to the appearance of inactive and metastable phases $SnCo_3C_{0.7}$ and subsequently Co_3C.

Cycling and testing of Nexelion 14430 cells has been reported by Fan et al.,[505] Wolfenstine et al.,[507] Foster et al.,[508] Christensen et al.,[512] Todd et al.,[487] and Smith et al.[397] To our knowledge, these cells were as described in the 2005 Sony press release, and no evaluations of the cells presented in the 2011 press release have been published. According to the 2005 press release, these cells have a 14430 (AA) format with 900 mAh at C/5 and 2.5−4.2 V cutoffs, resulting in a cell energy of 478 Wh/L or 158 Wh/kg. These numbers have been confirmed by Foster et al.[508] The

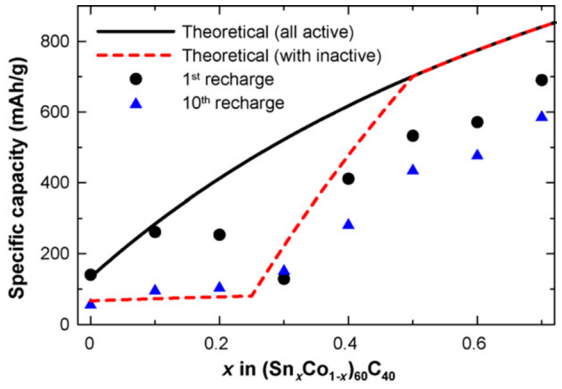


Figure 74. Specific capacity versus x in $(Sn_xCo_{1-x})_{60}C_{40}$ for samples prepared by vertical axis attritor milling. Data were measured at the end of the first recharge (delithiation) to 2.5 V and at the end of the 10th delithiation 1.2 V. The solid line is a calculation assuming each Sn and C atom can react with 4.4 and 0.5 Li atoms, respectively. The dashed line is a calculation assuming Co_3C and $SnCo_3C_{0.7}$ are inactive with Li and the samples are described by the phase diagram (see Figure 5 of ref 489). Reprinted with permission from ref 489. Copyright 2009 Elsevier.

negative electrode is a graphite/alloy blend with alloy particles of less than 1 um, and the cathode is a LCO/NMC-type blend in a 80:20 volume ratio.[505−507] Figure 75 shows the cycle perform-

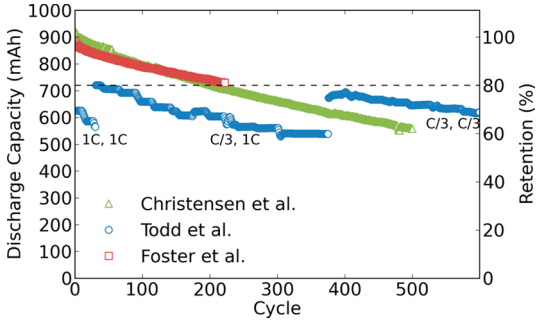


Figure 75. Cycling of Nexelion 14430 cells. Data derived from refs 512, 508, and 487. Christensen et al.: CCCV charge at $C/2$ to 4.2 V with trickle down to $C/10$, CC discharge at $C/2$ to 2.5 V.[512] Foster et al.: cycling conditions unknown.[508] Todd et al.: cycling currents are indicated on the figure as "charge,discharge".[487] Retention axis based on the Sony press release stating a capacity of 900 mAh at $C/5$ with 2.5 and 4.2 V cutoffs.[483]

ance of the Nexelion 14430 cell. The cells cross the 80% retention mark between 200 and 250 cycles. The cycling protocols used are unlikely to be ideal as Foster et al. note that the cells were designed to be discharged at $C/6$.[508] The lower capacities observed at higher rates by Todd et al. should therefore not be surprising. Smith et al. reported the CE and voltage curve of a Nexelion cell at $C/24$ with 2.5 and 4.1 V cutoffs, shown in Figure 76.[397] The slippage occurring at the bottom of discharge and the lack of slippage at top of charge are indicative of negative electrode related fade. The CE stabilized near 99.75% as compared to 99.90% for a commercial LCO/graphite 18650 in similar conditions. According to Figure 6, a sustained CE of 99.75% should result in a capacity retention of only about 60% after 200 cycles. The discrepancy between the cycle life predicted by a CE of 99.75% and the cycling reported above is likely due to the very slow $C/24$ cycling employed to measure CE, which would include time-based fade not measured in the faster cycling reported above.

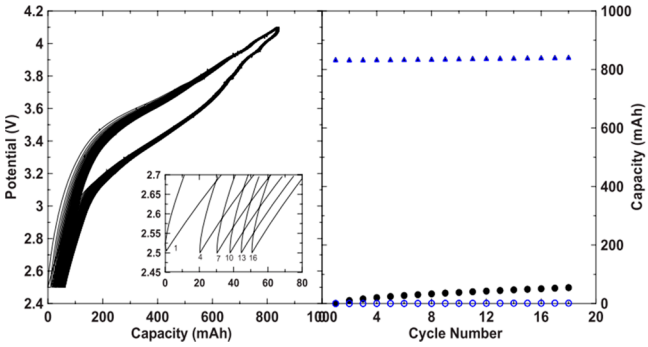


Figure 76. Nexelion voltage. Left panel: Potential versus capacity for the measured cycles of the Nexelion cell. The inset shows the details at the bottom of the discharge curve. Right panel: The charge (▲) and discharge (●) end-point capacities plotted versus cycle number. An estimate of the maximum possible error due to the charger system is also given (○). Reproduced with permission from ref 397. Copyright 2010 The Electrochemical Society.

7.3.2. SiO-Based Electrodes. SiO (or SiO_x) is typically synthesized by sublimation of a Si and SiO_2 mixture in an inert atmosphere.[513] The resulting sublimate powder is amorphous with a microstructure that has been debated over the past decades. The two principal models are the random bonding (RB) model in which SiO is thought of as a single-phase material with Si−Si and Si−O bonds randomly distributed throughout,[514,515] and the random mixture (RM) model in which n-Si grains (<10 nm) are randomly distributed within an SiO_2 matrix,[366,399,516−520] which is illustrated in Figure 77. Recently, Schulmeister et al. have suggested a model that is somewhat between the RM and RB models.[521] They propose that SiO is

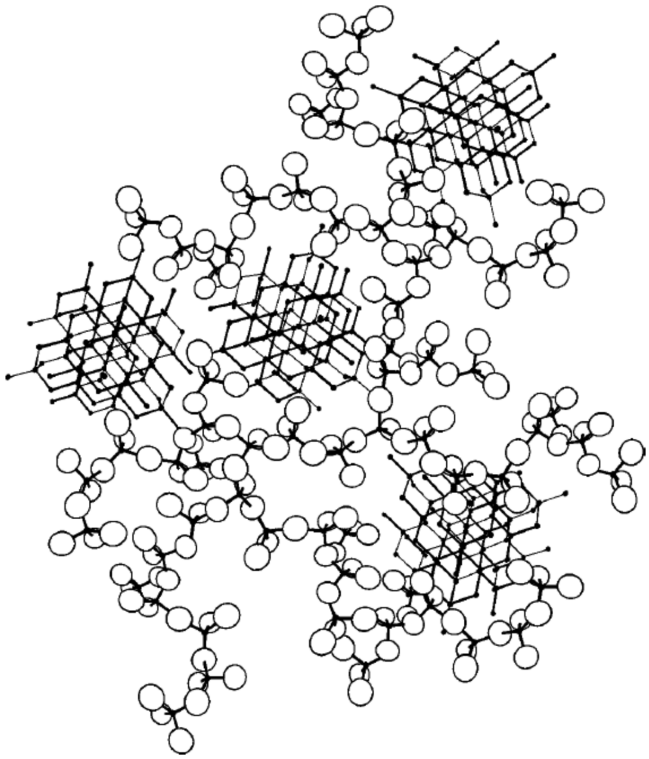


Figure 77. Structure of SiO as proposed by ref 517. O, open circles; Si, closed circles. Reproduced with permission from ref 517. Copyright 2004 The Electrochemical Society.

dx.doi.org/10.1021/cr500207g | Chem. Rev. 2014, 114, 11444−11502

composed of a n-Si phase and a SiO_2 phase that are separated with an interphase boundary layer of unknown stoichiometry that is 20−25 at. % of the entire composition.

Of the above models, the RM model is by far the most favored in recent publications and has been effectively used to explain the lithiation behavior of SiO. Figure 78 shows typical voltage and differential capacity curves of SiO. The reversible capacity of SiO is typically about 1300−1500 mAh/g with a very low initial Coulombic efficiency of about 50%. The lithiation of SiO is thought to progress via the reactions:[399,518−520]

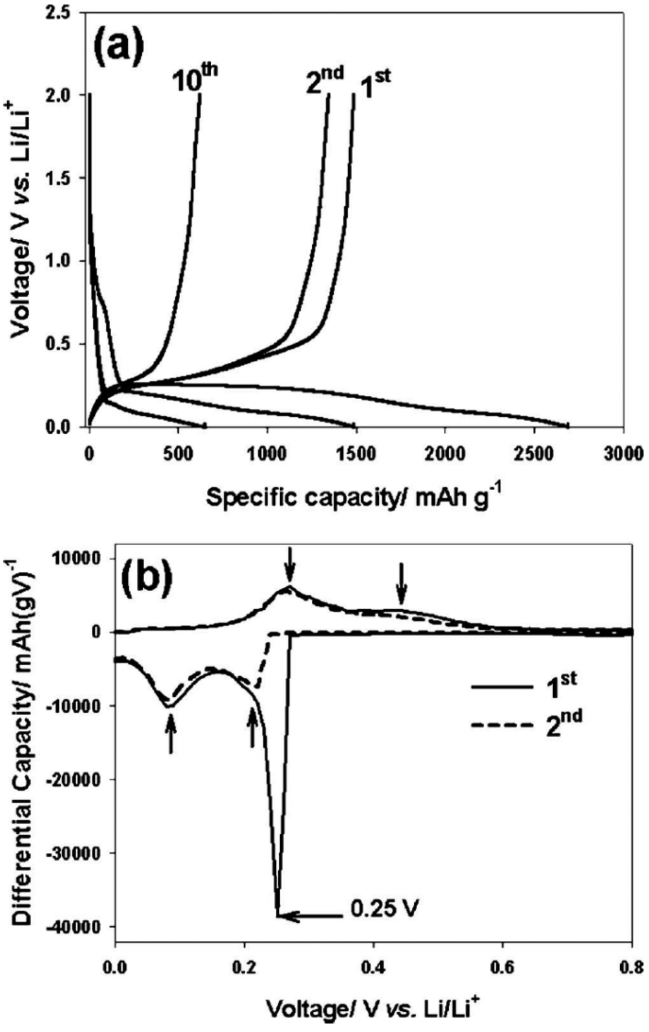


Figure 78. Typical (a) voltage and (b) differential capacity curves of SiO. Reproduced with permission from ref 399. Copyright 2007 The Electrochemical Society.

$$SiO \xrightarrow{Li} 1/4Li_4SiO_4 + 3/4Si \text{ (irreversible)} \quad (42)$$

$$1/4Li_4SiO_4 + 3/4Si \xrightarrow{Li} 1/4Li_4SiO_4 + 3/4Li_{15}Si_4 \text{ (reversible)} \quad (43)$$

Here, the reaction stoichiometry is derived from Al-Maghrabi et al., who proposed that a tie-line exists in the Li−O−Si phase diagram between $Li_{15}Si_4$ and Li_4SiO_4.[518] During reaction 42, an active/inactive alloy is formed in which the active Si phase can be reversibly cycled within the inactive Li_4SiO_4 matrix. The Li_4SiO_4 matrix phase is thought to conduct Li^+ ions and dilutes the active phase, thereby reducing the overall volume expansion. Furthermore, charge transfer at the SiO/electrolyte interface has been found to be exceptionally fast in various electrolytes, and is even significantly faster than graphite.[522]

In agreement with the RM model and reactions 42 and 43, the differential capacity after the first cycle is identical to a-Si, as shown in Figure 78b.[399] In addition, the observed reversible and irreversible capacity predicted from this model fits closely with what is observed for SiO, when lithium consumption from SEI formation is taken into account.[399,517] Recently, Al-Maghrabi et al. have shown this model can be used to accurately explain the reversible and irreversible capacities of the entire $Si_{1-x}O_x$, $0.1 \leq x \leq 0.4$, series.[518] In an interesting study, Kim et al. studied the lithiation of SiO by electrochemical dilatometry. Figure 79 shows the relative height change of a SiO electrode during the first cycle. Initially the expansion is small, corresponding to the initial and irreversible formation of the Li_4SiO_4 matrix. In this phase Li occupies much less volume than in alloys. After the Li_4SiO_4 matrix has been formed, the n-Si phase lithiates, and the now Si/Li_4SiO_4 particle accordingly expands by a greater amount.[399]

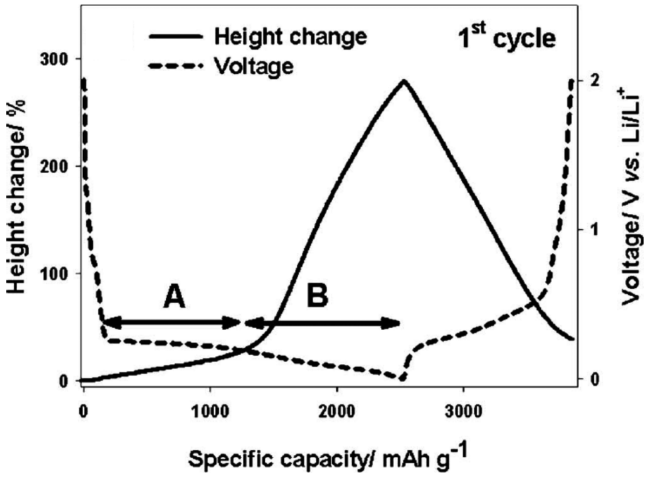


Figure 79. Voltage curve and height change, as measured by electrochemical dilatometry, of a SiO electrode. Reproduced with permission from ref 399. Copyright 2007 The Electrochemical Society.

According to reactions 42 and 43, the theoretical reversible capacity of SiO is about 1710 mAh/g, which is reasonably close to what has been observed. This corresponds to a theoretical volumetric capacity of 1547 Ah/L, with an initial volume expansion of 132% and a reversible volume expansion of 117%, where the reported densities of SiO (2.18 g/mL) and Li_4SiO_4 (2.39 g/mL) by Kim et al.[399] were used. Using the average voltage of Si of 0.4 V, a SiO electrode used in our cell model results in a 853 Wh/L stack energy density or an 18% improvement over a conventional graphite electrode. On this basis, SiO is an excellent candidate for high energy density cells; however, its high irreversible capacity must be somehow resolved for such energy density benefits to be realized.

Many articles have been written on methods to decrease the irreversible capacity and increase the cycling performance of SiO. Yamada et al. showed that cycling performance could be increased dramatically in SiO/carbon composites.[366] Carbon coating these composites significantly reduced the irreversible capacity. Figures 80 and 81 show a SEM image of a composite particle and its cycling performance in full cells, respectively. Besides carbon coating, reductions in irreversible capacity have

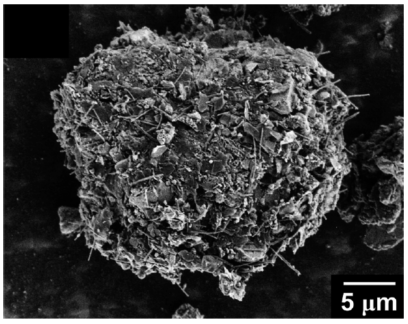


Figure 80. SEM image of a SiO-carbon composite consisting of 50 wt % SiO, 21 wt % graphite, 9 wt % carbon fiber, and 20 wt % carbon coated on the particles. Reproduced with permission from ref 366. Copyright 2011 The Electrochemical Society.

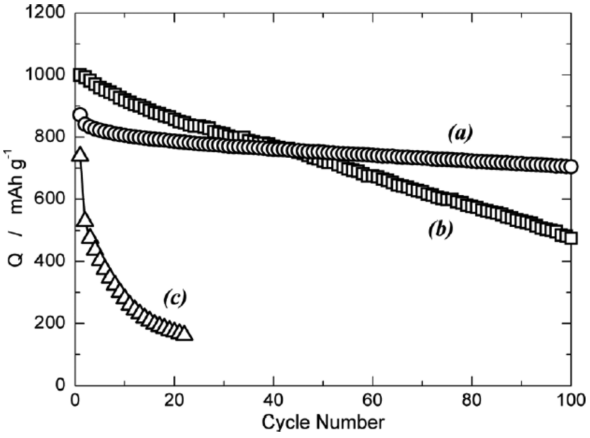


Figure 81. Cycling performance of (a) SiO-carbon composite, (b) carbon-coated SiO/graphite blend, and (C) SiO/graphite blend electrodes cycled in Li-ion full cells as described in ref 366. Reproduced with permission from ref 366. Copyright 2011 The Electrochemical Society.

been achieved by preforming the Li_4SiO_4 phase during synthesis[523] or replacing SiO_2 with inactive Al_2O_3.[319] Miyachi et al. have also reported that doping SiO with transition metal powders can significantly increase the initial Coulombic efficiency: from 50% for SiO to 85% in the case of Fe-doped SiO.[403] Because many of these materials are highly porous, their volumetric capacity, and thus their impact on cell energy density, is impossible to calculate. However, Hitachi has reported an increase in energy from 530 Wh/L $LiCoO_2$/graphite cells to 600 Wh/L $LiCo_{0.05}Mn_{0.025}Mg_{0.025}Ni_{0.9}O_2$ cells with a SiO-based anode.[520]

SiO_2 has also been studied as an environmentally sustainable anode material. Interestingly, ball milled or sputtered SiO_2 has been reported to be active and form $Li_2Si_2O_5$ during lithiation, which can reversibly delithiate back to Si + SiO_2.[524,525]

7.3.3. Si−Metal Alloys. The microstructure and electrochemistry of Si−metal active/inactive alloys have been discussed in section 3.7.2.2. A number of companies have researched Si−metal alloys for Li-ion batteries or are attempting commercialization. Both LG and Samsung SDI have publications focused on Si−metal alloys synthesized by either HEMM or meltspinning.[408,456,482,526−530] 3M has presented at conferences and has published articles on various Si-based metallic alloys. In 2009 Panasonic announced a 4 Ah 18650, which, to our knowledge, has never been commercialized.[531] The patent literature is also rich with examples; however, to our knowledge, optimized coatings for commercial energy cells have only been reported for 3M alloys in the academic literature.

3M authors have reported a "L-19725" alloy made by melt spinning, containing active Si, an inactive Si−Al−Fe phase, and an active Sn_3Mm (Mm = misch metal) phase. XRD patterns indicated the Sn_3Mm phase as being nanocrystalline and the other phases as being amorphous.[512] The Sn_3Mm phase was claimed to aid lithium diffusion within the alloy. Figure 82 shows the cycling performance of this material in an 18650 cell. The cell has impressive cycle life (68% retention after 500 cycles) and a high CE of 99.96%.[512]

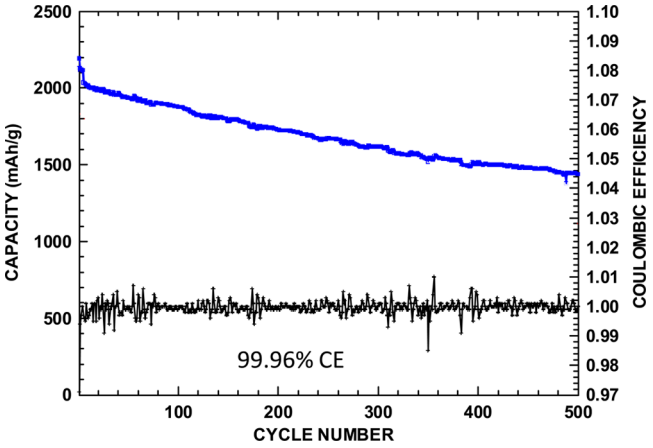


Figure 82. Cycling performance of a 18650 cell containing 3M L-19725 alloy. Reproduced with permission from ref 512. Copyright 2009 M. N. Obrovac.

Recently, a "L-20772 V6" alloy was also reported by 3M as an active/inactive Si-metal alloy.[12] Figure 83 shows the voltage profile and TEM image showing a microstructure consisting of grains less than 15 nm in size. This alloy is reported to have a first lithiation capacity of 1040 mAh/g, and a delithiation capacity of 900 mAh/g (or 1550 Ah/L), corresponding to a first cycle efficiency of 86% to 0.9 V and a volume expansion of 105%.[35] The sloping voltage curve during delithiation indicates that the active Si phase remained amorphous throughout cycling and that $Li_{15}Si_4$ was not formed due to the small grain size (<15 nm) of the active and inactive phases.[12] An average CE of 99.7% was found over cycles 5−60 with 95% retention with respect to the second cycle.[12] This high CE value may be a result of the low alloy surface area of 3.5 m^2/g. In calendered densified composite coatings containing graphite, good cycling characteristics could be achieved, as shown in Figure 70.[35] Such coatings have volumetric full cell energy density (870 Wh/L) and low volume expansion (64%), corresponding to a 13% improvement over graphite coatings.[35]

8. CONCLUDING REMARKS

In this Review, we have attempted to present an overview of alloy anode technology from the viewpoint of cell energy. Such information is scarce, as we have pointed out many times in this Review. Therefore, in embarking on this project, we did not know what we would find. It was very encouraging to find that many advanced alloys can offer about 15−20% improvement in cell energy as compared to graphite. Although alloy anode technology has had false starts, the amount of progress made every year in this field is astounding. With proper binder,

dx.doi.org/10.1021/cr500207g | Chem. Rev. 2014, 114, 11444−11502

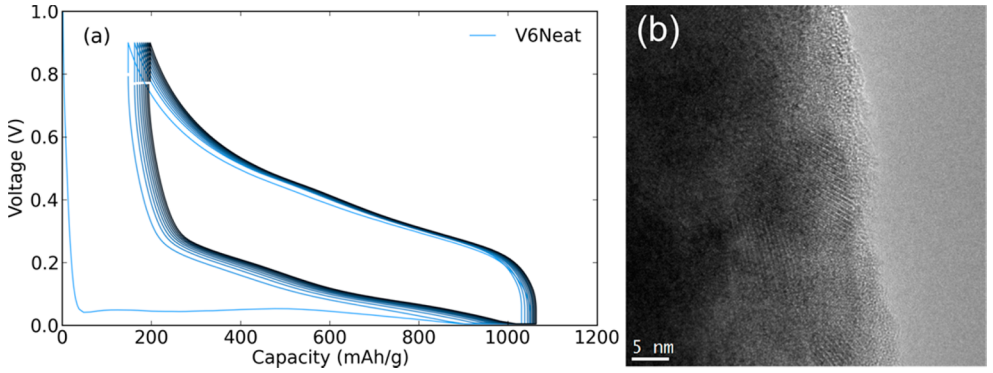


Figure 83. (a) Voltage curve of 3M L-20772 V6 alloy in a 91 wt % alloy, 9 wt % LiPAA electrode cycled at a C/4 rate. The first 10 cycles are shown. (b) TEM image of the 3M L-20772 V6 alloy showing grain sizes less than 15 nm. Reproduced with permission from ref 12. Copyright 2014 The Electrochemical Society.

electrolyte formulation, and coating design, alloys have been shown to cycle hundreds of times in high energy density full cells. This paints a bright future for the implementation of alloy materials in commercial cells. However, we have found that there is a lack of sufficient information to estimate the impact on cell energy of many important alloys. We have even found some "high capacity" alloys that will result in a reduced cell energy as compared to conventional graphite coatings. To ensure further progress in this field, we hope the research community will more universally adopt metrics that make sense for increasing cell energy.

AUTHOR INFORMATION

Corresponding Author

*E-mail: mark.obrovac@dal.ca.

Notes

The authors declare no competing financial interest.

Biographies



Mark Obrovac received his B.Sc. in Chemical Physics from Simon Fraser University in 1995. During this time he worked as an undergraduate researcher at Moli Energy (1990) Ltd., Bluestar Battery Systems, and Ballard Fuel Cells. He obtained his Ph.D. in Physics, researching nanocomposite lithium ion battery materials, under the supervision of Professor Jeff Dahn at Dalhousie University in 2001. He then studied inorganic chemical synthesis for one year as a postdoctoral fellow in Chemistry at Cornell University under the direction of Professor Frank DiSalvo. In 2002 he joined 3M Company where he became project leader for the development of Si alloy anode materials for Li-ion batteries. In 2010 he joined Dalhousie University, where he is currently an Associate Professor in Chemistry and Physics, and 3M/NSERC Industrial Research Chair in Metal-Ion Batteries.



Vincent Chevrier's introduction to alloy anodes for Li-ion batteries was as an undergraduate working in Prof. Jeff Dahn's lab, Dalhousie University (NS, Canada), in 2003. He obtained his B.Sc. in physics at the University of Ottawa (ON, Canada) in 2004 and subsequently joined Prof. Dahn's group in 2004. In 2006 he completed an M.Sc. focused on sputtered combinatorial quaternary alloy libraries, and in 2009 he completed a Ph.D. focusing on computational and experimental studies of Si for Li-ion batteries. He continued on to MIT (MA, U.S.A.) as a postdoctoral fellow under Prof. Gerbrand Ceder, studying a range of topics including Na-ion battery materials and Li-ion conversion cathodes. Since 2010, Vincent has been working for 3M on the optimization, scale up, and commercialization of alloy anodes for Li-ion batteries.

ACKNOWLEDGMENTS

We thank our families for the considerable support they provided during the preparation of this manuscript. V.L.C. thanks Prof. Jeff Dahn for useful discussions. We also thank Prof. Stanley Whittingham for giving us the opportunity to contribute to this issue. M.N.O. acknowledges funding from NSERC and 3M Canada, Co., under the auspices of the Discovery Grants and Industrial Research Chair programs.

REFERENCES

(1) Whittingham, M. S. *Proc. IEEE* **2012**, *100*, 1518.
(2) Gallagher, K. G.; Goebel, S.; Greszler, T.; Mathias, M.; Oelerich, W.; Eroglu, D.; Srinivasan, V. *Energy Environ. Sci.* **2014**.
(3) Kim, H.; Choi, J.; Sohn, J.-J.; Kang, T. *J. Electrochem. Soc.* **1999**, *146*, 4401.

(4) Beaulieu, L. Y.; Hewitt, K. C.; Turner, R. L.; Bonakdarpour, A.; Abdo, A. A.; Christensen, L.; Eberman, K. W.; Krause, L. J.; Dahn, J. R. *J. Electrochem. Soc.* **2003**, *150*, A149.
(5) Fleischauer, M. D.; Obrovac, M. N.; Dahn, J. R. *J. Electrochem. Soc.* **2008**, *155*, A851.
(6) Xu, Y.; Liu, Q.; Zhu, Y.; Liu, Y.; Langrock, A.; Zachariah, M. R.; Wang, C. *Nano Lett.* **2013**, *13*, 470.
(7) Wang, Y.; Wu, M.; Jiao, Z.; Lee, J. Y. *Chem. Mater.* **2009**, *21*, 3210.
(8) Vaughey, J. T.; Thackeray, M. M.; Shin, D.; Wolverton, C. *J. Electrochem. Soc.* **2009**, *156*, A536.
(9) Idota, Y. *Science* **1997**, *276*, 1395.
(10) Ferguson, P.; Todd, A.; Dahn, J. *Electrochem. Commun.* **2008**, *10*, 25.
(11) Liu, N.; Lu, Z.; Zhao, J.; McDowell, M. T.; Lee, H.-W.; Zhao, W.; Cui, Y. *Nat. Nanotechnol.* **2014**, *9*, 187.
(12) Chevrier, V. L.; Liu, L.; Le, D. B.; Lund, J.; Molla, B.; Reimer, K.; Krause, L. J.; Jensen, L. D.; Figgemeier, E.; Eberman, K. W. *J. Electrochem. Soc.* **2014**, *161*, A783.
(13) McDowell, M. T.; Lee, S. W.; Nix, W. D.; Cui, Y. *Adv. Mater.* **2013**, *25*, 4966.
(14) Zhang, W.-J. *J. Power Sources* **2011**, *196*, 13.
(15) Zhang, W.-J. *J. Power Sources* **2011**, *196*, 877.
(16) Park, C.-M.; Kim, J.-H.; Kim, H.; Sohn, H.-J. *Chem. Soc. Rev.* **2010**, *39*, 3115.
(17) Larcher, D.; Beattie, S.; Morcrette, M.; Edström, K.; Jumas, J.-C.; Tarascon, J.-M. *J. Mater. Chem.* **2007**, *17*, 3759.
(18) Kasavajjula, U.; Wang, C.; Appleby, A. J. *J. Power Sources* **2007**, *163*, 1003.
(19) Huggins, R. A. *J. Power Sources* **1999**, *81*−*82*, 13.
(20) Besenhard, J. O.; Yang, J.; Winter, M. *J. Power Sources* **1997**, *68*, 87.
(21) Winter, M.; Besenhard, J. O. *Electrochim. Acta* **1999**, *45*, 31.
(22) Liang, B.; Liu, Y.; Xu, Y. *J. Power Sources* **2014**, *267*, 469.
(23) Obrovac, M. N.; Christensen, L.; Le, D. B.; Dahn, J. R. *J. Electrochem. Soc.* **2007**, *154*, A849.
(24) Zheng, H.; Li, J.; Song, X.; Liu, G.; Battaglia, V. S. *Electrochim. Acta* **2012**, *71*, 258.
(25) Kim, H.; Park, B.; Sohn, H.-J.; Kang, T. *J. Power Sources* **2000**, *90*, 59.
(26) Taillades, G.; Sarradin, J. *J. Power Sources* **2004**, *125*, 199.
(27) Hwa, Y.; Sung, J. H.; Wang, B.; Park, C.-M.; Sohn, H.-J. *J. Mater. Chem.* **2012**, *22*, 12767.
(28) Wang, J.; King, P.; Huggins, R. A. *Solid State Ionics* **1986**, *20*, 185.
(29) Jow, T. R.; Liang, C. C. *J. Electrochem. Soc.* **1982**, *129*, 7.
(30) Purcell, M. I.; Hatchard, T. D.; Sanderson, R. J.; Obrovac, M. N. *J. Electrochem. Soc.* **2014**, *161*, A643.
(31) Tian, Y.; Timmons, A.; Dahn, J. R. *J. Electrochem. Soc.* **2009**, *156*, A187.
(32) Baggetto, L.; Niessen, R. A. H.; Roozeboom, F.; Notten, P. H. L. *Adv. Funct. Mater.* **2008**, *18*, 1057.
(33) Wang, J.; Raistrick, I. D.; Huggins, R. A. *J. Electrochem. Soc.* **1986**, *133*, 457.
(34) Tirado, J. L. *Mater. Sci. Eng., R* **2003**, *40*, 103.
(35) Du, Z.; Dunlap, R. A.; Obrovac, M. N. *J. Electrochem. Soc.* **2014**, *161*, A1698.
(36) Oumellal, Y.; Rougier, A.; Nazri, G. A.; Tarascon, J.-M.; Aymard, L. *Nat. Mater.* **2008**, *7*, 916.
(37) Oumellal, Y.; Rougier, A.; Tarascon, J.-M.; Aymard, L. *J. Power Sources* **2009**, *192*, 698.
(38) Zaïdi, W.; Oumellal, Y.; Bonnet, J.-P.; Zhang, J.; Cuevas, F.; Latroche, M.; Bobet, J.-L.; Aymard, L. *J. Power Sources* **2011**, *196*, 2854.
(39) Park, C.-M.; Kim, Y.-U.; Kim, H.; Sohn, H.-J. *J. Power Sources* **2006**, *158*, 1451.
(40) Massalski, T. B.; Okamoto, H.; Subramanian, P. R.; Kacprzak, L. *Binary Alloy, Phase Diagrams*, 2nd ed. plus updates [CD-ROM]; ASM International: Materials Park, OH, 1996.
(41) Lu, Z.; Schechter, A.; Moshkovich, M.; Aurbach, D. *J. Electroanal. Chem.* **1999**, *466*, 203.
(42) Wolfenstine, J. *J. Power Sources* **2003**, *124*, 241.
(43) Yu, P.; Haran, B. S.; Ritter, J. a.; White, R. E.; Popov, B. N. *J. Power Sources* **2000**, *91*, 107.
(44) Huggins, R. *J. Power Sources* **1988**, *22*, 341.
(45) Kulikova, L. N.; Volgin, M. A.; L'vov, A. L. *Russ. J. Electrochem.* **2005**, *41*, 620.
(46) Dey, A. *J. Electrochem. Soc.* **1971**, *118*, 1547.
(47) Park, S. H.; Winnick, J.; Kohl, P. A. *J. Electrochem. Soc.* **2002**, *149*, A1196.
(48) Awaludin, Z.; Okajima, T.; Ohsaka, T. *Electrochem. Commun.* **2013**, *31*, 100.
(49) Taillades, G.; Benjelloun, N.; Sarradin, J.; Ribes, M. *Solid State Ionics* **2002**, *c*, 119.
(50) Yuan, L.; Liu, H.; Maaroof, A.; Konstantinov, K.; Liu, J.; Cortie, M. *J. New Mater. Electrochem. Syst.* **2007**, *99*, 95.
(51) Renner, F. U.; Kageyama, H.; Siroma, Z.; Shikano, M.; Schöder, S.; Gründer, Y.; Sakata, O. *Electrochim. Acta* **2008**, *53*, 6064.
(52) Viudez, A.; Blázquez, M.; Madueno, R.; Morales, J.; Pineda, T.; Sanchez, L. *J. Phys. Chem. C* **2010**, *114*, 2360.
(53) Deutscher, R.; Florence, T.; Woods, R. *J. Power Sources* **1995**, *55*, 41.
(54) Park, C.-M.; Jung, H.; Sohn, H.-J. *Electrochem. Solid-State Lett.* **2009**, *12*, A171.
(55) Fujieda, T.; Takahashi, S.; Higuchi, S. *J. Power Sources* **1992**, *40*, 283.
(56) Saint, J.; Morcrette, M.; Larcher, D.; Tarascon, J. *Solid State Ionics* **2005**, *176*, 189.
(57) Lee, K. T.; Jung, Y. S.; Kim, T.; Kim, C. H.; Kim, J. H.; Kwon, J. Y.; Oh, S. M. *Electrochem. Solid-State Lett.* **2008**, *11*, A21.
(58) Deshpande, R. D.; Li, J.; Cheng, Y.-T.; Verbrugge, M. W. *J. Electrochem. Soc.* **2011**, *158*, A845.
(59) Vaughey, J.; Johnson, C.; Kropf, A. *J. Power Sources* **2001**, *98*, 194.
(60) Ho, W.-H.; Li, C.-F.; Liu, H.-C.; Yen, S.-K. *J. Power Sources* **2008**, *175*, 897.
(61) Chen, J.; Zhao, H.; Chen, N.; Wang, X.; Wang, J.; Zhang, R.; Jin, C. *J. Power Sources* **2011**, *200*, 98.
(62) Zhao, X. B.; Cao, G. S.; Lv, C. P.; Zhang, L. J.; Hu, S. H.; Zhu, T. J.; Zhou, B. C. *J. Alloys Compd.* **2001**, *315*, 265.
(63) Netz, A.; Huggins, R.; Weppner, W. *Ionics* **2001**, *7*, 433.
(64) Borgstedt, H. B.; Gumin, C. *J. Phase Equilib.* **2003**, *24*, 572.
(65) Albert, B. *Eur. J. Inorg. Chem.* **2000**, 1679.
(66) Devries, L. E.; Jackson, L. D.; James, S. D. *J. Electrochem. Soc.* **1979**, *126*, 993.
(67) Sanchez, P.; Belin, C.; Crepy, G.; Guibert, A. De. *J. Mater. Sci.* **1992**, *27*, 240.
(68) James, S.; DeVries, L. *J. Electrochem. Soc.* **1979**, *123*, 321.
(69) Mcmonis, G. E.; Miles, M. H.; Fletcher, A. N. *J. Electrochem. Soc.* **1984**, *131*, 286.
(70) Dallek, S.; Ernst, D. W.; Larrick, B. F. *J. Electrochem. Soc.* **1979**, *126*, 866.
(71) Szwarc, R.; Walton, R. D.; Dallek, S.; Larrick, B. F. *J. Electrochem. Soc.* **1982**, *129*, 1168.
(72) Ding, X.; Lu, X.; Fu, Z.; Li, H. *Electrochim. Acta* **2013**, *87*, 230.
(73) Limthongkul, P.; Jang, Y.-I.; Dudney, N. J.; Chiang, Y.-M. *Acta Mater.* **2003**, *51*, 1103.
(74) Hudak, N. S.; Huber, D. L. *J. Electrochem. Soc.* **2012**, *159*, A688.
(75) Frazer, E. *J. Electroanal. Chem. Interfacial Electrochem.* **1981**, *121*, 329.
(76) Okamoto, H. *J. Phase Equilib. Diffus.* **2012**, *33*, 500.
(77) Wen, C. J.; Boukamp, B. A.; Huggins, R. A. *J. Electrochem. Soc.* **1979**, *126*, 2258.
(78) Dahn, J. R.; Mar, R. E.; Abouzeid, A. *J. Electrochem. Soc.* **2006**, *153*, A361.
(79) Subramanian, V.; Karabacak, T.; Masarapu, C.; Teki, R.; Lu, T.-M.; Wei, B. *J. Power Sources* **2010**, *195*, 2044.
(80) Kulova, T. L.; Evstefeeva, Y. E.; Pleskov, Y. V.; Skundin, A. M.; Ral'chenko, V. G.; Korchagina, S. B.; Gordeev, S. K. *Phys. Solid State* **2004**, *46*, 726.
(81) Ferreira, N.; Mendonça, L. *Diamond Relat. Mater.* **2003**, *12*, 596.

(82) Christy, A. Y. M. T.; Nahm, K. S.; Hwang, Y. J.; Suh, E. K.; Kulandainathan, M. A.; Premkumar, T.; Stephan, A. M. *Ionics* **2007**, *14*, 157.
(83) Obrovac, M. N.; Christensen, L. *Electrochem. Solid-State Lett.* **2004**, *7*, A93.
(84) Li, J.; Dahn, J. R. *J. Electrochem. Soc.* **2007**, *154*, A156.
(85) Courtney, I.; Tse, J.; Mao, O.; Hafner, J.; Dahn, J. *Phys. Rev. B* **1998**, *58*, 15583.
(86) Goward, G. R.; Taylor, N. J.; Nazar, L. F. *J. Alloys Compd.* **2001**, *329*, 82.
(87) Lupu, C.; Mao, J.; Rabalais, J. *Inorg. Chem.* **2003**, *42*, 2943.
(88) Dahn, J.; Courtney, I.; Mao, O. *Solid State Ionics* **1998**, *111*, 289.
(89) Courtney, I.; Dahn, J. *J. Electrochem. Soc.* **1997**, *144*, 2045.
(90) Chouvin, J.; Olivier-Fourcade, J.; Jumas, J. C.; Simon, B.; Godiveau, O. *Chem. Phys. Lett.* **1999**, *308*, 413.
(91) Dunlap, R. A.; Small, D. A.; MacNeil, D. D.; Obrovac, M. N.; Dahn, J. R. *J. Alloys Compd.* **1999**, *289*, 135.
(92) Robert, F.; Lippens, P. E.; Olivier-Fourcade, J.; Jumas, J.-C.; Gillot, F.; Morcrette, M.; Tarascon, J.-M. *J. Solid State Chem.* **2007**, *180*, 339.
(93) Courtney, I. A.; Dunlap, R.; Dahn, J. . *Electrochim. Acta* **1999**, *45*, 51.
(94) Jolly, R.; Rhin, C. *Resour., Conserv. Recycl.* **1994**, *10*, 137.
(95) Martos, M.; Morales, J.; Sanchez, L. *Electrochim. Acta* **2003**, *48*, 615.
(96) Hewitt, K. C.; Beaulieu, L. Y.; Dahn, J. R. *J. Electrochem. Soc.* **2001**, *148*, A402.
(97) Baggetto, L.; Ganesh, P.; Sun, C.-N.; Meisner, R. A.; Zawodzinski, T. A.; Veith, G. M. *J. Mater. Chem. A* **2013**, *1*, 7985.
(98) Xianming, W.; Nishina, T.; Uchida, I. *J. Power Sources* **2002**, *104*, 90.
(99) Besenhard, J.; Hess, M.; Komenda, P. *Solid State Ionics* **1990**, *40/41*, 525.
(100) Beaulieu, L. Y.; Hatchard, T. D.; Bonakdarpour, A.; Fleischauer, M. D.; Dahn, J. R. *J. Electrochem. Soc.* **2003**, *150*, A1457.
(101) Besenhard, J. O.; Komenda, P.; Paxinos, A.; Wudy, E.; Josowicz, M. *Solid State Ionics* **1986**, *18−19*, 823.
(102) Thomas, K. E.; Newman, J. *Electrochem. Soc. Proc.* **2001**, *2001−21*, 327.
(103) Komaba, S.; Yabuuchi, N.; Ozeki, T.; Han, Z.; Shimomura, K.; Yui, H.; Katayama, Y.; Miura, T. *J. Phys. Chem. C* **2012**, *116*, 1380.
(104) Rhodes, K.; Dudney, N.; Lara-Curzio, E.; Daniel, C. *J. Electrochem. Soc.* **2010**, *157*, A1354.
(105) Tran, T. T.; Obrovac, M. N. *J. Electrochem. Soc.* **2011**, *158*, A1411.
(106) Timmons, A.; Dahn, J. R. *J. Electrochem. Soc.* **2007**, *154*, A444.
(107) Lee, S. W.; McDowell, M. T.; Choi, J. W.; Cui, Y. *Nano Lett.* **2011**, *11*, 3034.
(108) Chao, S.-C.; Song, Y.-F.; Wang, C.-C.; Sheu, H.-S.; Wu, H.-C.; Wu, N.-L. *J. Phys. Chem. C* **2011**, *115*, 22040.
(109) Chen, Q.; Sieradzki, K. *Nat. Mater.* **2013**, *12*, 1102.
(110) Pharr, M.; Suo, Z.; Vlassak, J. J. *Nano Lett.* **2013**, *13*, 5570.
(111) Beaulieu, L. Y.; Eberman, K. W.; Turner, R. L.; Krause, L. J.; Dahn, J. R. *Electrochem. Solid-State Lett.* **2001**, *4*, A137.
(112) Maranchi, J. P.; Hepp, A. F.; Evans, A. G.; Nuhfer, N. T.; Kumta, P. N. *J. Electrochem. Soc.* **2006**, *153*, A1246.
(113) Maranchi, J. P.; Hepp, A. F.; Kumta, P. N. *Electrochem. Solid-State Lett.* **2003**, *6*, A198.
(114) Liu, X. H.; Zhong, L.; Huang, S.; Mao, S. X.; Zhu, T.; Huang, J. Y. *ACS Nano* **2012**, *6*, 1522.
(115) Chon, M. J.; Sethuraman, V. A.; McCormick, A.; Srinivasan, V.; Guduru, P. R. *Phys. Rev. Lett.* **2011**, *107*, 045503.
(116) Zhao, K.; Pharr, M.; Wan, Q.; Wang, W. L.; Kaxiras, E.; Vlassak, J. J.; Suo, Z. *J. Electrochem. Soc.* **2012**, *159*, A238.
(117) Cui, L.-F.; Ruffo, R.; Chan, C. K.; Peng, H.; Cui, Y. *Nano Lett.* **2009**, *9*, 491.
(118) Nguyen, H. T.; Yao, F.; Zamfir, M. R.; Biswas, C.; So, K. P.; Lee, Y. H.; Kim, S. M.; Cha, S. N.; Kim, J. M.; Pribat, D. *Adv. Energy Mater.* **2011**, *1*, 1154.
(119) Courtney, I. A.; Dahn, J. *J. Electrochem. Soc.* **1997**, *144*, 2943.
(120) Hatchard, T. D.; Obrovac, M. N.; Dahn, J. R. *J. Electrochem. Soc.* **2006**, *153*, A282.
(121) Hatchard, T. D.; Topple, J. M.; Fleischauer, M. D.; Dahn, J. R. *Electrochem. Solid-State Lett.* **2003**, *6*, A129.
(122) Maxfield, M.; Jow, T. R.; Sewchok, M. G.; Shacklette, L. W. *J. Power Sources* **1989**, *26*, 93.
(123) Xun, S.; Song, X.; Battaglia, V.; Liu, G. *J. Electrochem. Soc.* **2013**, *160*, A849.
(124) Bryngelsson, H.; Eskhult, J.; Nyholm, L.; Herranen, M.; Alm, O.; Edström, K. *Chem. Mater.* **2007**, *19*, 1170.
(125) Besenhard, J.; Komenda, P.; Paxinos, A.; Wudy, E.; Josowicz, M. *Solid State Ionics* **1986**, *18−19*, 823.
(126) Aydinol, M.; Kohan, A.; Ceder, G.; Cho, K.; Joannopoulos, J. *Phys. Rev. B* **1997**, *56*, 1354.
(127) Kohn, W.; Sham, L. J. *Phys. Rev.* **1965**, *140*, A1133.
(128) Kresse, G. *Phys. Rev. B* **1996**, *54*, 11169.
(129) Clark, S. J.; Segall, M. D.; Pickard, C. J.; Hasnip, P. J.; Probert, M. I. J.; Refson, K.; Payne, M. C. *Z. Kristallogr.* **2005**, *220*, 567.
(130) Gonze, X.; Amadon, B.; Anglade, P.-M.; Beuken, J.-M.; Bottin, F.; Boulanger, P.; Bruneval, F.; Caliste, D.; Caracas, R.; Côté, M.; Deutsch, T.; Genovese, L.; Ghosez, P.; Giantomassi, M.; Goedecker, S.; Hamann, D. R.; Hermet, P.; Jollet, F.; Jomard, G.; Leroux, S.; Mancini, M.; Mazevet, S.; Oliveira, M. J. T.; Onida, G.; Pouillon, Y.; Rangel, T.; Rignanese, G.-M.; Sangalli, D.; Shaltaf, R.; Torrent, M.; Verstraete, M. J.; Zerah, G.; Zwanziger, J. W. *Comput. Phys. Commun.* **2009**, *180*, 2582.
(131) Giannozzi, P.; Baroni, S.; Bonini, N.; Calandra, M.; Car, R.; Cavazzoni, C.; Ceresoli, D.; Chiarotti, G. L.; Cococcioni, M.; Dabo, I.; Dal Corso, A.; de Gironcoli, S.; Fabris, S.; Fratesi, G.; Gebauer, R.; Gerstmann, U.; Gougoussis, C.; Kokalj, A.; Lazzeri, M.; Martin-Samos, L.; Marzari, N.; Mauri, F.; Mazzarello, R.; Paolini, S.; Pasquarello, A.; Paulatto, L.; Sbraccia, C.; Scandolo, S.; Sclauzero, G.; Seitsonen, A. P.; Smogunov, A.; Umari, P.; Wentzcovitch, R. M. *J. Phys.: Condens. Matter* **2009**, *21*, 395502.
(132) Nesper, R. *Prog. Solid State Chem.* **1990**, *20*, 1.
(133) Chevrier, V. L.; Zwanziger, J. W.; Dahn, J. R. *J. Alloys Compd.* **2010**, *496*, 25.
(134) Chevrier, V.; Ong, S.; Armiento, R.; Chan, M.; Ceder, G. *Phys. Rev. B* **2010**, *82*, 1.
(135) Perdew, J. P. *Phys. Rev. B* **1981**, *23*, 5048.
(136) Perdew, J. P.; Burke, K.; Ernzerhof, M. *Phys. Rev. Lett.* **1996**, *77*, 3865.
(137) Troullier, N.; Martins, J. L. *Phys. Rev. B* **1991**, *43*, 1993.
(138) Vanderbilt, D. *Phys. Rev. B* **1990**, *41*, 7892.
(139) Blöchl, P. E. *Phys. Rev. B* **1994**, *50*, 17953.
(140) Chevrier, V. L.; Zwanziger, J. W.; Dahn, J. R. *Can. J. Phys.* **2009**, *87*, 625.
(141) Wen, C. J.; Huggins, R. *J. Solid State Chem.* **1981**, *37*, 271.
(142) Limthongkul, P.; Jang, Y.-I.; Dudney, N. J.; Chiang, Y.-M. *Acta Mater.* **2003**, *51*, 1103.
(143) Chevrier, V. L.; Dahn, J. R. *J. Electrochem. Soc.* **2009**, *156*, A454.
(144) Chevrier, V. L.; Dahn, J. R. *J. Electrochem. Soc.* **2010**, *157*, A392.
(145) Zhang, Q.; Cui, Y.; Wang, E. *Model. Simul. Mater. Sci. Eng.* **2013**, *21*, 074001.
(146) Baggetto, L.; Niessen, R. A. H.; Roozeboom, F.; Notten, P. H. L. *Adv. Funct. Mater.* **2008**, *18*, 1057.
(147) Zhang, W.-J. *J. Power Sources* **2011**, *196*, 877.
(148) Sethuraman, V. A.; Srinivasan, V.; Newman, J. *J. Electrochem. Soc.* **2013**, *160*, A394.
(149) Sethuraman, V. A.; Srinivasan, V.; Bower, A. F.; Guduru, P. R. *J. Electrochem. Soc.* **2010**, *157*, A1253.
(150) Jain, A.; Ong, S. P.; Hautier, G.; Chen, W.; Richards, W. D.; Dacek, S.; Cholia, S.; Gunter, D.; Skinner, D.; Ceder, G.; Persson, K. A. *APL Mater.* **2013**, *1*, 011002.
(151) Curtarolo, S.; Setyawan, W.; Wang, S.; Xue, J.; Yang, K.; Taylor, R. H.; Nelson, L. J.; Hart, G. L. W.; Sanvito, S.; Buongiorno-Nardelli, M.; Mingo, N.; Levy, O. *Comput. Mater. Sci.* **2012**, *58*, 227.
(152) Kirklin, S.; Meredig, B.; Wolverton, C. *Adv. Energy Mater.* **2013**, *3*, 252.

(153) Sharma, R. A.; Seefurth, R. N. *J. Electrochem. Soc.* **1976**, *123*, 1763.
(154) Wilson, A. M.; Dahn, J. R. *J. Electrochem. Soc.* **1995**, *142*, 326.
(155) Key, B.; Bhattacharyya, R.; Morcrette, M.; Seznéc, V.; Tarascon, J.-M.; Grey, C. P. *J. Am. Chem. Soc.* **2009**, *131*, 9239.
(156) Li, J.; Smith, A.; Sanderson, R. J.; Hatchard, T. D.; Dunlap, R. A.; Dahn, J. R. *J. Electrochem. Soc.* **2009**, *156*, A283.
(157) Rhodes, K.; Dudney, N.; Lara-Curzio, E.; Daniel, C. *J. Electrochem. Soc.* **2010**, *157*, A1354.
(158) Liu, X. H.; Wang, J. W.; Huang, S.; Fan, F.; Huang, X.; Liu, Y.; Krylyuk, S.; Yoo, J.; Dayeh, S. a.; Davydov, A. V.; Mao, S. X.; Picraux, S. T.; Zhang, S.; Li, J.; Zhu, T.; Huang, J. Y. *Nat. Nanotechnol.* **2012**, *7*, 749.
(159) Liu, X. H.; Huang, J. Y. *Energy Environ. Sci.* **2011**, *4*, 3844.
(160) Chan, M. K. Y.; Wolverton, C.; Greeley, J. P. *J. Am. Chem. Soc.* **2012**, *134*, 14362.
(161) Obrovac, M. N.; Krause, L. J. *J. Electrochem. Soc.* **2007**, *154*, A103.
(162) Gu, M.; Wang, Z.; Connell, J. G.; Perea, D. E.; Lauhon, L. J.; Gao, F.; Wang, C. *ACS Nano* **2013**, *7*, 6303.
(163) Hatchard, T. D.; Dahn, J. R. *J. Electrochem. Soc.* **2004**, *151*, A838.
(164) Wang, Y.; Dahn, J. R. *Electrochem. Solid-State Lett.* **2006**, *9*, A340.
(165) Chevrier, V. L.; Dahn, H. M.; Dahn, J. R. *J. Electrochem. Soc.* **2011**, *158*, A1207.
(166) McDowell, M. T.; Lee, S. W.; Harris, J. T.; Korgel, B. a.; Wang, C.; Nix, W. D.; Cui, Y. *Nano Lett.* **2013**, *13*, 758.
(167) Gauthier, M.; Mazouzi, D.; Reyter, D.; Lestriez, B.; Moreau, P.; Guyomard, D.; Roué, L. *Energy Environ. Sci.* **2013**, *6*, 2145.
(168) Szczech, J. R.; Jin, S. *Energy Environ. Sci.* **2011**, *4*, 56.
(169) Wu, H.; Cui, Y. *Nano Today* **2012**, *7*, 414.
(170) Su, X.; Wu, Q.; Li, J.; Xiao, X.; Lott, A.; Lu, W.; Sheldon, B. W.; Wu, J. *Adv. Energy Mater.* **2014**, *4*, 1.
(171) Li, H. *Electrochem. Solid-State Lett.* **1999**, *2*, 547.
(172) Li, H.; Huang, X.; Chen, L.; Zhou, G.; Zhang, Z.; Yu, D.; Jun, Mo. Y.; Pei, N. *Solid State Ionics* **2000**, *135*, 181.
(173) Graetz, J.; Ahn, C. C.; Yazami, R.; Fultz, B. *Electrochem. Solid-State Lett.* **2003**, *6*, A194.
(174) Holzapfel, M.; Buqa, H.; Scheifele, W.; Novák, P.; Petrat, F.-M. *Chem. Commun.* **2005**, 1566.
(175) Guo, Z. P.; Wang, J. Z.; Liu, H. K.; Dou, S. X. *J. Power Sources* **2005**, *146*, 448.
(176) Beattie, S. D.; Larcher, D.; Morcrette, M.; Simon, B.; Tarascon, J.-M. *J. Electrochem. Soc.* **2008**, *155*, A158.
(177) Bridel, J.-S.; Azaïs, T.; Morcrette, M.; Tarascon, J.-M.; Larcher, D. *Chem. Mater.* **2010**, *22*, 1229.
(178) Oumellal, Y.; Delpuech, N.; Mazouzi, D.; Dupré, N.; Gaubicher, J.; Moreau, P.; Soudan, P.; Lestriez, B.; Guyomard, D. *J. Mater. Chem.* **2011**, *21*, 6201.
(179) McDowell, M. T.; Ryu, I.; Lee, S. W.; Wang, C.; Nix, W. D.; Cui, Y. *Adv. Mater.* **2012**, *24*, 6034.
(180) Liu, X. H.; Zhong, L.; Huang, S.; Mao, S. X.; Zhu, T.; Huang, J. Y. *ACS Nano* **2012**, *6*, 1522.
(181) Liu, N.; Huo, K.; McDowell, M. T.; Zhao, J.; Cui, Y. *Sci. Rep.* **2013**, *3*, 1919.
(182) Holzapfel, M.; Buqa, H.; Krumeich, F.; Novák, P.; Petrat, F.-M.; Veit, C. *Electrochem. Solid-State Lett.* **2005**, *8*, A516.
(183) Laïk, B.; Eude, L.; Pereira-Ramos, J.-P.; Cojocaru, C. S.; Pribat, D.; Rouvière, E. *Electrochim. Acta* **2008**, *53*, 5528.
(184) Chan, C. K.; Peng, H.; Liu, G.; McIlwrath, K.; Zhang, X. F.; Huggins, R. a; Cui, Y. *Nat. Nanotechnol.* **2008**, *3*, 31.
(185) Chan, C. K.; Ruffo, R.; Hong, S. S.; Huggins, R. A.; Cui, Y. *J. Power Sources* **2009**, *189*, 34.
(186) Ruffo, R.; Hong, S. S.; Chan, C. K.; Huggins, R. A.; Cui, Y. *J. Phys. Chem. C* **2009**, *113*, 11390.
(187) Chan, C. K.; Patel, R. N.; O'Connell, M. J.; Korgel, B. a.; Cui, Y. *ACS Nano* **2010**, *4*, 1443.
(188) Ryu, I.; Choi, J. W.; Cui, Y.; Nix, W. D. *J. Mech. Phys. Solids* **2011**, *59*, 1717.
(189) Liu, N.; Hu, L.; McDowell, M. T.; Jackson, A.; Cui, Y. *ACS Nano* **2011**, *5*, 6487.
(190) Etacheri, V.; Haik, O.; Goffer, Y.; Roberts, G. a; Stefan, I. C.; Fasching, R.; Aurbach, D. *Langmuir* **2012**, *28*, 965.
(191) Song, T.; Xia, J.; Lee, J.-H.; Lee, D. H.; Kwon, M.-S.; Choi, J.-M.; Wu, J.; Doo, S. K.; Chang, H.; Park, W.; Il Zang, D. S.; Kim, H.; Huang, Y.; Hwang, K.-C.; Rogers, J. a; Paik, U. *Nano Lett.* **2010**, *10*, 1710.
(192) Park, M.-H.; Kim, M. G.; Joo, J.; Kim, K.; Kim, J.; Ahn, S.; Cui, Y.; Cho, J. *Nano Lett.* **2009**, *9*, 3844.
(193) Yoo, J.-K.; Kim, J.; Jung, Y. S.; Kang, K. *Adv. Mater.* **2012**, *24*, 5452.
(194) Saito, M.; Nakai, K.; Yamada, T.; Takenaka, T.; Hirota, M.; Kamei, A.; Tasaka, A.; Inaba, M. *J. Power Sources* **2011**, *196*, 6637.
(195) Yamada, T.; Saito, M.; Yodoya, C.; Kamei, A.; Hirota, M.; Takenaka, T.; Tasaka, A.; Inaba, M. *ECS Trans.* **2012**, *41*, 27.
(196) Green, M.; Fielder, E.; Scrosati, B.; Wachtler, M.; Moreno, J. S. *Electrochem. Solid-State Lett.* **2003**, *6*, A75.
(197) Lee, S. W.; McDowell, M. T.; Berla, L. A.; Nix, W. D.; Cui, Y. *Proc. Natl. Acad. Sci. U.S.A.* **2012**, *109*, 4080.
(198) Ma, H.; Cheng, F.; Chen, J.-Y.; Zhao, J.-Z.; Li, C.-S.; Tao, Z.-L.; Liang, J. *Adv. Mater.* **2007**, *19*, 4067.
(199) Yao, Y.; McDowell, M. T.; Ryu, I.; Wu, H.; Liu, N.; Hu, L.; Nix, W. D.; Cui, Y. *Nano Lett.* **2011**, *11*, 2949.
(200) Zhou, W.; Jiang, T.; Zhou, H.; Wang, Y.; Fang, J.; Whittingham, M. S. *MRS Commun.* **2013**, *3*, 119.
(201) Hu, L.; Wu, H.; Hong, S. S.; Cui, L.; McDonough, J. R.; Bohy, S.; Cui, Y. *Chem. Commun. (Cambridge, U. K.)* **2011**, *47*, 367.
(202) Yao, H.; Zheng, G.; Li, W.; McDowell, M. T.; Seh, Z.; Liu, N.; Lu, Z.; Cui, Y. *Nano Lett.* **2013**, *13*, 3385.
(203) Wilson, A. M.; Way, B. M.; Dahn, J. R.; van Buuren, T. *J. Appl. Phys.* **1995**, *77*, 2363.
(204) Wang, C. S. *J. Electrochem. Soc.* **1998**, *145*, 2751.
(205) Liu, N.; Wu, H.; McDowell, M. T.; Yao, Y.; Wang, C.; Cui, Y. *Nano Lett.* **2012**, *12*, 3315.
(206) Wu, H.; Zheng, G.; Liu, N.; Carney, T. J.; Yang, Y.; Cui, Y. *Nano Lett.* **2012**, *12*, 904.
(207) Wu, H.; Chan, G.; Choi, J. W.; Ryu, I.; Yao, Y.; McDowell, M. T.; Lee, S. W.; Jackson, A.; Yang, Y.; Hu, L.; Cui, Y. *Nat. Nanotechnol.* **2012**, *7*, 310.
(208) Gu, M.; Li, Y.; Li, X.; Hu, S.; Zhang, X.; Xu, W.; Thevuthasan, S.; Baer, D. R.; Zhang, J.-G.; Liu, J.; Wang, C. *ACS Nano* **2012**, *6*, 8439.
(209) Huggins, R. A.; Nix, W. D. *Ionics* **2000**, *6*, 57.
(210) Wang, C.-M.; Li, X.; Wang, Z.; Xu, W.; Liu, J.; Gao, F.; Kovarik, L.; Zhang, J.-G.; Howe, J.; Burton, D. J.; Liu, Z.; Xiao, X.; Thevuthasan, S.; Baer, D. R. *Nano Lett.* **2012**, *12*, 1624.
(211) Wang, F.; Wu, L.; Key, B.; Yang, X.-Q.; Grey, C. P.; Zhu, Y.; Graetz, J. *Adv. Energy Mater.* **2013**, *3*, 1324.
(212) Erk, C.; Brezesinski, T.; Sommer, H.; Schneider, R.; Janek, J. *ACS Appl. Mater. Interfaces* **2013**, *5*, 7299.
(213) Yin, J.; Wada, M.; Yamamoto, K.; Kitano, Y.; Tanase, S.; Sakai, T. *J. Electrochem. Soc.* **2006**, *153*, A472.
(214) Sethuraman, V. A.; Chon, M. J.; Shimshak, M.; Srinivasan, V.; Guduru, P. R. *J. Power Sources* **2010**, *195*, 5062.
(215) Sethuraman, V. A.; Chon, M. J.; Shimshak, M.; Van Winkle, N.; Guduru, P. R. *Electrochem. Commun.* **2010**, *12*, 1614.
(216) Goldman, J. L.; Long, B. R.; Gewirth, A. A.; Nuzzo, R. G. *Adv. Funct. Mater.* **2011**, *21*, 2412.
(217) Kim, G.; Jeong, S.; Shin, J.-H.; Cho, J.; Lee, H. *ACS Nano* **2014**, *8*, 1907.
(218) Bourderau, S.; Brousse, T.; Schleich, D. *J. Power Sources* **1999**, *81−82*, 233.
(219) Takamura, T.; Ohara, S.; Uehara, M.; Suzuki, J.; Sekine, K. *J. Power Sources* **2004**, *129*, 96.
(220) Baranchugov, V.; Markevich, E.; Pollak, E.; Salitra, G.; Aurbach, D. *Electrochem. Commun.* **2007**, *9*, 796.
(221) Choi, N.-S.; Yew, K. H.; Lee, K. Y.; Sung, M.; Kim, H.; Kim, S.-S. *J. Power Sources* **2006**, *161*, 1254.
(222) Markevich, E.; Fridman, K.; Sharabi, R.; Elazari, R.; Salitra, G.; Gottlieb, H. E.; Gershinsky, G.; Garsuch, A.; Semrau, G.; Schmidt, M. A.; Aurbach, D. *J. Electrochem. Soc.* **2013**, *160*, A1824.

(223) Sethuraman, V. A.; Kowolik, K.; Srinivasan, V. *J. Power Sources* **2011**, *196*, 393.
(224) Nadimpalli, S. P. V.; Sethuraman, V. A.; Dalavi, S.; Lucht, B.; Chon, M. J.; Shenoy, V. B.; Guduru, P. R. *J. Power Sources* **2012**, *215*, 145.
(225) Chen, L.; Wang, K.; Xie, X.; Xie, J. *Electrochem. Solid-State Lett.* **2006**, *9*, A512.
(226) Al-Maghrabi, M. A.; van der Bosch, N.; Sanderson, R. J.; Stevens, D. A.; Dunlap, R. A.; Dahn, J. R. *Electrochem. Solid-State Lett.* **2011**, *14*, A42.
(227) Harris, J. T.; Hueso, J. L.; Korgel, B. A. *Chem. Mater.* **2010**, *22*, 6378.
(228) Roberts, G. A.; Cairns, E. J.; Reimer, J. A. *J. Power Sources* **2002**, *110*, 424.
(229) Moriga, T.; Watanabe, K.; Tsuji, D.; Massaki, S.; Nakabayashi, I. *J. Solid State Chem.* **2000**, *153*, 386.
(230) Imai, Y.; Watanabe, A. *J. Alloys Compd.* **2011**, *509*, 7877.
(231) Liu, H.; Hu, C.; Wu, S. *Mater. Renewable Energy* **2011**, 683.
(232) Song, S.-W.; Striebel, K. A.; Reade, R. P.; Roberts, G. A.; Cairns, E. J. *J. Electrochem. Soc.* **2003**, *150*, A121.
(233) Xiao, C.; Du, N.; Zhang, H.; Yang, D. *J. Alloys Compd.* **2014**, *587*, 807.
(234) Hwang, S.-M.; Lee, H.-Y.; Jang, S.-W.; Lee, S.-M.; Lee, S.-J.; Baik, H.-K.; Lee, J.-Y. *Electrochem. Solid-State Lett.* **2001**, *4*, A97.
(235) Yang, X.; Wen, Z.; Huang, S.; Zhu, X.; Zhang, X. *Solid State Ionics* **2006**, *177*, 2807.
(236) Lee, S.-J.; Lee, H.-Y.; Park, Y.; Baik, H.-K.; Lee, S.-M. *J. Power Sources* **2003**, *119−121*, 117.
(237) Alcántara, R.; Tillard-Charbonnel, M.; Spina, L.; Belin, C.; Tirado, J. L. *Electrochim. Acta* **2002**, *47*, 1115.
(238) Hatchard, T. D.; Obrovac, M. N.; Dahn, J. R. *J. Electrochem. Soc.* **2005**, *152*, A2335.
(239) Gröbner, J.; Kevorkov, D.; Schmid-Fetzer, R. *J. Solid State Chem.* **2001**, *156*, 506.
(240) Kevorkov, D.; Gröbner, J.; Schmid-Fetzer, R. *J. Solid State Chem.* **2001**, *156*, 500.
(241) Spina, L.; Jia, Y. Z.; Ducourant, B.; Tillard, M.; Belin, C. *Z. Kristallogr.* **2003**, *218*, 740.
(242) Tillard, M.; Belin, C.; Spina, L.; Jia, Y. Z. *Solid State Sci.* **2005**, *7*, 1125.
(243) Pisch, A.; Jakse, N.; Pasturel, A.; Harvey, J. P.; Chartrand, P. *Appl. Phys. Lett.* **2007**, *90*, 251902.
(244) Liu, L.; Obrovac, M. N. *ECS Electrochem. Lett.* **2012**, *1*, A10.
(245) Terranova, M. L.; Orlanducci, S.; Tamburri, E.; Guglielmotti, V.; Rossi, M. *J. Power Sources* **2014**, *246*, 167.
(246) Xing, W.; Wilson, A.; Eguchi, K.; Zank, G.; Dahn, J. *J. Electrochem. Soc.* **1997**, *144*, 2410.
(247) Yang, J.; Wang, B. F.; Wang, K.; Liu, Y.; Xie, J. Y.; Wen, Z. S. *Electrochem. Solid-State Lett.* **2003**, *6*, A154.
(248) Kim, I.; Blomgren, G. E.; Kumta, P. N. *J. Power Sources* **2004**, *130*, 275.
(249) Hanai, K.; Liu, Y.; Imanishi, N.; Hirano, A.; Matsumura, M.; Ichikawa, T.; Takeda, Y. *J. Power Sources* **2005**, *146*, 156.
(250) Datta, M. K.; Kumta, P. N. *J. Power Sources* **2006**, *158*, 557.
(251) Timmons, A.; Todd, A. D. W.; Mead, S. D.; Carey, G. H.; Sanderson, R. J.; Mar, R. E.; Dahn, J. R. *J. Electrochem. Soc.* **2007**, *154*, A865.
(252) Wang, G. X.; Ahn, J. H.; Yao, J.; Bewlay, S.; Liu, H. K. *Electrochem. Commun.* **2004**, *6*, 689.
(253) Larcher, D.; Mudalige, C.; George, A. E.; Porter, V.; Gharghouri, M.; Dahn, J. R. *Solid State Ionics* **1999**, *122*, 71.
(254) Liu, Y.; Wen, Z. Y.; Wang, X. Y.; Hirano, A.; Imanishi, N.; Takeda, Y. *J. Power Sources* **2009**, *189*, 733.
(255) Wang, W.; Kumta, P. N. *J. Power Sources* **2007**, *172*, 650.
(256) Datta, M. K.; Kumta, P. N. *J. Power Sources* **2006**, *158*, 557.
(257) Lipson, A. L.; Chattopadhyay, S.; Karmel, H. J.; Fister, T. T.; Emery, J. D.; Dravid, V. P.; Thackeray, M. M.; Fenter, P. A.; Bedzyk, M. J.; Hersam, M. C. *J. Phys. Chem. C* **2012**, *116*, 20949.
(258) Kim, H.; Cho, J. *Nano Lett.* **2008**, *8*, 3688.
(259) Li, X.; Meduri, P.; Chen, X.; Qi, W.; Engelhard, M. H.; Xu, W.; Ding, F.; Xiao, J.; Wang, W.; Wang, C.; Zhang, J.-G.; Liu, J. *J. Mater. Chem.* **2012**, *22*, 11014.
(260) Wang, B.; Li, X.; Zhang, X.; Luo, B.; Zhang, Y.; Zhi, L. *Adv. Mater.* **2013**, *25*, 3560.
(261) Tao, H.-C.; Fan, L.-Z.; Qu, X. *Electrochim. Acta* **2012**, *71*, 194.
(262) Wang, M.-S.; Fan, L.-Z.; Huang, M.; Li, J.; Qu, X. *J. Power Sources* **2012**, *219*, 29.
(263) Hong, I.; Scrosati, B.; Croce, F. *Solid State Ionics* **2013**, *232*, 24.
(264) Yao, H.; Zheng, G.; Li, W.; McDowell, M. T.; Seh, Z.; Liu, N.; Lu, Z.; Cui, Y. *Nano Lett.* **2013**, *13*, 3385.
(265) Zhao, X.; Rui, X.; Zhou, W.; Tan, L.; Yan, Q.; Lu, Z.; Hng, H. H. *J. Power Sources* **2014**, *250*, 160.
(266) Richard, M. N.; Dahn, J. R. *J. Electrochem. Soc.* **1999**, *146*, 2068.
(267) Chen, Z.; Christensen, L.; Dahn, J. R. *Electrochem. Commun.* **2003**, *5*, 919.
(268) Hatchard, T. D.; Dahn, J. R. *J. Electrochem. Soc.* **2004**, *151*, A1628.
(269) Ahn, H.-J.; Kim, Y.-S.; Park, K.-W.; Seong, T.-Y. *Chem. Commun. (Cambridge, U. K.)* **2005**, 43.
(270) Yin, J.; Wada, M.; Yoshida, S.; Ishihara, K.; Tanase, S.; Sakai, T. *J. Electrochem. Soc.* **2003**, *150*, A1129.
(271) Yang, J.; Winter, M.; Besenhard, J. O. *Solid State Ionics* **1996**, *90*, 281.
(272) Yang, J.; Takeda, Y.; Imanishi, N.; Yamamoto, O. *J. Electrochem. Soc.* **1999**, *146*, 4009.
(273) Yang, J.; Takeda, Y.; Imanishi, N.; Xie, J. Y.; Yamamoto, O. *J. Electrochem. Soc.* **2000**, *133*, 189.
(274) Trifonova, A.; Wachtler, M.; Winter, M.; Besenhard, J. O. *Ionics* **2002**, *8*, 321.
(275) Wachtler, M.; Winter, M.; Besenhard, J. O. *J. Power Sources* **2002**, *105*, 151.
(276) Zhao, H.; Yin, C.; Guo, H.; He, J.; Qiu, W.; Li, Y. *J. Power Sources* **2007**, *174*, 916.
(277) Kim, I.; Blomgren, G. E.; Kumta, P. N. *Electrochem. Solid-State Lett.* **2004**, *7*, A44.
(278) Meschini, I.; Nobili, F.; Mancini, M.; Marassi, R.; Tossici, R.; Savoini, A.; Focarete, M. L.; Croce, F. *J. Power Sources* **2013**, *226*, 241.
(279) Tan, Z.; Sun, Z.; Wang, H.; Guo, Q.; Su, D. *J. Mater. Chem. A* **2013**, *1*, 9462.
(280) Zhu, Z.; Wang, S.; Du, J.; Jin, Q.; Zhang, T.; Cheng, F.; Chen, J. *Nano Lett.* **2014**, *14*, 153.
(281) Larcher, D.; Prakash, A. S.; Saint, J.; Morcrette, M.; Tarascon, J. *Chem. Mater.* **2004**, *16*, 5502.
(282) Aldon, L.; Ionica, C. M.; Lippens, P. E.; Larcher, D.; Tarascon, J.-M.; Olivier-Fourcade, J.; Jumas, J.-C. *Hyperfine Interact.* **2006**, *167*, 729.
(283) Wang, L.; Kitamura, S.; Sonoda, T.; Obata, K.; Tanase, S.; Sakai, T. *J. Electrochem. Soc.* **2003**, *150*, A1346.
(284) Ru, Q.; Peng, W.; Zhang, Z.; Hu, S.; Li, Y. *Rare Met.* **2011**, *30*, 160.
(285) Du, Z.; Zhang, S.; Zhao, J.; Fang, Y. *J. Appl. Electrochem.* **2012**, *42*, 477.
(286) Hu, R. Z.; Zhang, L.; Liu, X.; Zeng, M. Q.; Zhu, M. *Electrochem. Commun.* **2008**, *10*, 1109.
(287) Hu, R.; Zeng, M.; Li, C. Y. V.; Zhu, M. *J. Power Sources* **2009**, *188*, 268.
(288) Guo, J.; Yang, Z.; Archer, L. A. *J. Mater. Chem. A* **2013**, *1*, 8710.
(289) Ni, W.; Wang, Y.; Xu, R. *Part. Part. Syst. Charact.* **2013**, *30*, 873.
(290) Luo, B.; Wang, B.; Liang, M.; Ning, J.; Li, X.; Zhi, L. *Adv. Mater.* **2012**, *24*, 1405.
(291) Li, X.; Dhanabalan, A.; Gu, L.; Wang, C. *Adv. Energy Mater.* **2012**, *2*, 238.
(292) Yu, Y.; Gu, L.; Wang, C.; Dhanabalan, A.; van Aken, P. a; Maier, J. *Angew. Chem., Int. Ed.* **2009**, *48*, 6485.
(293) Ji, L.; Tan, Z.; Kuykendall, T.; An, E. J.; Fu, Y.; Battaglia, V.; Zhang, Y. *Energy Environ. Sci.* **2011**, *4*, 3611.
(294) Luo, B.; Wang, B.; Li, X.; Jia, Y.; Liang, M.; Zhi, L. *Adv. Mater.* **2012**, *24*, 3538.

(295) Courtney, I. A.; McKinnon, W. R.; Dahn, J. R. *J. Electrochem. Soc.* **1999**, *146*, 59.
(296) Weydanz, W. .; Wohlfahrt-Mehrens, M.; Huggins, R. *J. Power Sources* **1999**, *81−82*, 237.
(297) Netz, A.; Huggins, R. *Solid State Ionics* **2004**, *175*, 215.
(298) Netz, A.; Huggins, R. A.; Weppner, W. *J. Power Sources* **2003**, *119−121*, 95.
(299) Fleischauer, M. D.; Topple, J. M.; Dahn, J. R. *Electrochem. Solid-State Lett.* **2005**, *8*, A137.
(300) Lee, H. *J. Power Sources* **2002**, *112*, 649.
(301) Dong, H.; Ai, X. P.; Yang, H. X. *Electrochem. Commun.* **2003**, *5*, 952.
(302) Li, T.; Cao, Y. L.; Ai, X. P.; Yang, H. X. *J. Power Sources* **2008**, *184*, 473.
(303) Fleischauer, M. D.; Mar, R.; Dahn, J. R. *J. Electrochem. Soc.* **2007**, *154*, A151.
(304) Park, M.-S.; Lee, Y.-J.; Rajendran, S.; Song, M.-S.; Kim, H.-S.; Lee, J.-Y. *Electrochim. Acta* **2005**, *50*, 5561.
(305) Kim, T.; Park, S.; Oh, S. M. *Electrochem. Commun.* **2006**, *8*, 1461.
(306) Du, N.; Fan, X.; Yu, J.; Zhang, H.; Yang, D. *Electrochem. Commun.* **2011**, *13*, 1443.
(307) Kim, J.-H.; Kim, H.; Sohn, H.-J. *Electrochem. Commun.* **2005**, *7*, 557.
(308) NuLi, Y.; Wang, B.; Yang, J.; Yuan, X.; Ma, Z. *J. Power Sources* **2006**, *153*, 371.
(309) Dahn, J. R.; Mar, R. E.; Fleischauer, M. D.; Obrovac, M. N. *J. Electrochem. Soc.* **2006**, *153*, A1211.
(310) Wang, G.; Sun, L.; Bradhurst, D.; Zhong, S.; Dou, S.; Liu, H. *J. Alloys Compd.* **2000**, *306*, 249.
(311) Zhou, Y.-N.; Li, W.-J.; Chen, H.-J.; Liu, C.; Zhang, L.; Fu, Z. *Electrochem. Commun.* **2011**, *13*, 546.
(312) Liu, W.-R.; Wu, N.-L.; Shieh, D.-T.; Wu, H.-C.; Yang, M.-H.; Korepp, C.; Besenhard, J. O.; Winter, M. *J. Electrochem. Soc.* **2007**, *154*, A97.
(313) Zhang, H.-L.; Li, F.; Liu, C.; Cheng, H.-M. *Nanotechnology* **2008**, *19*, 165606.
(314) Zhou, S.; Simpson, Z. I.; Yang, X.; Wang, D. *ACS Nano* **2012**, *6*, 8114.
(315) Aselage, T. L. *J. Mater. Res.* **1998**, *13*, 1786.
(316) Rousselot, S.; Gauthier, M.; Mazouzi, D.; Lestriez, B.; Guyomard, D.; Roué, L. *J. Power Sources* **2012**, *202*, 262.
(317) Kim, I.; Kumta, P. N.; Blomgren, G. E. *Electrochem. Solid-State Lett.* **2000**, *3*, 493.
(318) Kim, I.; Blomgren, G. E.; Kumta, P. N. *Electrochem. Solid-State Lett.* **2003**, *6*, A157.
(319) Lee, H.-Y.; Lee, S.-M. *Electrochem. Commun.* **2004**, *6*, 465.
(320) Todd, A. D. W.; Mar, R. E.; Dahn, J. R. *J. Electrochem. Soc.* **2006**, *153*, A1998.
(321) Wang, X.-L.; Feygenson, M.; Chen, H.; Lin, C.-H.; Ku, W.; Bai, J.; Aronson, M. C.; Tyson, T. a.; Han, W.-Q. *J. Am. Chem. Soc.* **2011**, *133*, 11213.
(322) Zhang, C. Q.; Tu, J. P.; Huang, X. H.; Yuan, Y. F.; Wang, S. F.; Mao, F. *J. Alloys Compd.* **2008**, *457*, 81.
(323) Mao, O.; Dahn, J. *J. Electrochem. Soc.* **1999**, *146*, 414.
(324) Larcher, D.; Beaulieu, L. Y.; Macneil, D. D.; Dahn, J. R. *J. Electrochem. Soc.* **2000**, *147*, 1658.
(325) Kitada, A.; Fukuda, N.; Ichii, T.; Sugimura, H.; Murase, K. *Electrochim. Acta* **2013**, *98*, 239.
(326) Tamura, N.; Ohshita, R.; Fujimoto, M.; Kamino, M.; Fujitani, S. *J. Electrochem. Soc.* **2003**, *150*, A679.
(327) Yoshinaga, H.; Asai, J.; Wada, M.; Yamamoto, K. *Electrochemistry* **2005**, *73*, 897.
(328) Yoshinaga, H.; Dan, S.; Kawabata, A.; Sakai, T. *J. Jpn. Inst. Met.* **2002**, *66*, 861.
(329) Beaulieu, L.; Larcher, D.; Dunlap, R.; Dahn, J. *J. Alloys Compd.* **2000**, *297*, 122.
(330) Tamura, N.; Fujimoto, M.; Kamino, M.; Fujitani, S. *Electrochim. Acta* **2004**, *49*, 1949.
(331) Mukaibo, H.; Sumi, T.; Yokoshima, T.; Momma, T.; Osaka, T. *Electrochem. Solid-State Lett.* **2003**, *6*, A218.
(332) Lee, H.; Jang, S.; Lee, S.; Lee, S.; Baik, H. *J. Power Sources* **2002**, *112*, 8.
(333) Kim, Y.-L.; Heon-Young, L.; Serk-Won, J.; Seung-Joo, L.; Hong-Koo, B.; Young-Soo, Y.; Young-Shin, P.; Sung-Man, L. *Solid State Ionics* **2003**, *160*, 235.
(334) Dong, Q.; Wu, C.; Jin, M.; Huang, Z.; Zheng, M.; You, J.; ZG, L. *Solid State Ionics* **2004**, *167*, 49.
(335) Beattie, S. D.; Dahn, J. R. *J. Electrochem. Soc.* **2003**, *150*, A894.
(336) Kepler, K. D.; Vaughey, J. T.; Thackeray, M. M. *J. Power Sources* **1999**, *81−82*, 383.
(337) Zhang, J.; Xia, Y. *J. Electrochem. Soc.* **2006**, *153*, A1466.
(338) Kepler, K. D.; Vaughey, J. T.; Thackeray, M. M. *Electrochem. Solid-State Lett.* **1999**, *2*, 307.
(339) Kwon, J. Y.; Ryu, J. H.; Jung, Y. S.; Oh, S. M. *J. Alloys Compd.* **2011**, *509*, 7595.
(340) Hassoun, J.; Panero, S.; Simon, P.; Taberna, P. L.; Scrosati, B. *Adv. Mater.* **2007**, *19*, 1632.
(341) Sakaguchi, H.; Honda, H.; Akasaka, Y.; Esaka, T. *J. Power Sources* **2003**, *119−121*, 50.
(342) Reddy, M. V.; Subba Rao, G. V.; Chowdari, B. V. R. *Chem. Rev.* **2013**, *113*, 5364.
(343) Kim, C.; Noh, M.; Choi, M.; Cho, J.; Park, B. *Chem. Mater.* **2005**, *17*, 3297.
(344) Mansour, A. N.; Mukerjee, S.; Yang, X. Q.; McBreen, J. *J. Electrochem. Soc.* **2000**, *147*, 869.
(345) Wachtler, M.; Wagner, M. R.; Schmied, M.; Winter, M.; Besenhard, J. O. *J. Electroanal. Chem.* **2001**, *510*, 12.
(346) Li, J.; Christensen, L.; Obrovac, M. N.; Hewitt, K. C.; Dahn, J. R. *J. Electrochem. Soc.* **2008**, *155*, A234.
(347) Gong, L.; Nguyen, M. H. T.; Oh, E.-S. *Electrochem. Commun.* **2013**, *29*, 45.
(348) Choi, N.-S.; Yew, K. H.; Choi, W.-U.; Kim, S.-S. *J. Power Sources* **2008**, *177*, 590.
(349) Kim, J. S.; Choi, W.; Cho, K. Y.; Byun, D.; Lim, J.; Lee, J. K. *J. Power Sources* **2013**, *244*, 521.
(350) Liu, W.-R.; Yang, M.-H.; Wu, H.-C.; Chiao, S. M.; Wu, N.-L. *Electrochem. Solid-State Lett.* **2005**, *8*, A100.
(351) Lestriez, B.; Bahri, S.; Sandu, I.; Roue, L.; Guyomard, D. *Electrochem. Commun.* **2007**, *9*, 2801.
(352) Hochgatterer, N. S.; Schweiger, M. R.; Koller, S.; Raimann, P. R.; Wöhrle, T.; Wurm, C.; Winter, M. *Electrochem. Solid-State Lett.* **2008**, *11*, A76.
(353) Bridel, J.-S.; Azaïs, T.; Morcrette, M.; Tarascon, J.-M.; Larcher, D. *J. Electrochem. Soc.* **2011**, *158*, A750.
(354) Cerbelaud, M.; Lestriez, B.; Guyomard, D.; Videcoq, A.; Ferrando, R. *Langmuir* **2012**, *28*, 10713.
(355) Li, J.; Le, D.-B.; Ferguson, P. P.; Dahn, J. R. *Electrochim. Acta* **2010**, *55*, 2991.
(356) Magasinski, A.; Zdyrko, B.; Kovalenko, I.; Hertzberg, B.; Burtovyy, R.; Huebner, C. F.; Fuller, T. F.; Luzinov, I.; Yushin, G. *ACS Appl. Mater. Interfaces* **2010**, *2*, 3004.
(357) Komaba, S.; Shimomura, K.; Yabuuchi, N.; Ozeki, T.; Yui, H.; Konno, K. *J. Phys. Chem. C* **2011**, *115*, 13487.
(358) Kovalenko, I.; Zdyrko, B.; Magasinski, A.; Hertzberg, B.; Milicev, Z.; Burtovyy, R.; Luzinov, I.; Yushin, G. *Science* **2011**, *334*, 75.
(359) Lee, Y. M.; Lee, J. Y.; Shim, H.-T.; Lee, J. K.; Park, J.-K. *J. Electrochem. Soc.* **2007**, *154*, A515.
(360) Nie, M.; Abraham, D. P.; Chen, Y.; Bose, A.; Lucht, B. L. *J. Phys. Chem. C* **2013**, *117*, 13403.
(361) Philippe, B.; Dedryvère, R.; Gorgoi, M.; Rensmo, H.; Gonbeau, D.; Edström, K. *J. Am. Chem. Soc.* **2013**, *135*, 9829.
(362) Wang, C.; Wu, H.; Chen, Z.; McDowell, M. T.; Cui, Y.; Bao, Z. *Nat. Chem.* **2013**, *5*, 1042.
(363) Koo, B.; Kim, H.; Cho, Y.; Lee, K. T.; Choi, N.-S.; Cho, J. *Angew. Chem., Int. Ed.* **2012**, *51*, 8762.
(364) Jow, T. R.; Shacklette, L. W.; Maxfield, M.; Vernick, D. *J. Electrochem. Soc.* **1987**, *134*, 1730.

(365) Wu, H.; Yu, G.; Pan, L.; Liu, N.; McDowell, M. T.; Bao, Z.; Cui, Y. *Nat. Commun.* **2013**, *4*, 1943.
(366) Yamada, M.; Ueda, A.; Matsumoto, K.; Ohzuku, T. *J. Electrochem. Soc.* **2011**, *158*, A417.
(367) Liu, Y.; Wen, Z. Y.; Wang, X. Y.; Yang, X. L.; Hirano, A.; Imanishi, N.; Takeda, Y. *J. Power Sources* **2009**, *189*, 480.
(368) Kim, J. W.; Ryu, J. H.; Lee, K. T.; Oh, S. M. *J. Power Sources* **2005**, *147*, 227.
(369) Yu, Y.; Gu, L.; Zhu, C.; Tsukimoto, S.; van Aken, P. a.; Maier, J. *Adv. Mater.* **2010**, *22*, 2247.
(370) Yoo, S.; Lee, J.-I.; Ko, S.; Park, S. *Nano Energy* **2013**, *2*, 1271.
(371) Shimoi, N.; Tanaka, Y. *Electrochim. Acta* **2012**, *80*, 227.
(372) Jeong, G.; Kim, J.-H.; Kim, Y.-U.; Kim, Y.-J. *J. Mater. Chem.* **2012**, *22*, 7999.
(373) Kataoka, R.; Mukai, T.; Yoshizawa, A.; Sakai, T. *J. Electrochem. Soc.* **2013**, *160*, A1684.
(374) Park, O.; Lee, J.-I.; Chun, M.-J.; Yeon, J.-T.; Yoo, S.; Choi, S.; Choi, N.-S.; Park, S. *RSC Adv.* **2013**, *3*, 2538.
(375) Wagner, M. R.; Raimann, P. R.; Trifonova, A.; Moeller, K.-C.; Besenhard, J. O.; Winter, M. *Electrochem. Solid-State Lett.* **2004**, *7*, A201.
(376) Wang, C.; John Appleby, A.; Little, F. E. *J. Power Sources* **2001**, *93*, 174.
(377) Choi, N.-S.; Yew, K. H.; Kim, H.; Kim, S.-S.; Choi, W.-U. *J. Power Sources* **2007**, *172*, 404.
(378) Nakai, H.; Kubota, T.; Kita, A.; Kawashima, A. *J. Electrochem. Soc.* **2011**, *158*, A798.
(379) Elazari, R.; Salitra, G.; Gershinsky, G.; Garsuch, A.; Panchenko, A.; Aurbach, D. *J. Electrochem. Soc.* **2012**, *159*, A1440.
(380) Mazouzi, D.; Delpuech, N.; Oumellal, Y.; Gauthier, M.; Cerbelaud, M.; Gaubicher, J.; Dupré, N.; Moreau, P.; Guyomard, D.; Roué, L.; Lestriez, B. *J. Power Sources* **2012**, *220*, 180.
(381) Han, G.-B.; Ryou, M.-H.; Cho, K. Y.; Lee, Y. M.; Park, J.-K. *J. Power Sources* **2010**, *195*, 3709.
(382) Schroder, K. W.; Celio, H.; Webb, L. J.; Stevenson, K. J. *J. Phys. Chem. C* **2012**, *116*, 19737.
(383) Song, S.-W.; Baek, S.-W. *Electrochem. Solid-State Lett.* **2009**, *12*, A23.
(384) Kajita, T.; Yuge, R.; Nakahara, K.; Iriyama, J.; Takahashi, H.; Kasahara, R.; Numata, T.; Serizawa, S.; Utsugi, K. *J. Electrochem. Soc.* **2013**, *160*, A1806.
(385) Dalavi, S.; Guduru, P.; Lucht, B. L. *J. Electrochem. Soc.* **2012**, *159*, A642.
(386) Delpuech, N.; Dupré, N.; Mazouzi, D.; Gaubicher, J.; Moreau, P.; Bridel, J. S.; Guyomard, D.; Lestriez, B. *Electrochem. Commun.* **2013**, *33*, 72.
(387) McArthur, M. A.; Trussler, S.; Dahn, J. R. *J. Electrochem. Soc.* **2012**, *159*, A198.
(388) Bridel, J.-S.; Grugeon, S.; Laruelle, S.; Hassoun, J.; Reale, P.; Scrosati, B.; Tarascon, J.-M. *J. Power Sources* **2010**, *195*, 2036.
(389) Han, G.-B.; Lee, J.-N.; Choi, J. W.; Park, J.-K. *Electrochim. Acta* **2011**, *56*, 8997.
(390) Ryu, Y.-G.; Lee, S.; Mah, S.; Lee, D. J.; Kwon, K.; Hwang, S.; Doo, S. *J. Electrochem. Soc.* **2008**, *155*, A583.
(391) Li, M.-Q.; Qu, M.-Z.; He, X.-Y.; Yu, Z.-L. *J. Electrochem. Soc.* **2009**, *156*, A294.
(392) Jouen, S.; Hannoyer, B.; Piana, O. *Surf. Interface Anal.* **2002**, *34*, 192.
(393) Cho, S.; Yu, J.; Kang, S. K.; Shih, D.-Y. *J. Electron. Mater.* **2005**, *34*, 635.
(394) Beattie, S. D.; Hatchard, T.; Bonakdarpour, A.; Hewitt, K. C.; Dahn, J. R. *J. Electrochem. Soc.* **2003**, *150*, A701.
(395) Baek, S.-W.; Hong, S.-J.; Kim, D.-W.; Song, S.-W. *J. Power Sources* **2009**, *189*, 660.
(396) Song, S.-W.; Baek, S.-W. *Electrochim. Acta* **2009**, *54*, 1312.
(397) Smith, A. J.; Burns, J. C.; Trussler, S.; Dahn, J. R. *J. Electrochem. Soc.* **2010**, *157*, A196.
(398) Yoshio, M.; Wang, H.; Fukuda, K.; Umeno, T.; Dimov, N.; Ogumi, Z. *J. Electrochem. Soc.* **2002**, *149*, A1598.
(399) Kim, T.; Park, S.; Oh, S. M. *J. Electrochem. Soc.* **2007**, *154*, A1112.
(400) Kim, J.; Sohn, H.; Kim, H.; Jeong, G.; Choi, W. *J. Power Sources* **2007**, *170*, 456.
(401) Liu, X.; Zheng, M.-C.; Xie, K. *J. Power Sources* **2011**, *196*, 10667.
(402) Tabuchi, T.; Yasuda, H.; Yamachi, M. *J. Power Sources* **2005**, *146*, 507.
(403) Miyachi, M.; Yamamoto, H.; Kawai, H. *J. Electrochem. Soc.* **2007**, *154*, A376.
(404) Martin, L.; Martinez, H.; Ulldemolins, M.; Pecquenard, B.; Le Cras, F. *Solid State Ionics* **2012**, *215*, 36.
(405) Etacheri, V.; Geiger, U.; Gofer, Y.; Roberts, G. a; Stefan, I. C.; Fasching, R.; Aurbach, D. *Langmuir* **2012**, *28*, 6175.
(406) Philippe, B.; Allouche, J.; Lindgren, F.; Gorgoi, M.; Rensmo, H.; Gonbeau, D.; Edstro, K. *Chem. Mater.* **2012**, *24*, 1107.
(407) Takezawa, H.; Iwamoto, K.; Ito, S.; Yoshizawa, H. *J. Power Sources* **2013**, *244*, 149.
(408) Song, T.; Kil, K. C.; Jeon, Y.; Lee, S.; Shin, W. C.; Chung, B.; Kwon, K.; Paik, U. *J. Power Sources* **2014**, *253*, 282.
(409) Mukherjee, R.; Krishnan, R.; Lu, T.-M.; Koratkar, N. *Nano Energy* **2012**, *1*, 518.
(410) Wang, C. S.; Wu, G. T.; Zhang, X. B.; Qi, Z. F.; Li, W. Z. *J. Electrochem. Soc.* **1998**, *145*, 2751.
(411) Holzapfel, M.; Buqa, H.; Hardwick, L.; Hahn, M.; Wursig, A.; Scheifele, W.; Novak, P.; Kotz, R.; Veit, C.; Petrat, F. *Electrochim. Acta* **2006**, *52*, 973.
(412) Hu, Y.-S.; Demir-Cakan, R.; Titirici, M.-M.; Müller, J.-O.; Schlögl, R.; Antonietti, M.; Maier, J. *Angew. Chem., Int. Ed.* **2008**, *47*, 1645.
(413) Zhao, X.; Hayner, C. M.; Kung, M. C.; Kung, H. H. *Adv. Energy Mater.* **2011**, *1*, 1079.
(414) Bang, B. M.; Kim, H.; Song, H.-K.; Cho, J.; Park, S. *Energy Environ. Sci.* **2011**, *4*, 5013.
(415) Yoon, Y. S.; Jee, S. H.; Lee, S. H.; Nam, S. C. *Surf. Coat. Technol.* **2011**, *206*, 553.
(416) Murugesan, S.; Harris, J. T.; Korgel, B. A.; Stevenson, K. J. *Chem. Mater.* **2012**, *24*, 1306.
(417) Liu, B.; Abouimrane, A.; Ren, Y.; Balasubramanian, M.; Wang, D.; Fang, Z. Z.; Amine, K. *Chem. Mater.* **2012**, *24*, 4653.
(418) Yuge, R.; Toda, A.; Fukatsu, K.; Tamura, N.; Manako, T.; Nakahara, K.; Nakano, K. *J. Electrochem. Soc.* **2013**, *160*, A1789.
(419) Piper, D. M.; Yersak, T. A.; Son, S.-B.; Kim, S. C.; Kang, C. S.; Oh, K. H.; Ban, C.; Dillon, A. C.; Lee, S.-H. *Adv. Energy Mater.* **2013**, *3*, 697.
(420) Ebner, M.; Marone, F.; Stampanoni, M.; Wood, V. *Science* **2013**, *342*, 716.
(421) Lin, C.-K.; Ren, Y.; Amine, K.; Qin, Y.; Chen, Z. *J. Power Sources* **2013**, *230*, 32.
(422) Hu, Y.-Y.; Liu, Z.; Nam, K.-W.; Borkiewicz, O. J.; Cheng, J.; Hua, X.; Dunstan, M. T.; Yu, X.; Wiaderek, K. M.; Du, L.-S.; Chapman, K. W.; Chupas, P. J.; Yang, X.-Q.; Grey, C. P. *Nat. Mater.* **2013**, *12*, 1130.
(423) Mazouzi, D.; Lestriez, B.; Roué, L.; Guyomard, D. *Electrochem. Solid-State Lett.* **2009**, *12*, A215.
(424) Lestriez, B.; Desaever, S.; Danet, J.; Moreau, P.; Plée, D.; Guyomard, D. *Electrochem. Solid-State Lett.* **2009**, *12*, A76.
(425) Mazouzi, D.; Lestriez, B.; Roué, L.; Guyomard, D. *Electrochem. Solid-State Lett.* **2009**, *12*, A215.
(426) Thompson, A. H. *Phys. Rev. Lett.* **1978**, *40*, 1511.
(427) Burns, J. C.; Krause, L. J.; Le, D.-B.; Jensen, L. D.; Smith, A. J.; Xiong, D.; Dahn, J. R. *J. Electrochem. Soc.* **2011**, *158*, A1417.
(428) Applestone, D.; Manthiram, A. *J. Power Sources* **2012**, *217*, 1.
(429) Krause, L. J.; Chevrier, V. L.; Le, D. B.; Liu, L.; Jensen, L. D.; Singh, J.; Eberman, K. W. *30th International Seminar on Primary and Secondary Lithium Batteries*, Fort Lauderdale, 2013.
(430) Krause, L. J.; Liu, L.; Jensen, L. D.; Chevrier, V. L.; Singh, J. *222nd Meeting of the Electrochemical Society*, 2012; Abstract #343.
(431) Chen, C. H.; Liu, J.; Amine, K. *J. Power Sources* **2001**, *96*, 321.
(432) Plashnitsa, L. S.; Kobayashi, E.; Okada, S.; Yamaki, J. *Electrochim. Acta* **2011**, *56*, 1344.
(433) Petibon, R.; Henry, E. C.; Burns, J. C.; Sinha, N. N.; Dahn, J. R. *J. Electrochem. Soc.* **2013**, *161*, A66.

(434) Petibon, R.; Sinha, N. N.; Burns, J. C.; Aiken, C. P.; Ye, H.; VanElzen, C. M.; Jain, G.; Trussler, S.; Dahn, J. R. *J. Power Sources* **2014**, *251*, 187.
(435) Marks, T.; Trussler, S.; Smith, A. J.; Xiong, D.; Dahn, J. R. *J. Electrochem. Soc.* **2011**, *158*, A51.
(436) Eberman, K.; Gomadam, P. M.; Jain, G.; Scott, E. *ECS Trans.* **2010**, *25*, 47.
(437) Yamada, M.; Uchitomi, K.; Ueda, A.; Matsumoto, K.; Ohzuku, T. *J. Power Sources* **2013**, *225*, 221.
(438) Cui, L.-F.; Yang, Y.; Hsu, C.; Cui, Y. *Nano Lett.* **2009**, *9*, 3370.
(439) Burns, J. C.; Kassam, A.; Sinha, N. N.; Downie, L. E.; Solnickova, L.; Way, B. M.; Dahn, J. R. *J. Electrochem. Soc.* **2013**, *160*, A1451.
(440) Dubarry, M.; Liaw, B. Y. *J. Power Sources* **2009**, *194*, 541.
(441) Dubarry, M.; Liaw, B. Y. *J. Power Sources* **2007**, *174*, 856.
(442) Dahn, H. M.; Smith, A. J.; Burns, J. C.; Stevens, D. A.; Dahn, J. R. *J. Electrochem. Soc.* **2012**, *159*, A1405.
(443) Ryu, J. H.; Kim, J. W.; Sung, Y.-E.; Oh, S. M. *Electrochem. Solid-State Lett.* **2004**, *7*, A306.
(444) Orazem, M. E.; Tribollet, B. *Electrochemical Impedance Spectroscopy*; John Wiley & Sons, Inc.: Hoboken, NJ, 2008; pp 1−523.
(445) Mohamedi, M.; Lee, S.-J.; Takahashi, D.; Nishizawa, M.; Itoh, T.; Uchida, I. *Electrochim. Acta* **2001**, *46*, 1161.
(446) Aurbach, D.; Nimberger, A.; Markovsky, B.; Levi, E.; Sominski, E.; Gedanken, A. *Chem. Mater.* **2002**, *14*, 4155.
(447) Zhang, Y.; Zhang, X. G.; Zhang, H. L.; Zhao, Z. G.; Li, F.; Liu, C.; Cheng, H. M. *Electrochim. Acta* **2006**, *51*, 4994.
(448) Ding, N.; Xu, J.; Yao, Y.; Wegner, G.; Lieberwirth, I.; Chen, C. *J. Power Sources* **2009**, *192*, 644.
(449) Wu, Q.; Lu, W.; Prakash, J. *J. Power Sources* **2000**, *88*, 237.
(450) Ohzuku, T.; Tomura, H.; Sawai, K. *J. Electrochem. Soc.* **1997**, *144*, 3496.
(451) Villevieille, C.; Boinet, M.; Monconduit, L. *Electrochem. Commun.* **2010**, *12*, 1336.
(452) Kalnaus, S.; Rhodes, K.; Daniel, C. *J. Power Sources* **2011**, *196*, 8116.
(453) Yang, J.; Winter, M.; Besenhard, J. O. *Solid State Ionics* **1996**, *90*, 281.
(454) Jeong, G.; Lee, S. M.; Choi, N. S.; Kim, Y.-U.; Lee, C. K. *Electrochim. Acta* **2011**, *56*, 5095.
(455) Miyuki, T.; Okuyama, Y.; Kojima, T.; Sakai, T. *Electrochemistry* **2012**, *80*, 405.
(456) Yu, H.-J.; Hong, K.-P.; Sung, M.-S.; Lee, S.; Yoon Sheem, K.; Kim, S.-S. *ECS Electrochem. Lett.* **2012**, *2*, A10.
(457) Krause, L. J.; Jensen, L. D.; Dahn, J. R. *J. Electrochem. Soc.* **2012**, *159*, A937.
(458) Wang, Y.; Dahn, J. R. *J. Electrochem. Soc.* **2006**, *153*, A2188.
(459) Wang, Y.; Dahn, J. R. *J. Electrochem. Soc.* **2006**, *153*, A2314.
(460) Zhou, F.; Zhao, X.; Fergusoń, P. P.; Thorne, J. S.; Dunlap, R. A.; Dahn, J. R. *J. Electrochem. Soc.* **2008**, *155*, A921.
(461) Profatilova, I. A.; Langer, T.; Badillo, J. P.; Schmitz, A.; Orthner, H.; Wiggers, H.; Passerini, S.; Winter, M. *J. Electrochem. Soc.* **2012**, *159*, A657.
(462) Profatilova, I. A.; Stock, C.; Schmitz, A.; Passerini, S.; Winter, M. *J. Power Sources* **2013**, *222*, 140.
(463) Park, Y.; Lee, S. *Bull. Korean Chem. Soc.* **2011**, *32*, 145.
(464) Matsumura, Y.; Wang, S.; Mondori, J. *J. Electrochem. Soc.* **1995**, *142*, 2914.
(465) Van Bommel, A.; Krause, L. J.; Dahn, J. R. *J. Electrochem. Soc.* **2011**, *158*, A731.
(466) Lu, Z.; Dahn, J. R. *J. Electrochem. Soc.* **2002**, *149*, A815.
(467) Jarvis, C. R.; Lain, M. J.; Yakovleva, M. V.; Gao, Y. *J. Power Sources* **2006**, *162*, 800.
(468) Seong, I. W.; Kim, K. T.; Yoon, W. Y. *J. Power Sources* **2009**, *189*, 511.
(469) Forney, M. W.; Ganter, M. J.; Staub, J. W.; Ridgley, R. D.; Landi, B. J. *Nano Lett.* **2013**, *13*, 4158.
(470) Yang, J.; Takeda, Y.; Imanishi, N.; Yamamoto, O. *J. Electrochem. Soc.* **2000**, *147*, 1671.
(471) Takeda, Y.; Yang, J.; Imanishi, N. *Solid State Ionics* **2002**, *152*−*153*, 35.
(472) Shanmukaraj, D.; Grugeon, S.; Laruelle, S.; Douglade, G.; Tarascon, J.-M.; Armand, M. *Electrochem. Commun.* **2010**, *12*, 1344.
(473) Gnanaraj, J. S.; Cohen, Y. S.; Levi, M. D.; Aurbach, D. *J. Electroanal. Chem.* **2001**, *516*, 89.
(474) Manev, V.; Naidenov, I.; Puresheva, B.; Pistoia, G. *J. Power Sources* **1995**, *57*, 133.
(475) Shim, J.; Striebel, K. A. *J. Power Sources* **2003**, *119*−*121*, 934.
(476) Dimov, N.; Noguchi, H.; Yoshio, M. *J. Power Sources* **2006**, *156*, 567.
(477) Park, Y.-S.; Kim, J.-Y.; Lee, S.-M. *Electrochem. Solid-State Lett.* **2011**, *14*, A36.
(478) Ng, S.-H.; Wang, J.; Wexler, D.; Konstantinov, K.; Guo, Z.-P.; Liu, H.-K. *Angew. Chem., Int. Ed.* **2006**, *45*, 6896.
(479) Jung, Y. S.; Lee, K. T.; Ryu, J. H.; Im, D.; Oh, S. M. *J. Electrochem. Soc.* **2005**, *152*, A1452.
(480) Lee, J.-H.; Kim, W.-J.; Kim, J.-Y.; Lim, S.-H.; Lee, S.-M. *J. Power Sources* **2008**, *176*, 353.
(481) Yang, J.; Wang, B. F.; Wang, K.; Liu, Y.; Xie, J. Y.; Wen, Z. S. *Electrochem. Solid-State Lett.* **2003**, *6*, A154.
(482) Park, M.-S.; Rajendran, S.; Kang, Y.-M.; Han, K.-S.; Han, Y.-S.; Lee, J.-Y. *J. Power Sources* **2006**, *158*, 650.
(483) Sony's New Nexelion Hybrid, Lithium Ion Batteries, http://www.sony.net/SonyInfo/News/Press/200502/05-006E/ (accessed Jan 1, 2014).
(484) Inoue, H. *International Meeting on Lithium Batteries*, Biarritz, 2006; Abstract #228.
(485) Inoue, H.; Mizutani, S.; Ishihara, H.; Hatake, S. *214th ECS Meeting*, 2007; Abstract #1160.
(486) Park, C.-M.; Sohn, H.-J. *Electrochim. Acta* **2009**, *54*, 6367.
(487) Todd, A. D. W.; Ferguson, P. P.; Fleischauer, M. D.; Dahn, J. R. *Int. J. Energy Res.* **2010**, *34*, 535.
(488) Development of a Notebook PC High-Capacity Secondary Li-ion Battery "Nexelion" (trans), http://www.sony.co.jp/SonyInfo/News/Press/201107/11-078 (accessed Jan 1, 2014).
(489) Ferguson, P. P.; Martine, M. L.; Dunlap, R. A.; Dahn, J. R. *Electrochim. Acta* **2009**, *54*, 4534.
(490) Ferguson, P. P.; Todd, A. D. W.; Dahn, J. R. *Electrochem. Commun.* **2010**, *12*, 1041.
(491) Ferguson, P. P.; Fleischauer, M. D.; LaForge, J. M.; Todd, A. D. W.; Li, P.; Dahn, J. R. *J. Alloys Compd.* **2012**, *541*, 168.
(492) Todd, A. D. W.; Ferguson, P. P.; Barker, J. G.; Fleischauer, M. D.; Dahn, J. R. *J. Electrochem. Soc.* **2009**, *156*, A1034.
(493) Thorne, J. S.; Ferguson, P. P.; Dunlap, R. A.; Dahn, J. R. *J. Alloys Compd.* **2009**, *472*, 390.
(494) Ferguson, P. P.; Rajora, M.; Dunlap, R. A.; Dahn, J. R. *J. Electrochem. Soc.* **2009**, *156*, A204.
(495) Todd, A.; Dunlap, R.; Dahn, J. *J. Alloys Compd.* **2007**, *443*, 114.
(496) Ferguson, P. P.; Liao, P.; Dunlap, R. A.; Dahn, J. R. *J. Electrochem. Soc.* **2009**, *156*, A13.
(497) Lewis, R. B.; Timmons, A.; Mar, R. E.; Dahn, J. R. *J. Electrochem. Soc.* **2007**, *154*, A213.
(498) Ferguson, P. P.; Martine, M. L.; George, A. E.; Dahn, J. R. *J. Power Sources* **2009**, *194*, 794.
(499) Ferguson, P. P.; Dahn, J. R. *Electrochem. Solid-State Lett.* **2008**, *11*, A187.
(500) Ferguson, P. P.; Dunlap, R. A.; Dahn, J. R. *J. Electrochem. Soc.* **2010**, *157*, A326.
(501) Todd, A. D. W.; Mar, R. E.; Dahn, J. R. *J. Electrochem. Soc.* **2007**, *154*, A597.
(502) Hassoun, J.; Ochal, P.; Panero, S.; Mulas, G.; Bonattominella, C.; Scrosati, B. *J. Power Sources* **2008**, *180*, 568.
(503) Hassoun, J.; Panero, S.; Mulas, G.; Scrosati, B. *J. Power Sources* **2007**, *171*, 928.
(504) Hassoun, J.; Mulas, G.; Panero, S.; Scrosati, B. *Electrochem. Commun.* **2007**, *9*, 2075.
(505) Fan, Q.; Chupas, P. J.; Whittingham, M. S. *Electrochem. Solid-State Lett.* **2007**, *10*, A274.

(506) Zhang, R.; Whittingham, M. S. *Electrochem. Solid-State Lett.* **2010**, *13*, A184.
(507) Wolfenstine, J.; Allen, J. L.; Read, J.; Foster, D. *Chemistry and Structure of Sony's Nexelion Li-ion Electrode Materials (ARL-TN-0257)*, 2006; pp 1−12.
(508) Foster, D.; Wolfenstine, J.; Read, J.; Allen, J. L. *Performance of Sony's Alloy Based Li-ion Battery (ARL-TN-0319)*, 2008; pp 1−14.
(509) Mao, O.; Dunlap, R.; Dahn, J. *J. Electrochem. Soc.* **1999**, *146*, 405.
(510) Mao, O.; Turner, R. L.; Courtney, I. A.; Fredericksen, B. D.; Buckett, M. I.; Krause, L. J.; Dahn, J. R. *Electrochem. Solid-State Lett.* **1999**, *2*, 3.
(511) Mao, Ou.; Dunlap, R. A.; Dahn, J. R. *J. Electrochem. Soc.* **1999**, *146*, 423.
(512) Christensen, L.; Le, D. B.; Singh, J.; Obrovac, M. N. *216th Meeting of the Electrochemical Society*, Vienna, 2009.
(513) Sepehri-Amin, H.; Ohkubo, T.; Kodzuka, M.; Yamamura, H.; Saito, T.; Iba, H.; Hono, K. *Scr. Mater.* **2013**, *69*, 92.
(514) Philipp, H. *J. Non-Cryst. Solids* **1972**, *8−10*, 627.
(515) Nagamori, M.; Boivin, J.-A.; Claveau, A. *J. Non-Cryst. Solids* **1995**, *189*, 270.
(516) Brady, G. *J. Phys. Chem.* **1959**, *63*, 1119.
(517) Nagao, Y.; Sakaguchi, H.; Honda, H.; Fukunaga, T.; Esaka, T. *J. Electrochem. Soc.* **2004**, *151*, A1572.
(518) Al-Maghrabi, M. A.; Suzuki, J.; Sanderson, R. J.; Chevrier, V. L.; Dunlap, R. A.; Dahn, J. R. *J. Electrochem. Soc.* **2013**, *160*, A1587.
(519) Hwa, Y.; Park, C.-M.; Sohn, H.-J. *J. Power Sources* **2013**, *222*, 129.
(520) Nagai, R.; Kita, F.; Yamada, M.; Katayama, H. *Hitachi Rev.* **2011**, *60*, 28.
(521) Schulmeister, K.; Mader, W. *J. Non-Cryst. Solids* **2003**, *320*, 143.
(522) Yamada, Y.; Iriyama, Y.; Abe, T.; Ogumi, Z. *J. Electrochem. Soc.* **2010**, *157*, A26.
(523) Veluchamy, A.; Doh, C.-H.; Kim, D.-H.; Lee, J.-H.; Lee, D.-J.; Ha, K.-H.; Shin, H.-M.; Jin, B.-S.; Kim, H.-S.; Moon, S.-I.; Park, C.-W. *J. Power Sources* **2009**, *188*, 574.
(524) Chang, W.-S.; Park, C.-M.; Kim, J.-H.; Kim, Y.-U.; Jeong, G.; Sohn, H.-J. *Energy Environ. Sci.* **2012**, *5*, 6895.
(525) Sun, Q.; Zhang, B.; Fu, Z.-W. *Appl. Surf. Sci.* **2008**, *254*, 3774.
(526) Park, M.-S.; Lee, Y.-J.; Han, Y.-S.; Lee, J.-Y. *Mater. Lett.* **2006**, *60*, 3079.
(527) Son, S.-B.; Kim, S. C.; Kang, C. S.; Yersak, T. A.; Kim, Y.-C.; Lee, C.-G.; Moon, S.-H.; Cho, J. S.; Moon, J.-T.; Oh, K. H.; Lee, S.-H. *Adv. Energy Mater.* **2012**, *2*, 1226.
(528) Jung, H.; Kim, Y.-U.; Sung, M.-S.; Hwa, Y.; Jeong, G.; Kim, G.-B.; Sohn, H.-J. *J. Mater. Chem.* **2011**, *21*, 11213.
(529) Lee, K. J.; Yu, S.-H.; Kim, J.-J.; Lee, D.-H.; Park, J.; Suh, S. S.; Cho, J. S.; Sung, Y.-E. *J. Power Sources* **2014**, *246*, 729.
(530) Suh, S.-S.; Yoon, W. Y.; Lee, C.-G.; Kwon, S.-U.; Kim, J.-H.; Matulevich, Y.; Kim, Y.-U.; Park, Y.; Jeong, C.-U.; Chan, Y.-Y.; Kang, S.-H. *J. Electrochem. Soc.* **2013**, *160*, A751.
(531) Panasonic Develops High-Capacity Lithium-Ion Battery Cells That Can Power Laptops and Electric Vehicles, http://panasonic.co.jp/corp/news/official.data/data.dir/en091225-3/en091225-3.html (accessed Jan 1, 2014).
(532) Zhao, H.; Yin, C.; Guo, H.; Qiu, W. *Electrochem. Solid-State Lett.* **2006**, *9*, A281.
(533) Goward, G.; Leroux, F.; Power, W. *Electrochem. Solid-State Lett.* **1999**, *2*, 367.